

AD _____

CONTRACT NUMBER DAMD17-94-C-4052

TITLE: Development of a Novel Intravenous Membrane Oxygenator

PRINCIPAL INVESTIGATOR: Brack G. Hattler, M.D., Ph.D.
Hout, Mariah, M.S., Lund, Laura, M.S., Federspiel, William, Ph.D.
Heinrich, Shelly, B.S., Hewitt, Todd, M.S.

CONTRACTING ORGANIZATION: University of Pittsburgh
Pittsburgh, Pennsylvania 15260

REPORT DATE: October 1997

TYPE OF REPORT: Final

PREPARED FOR: Commander
U.S. Army Medical Research and Materiel Command
Fort Detrick, Maryland 21702-5012

DISTRIBUTION STATEMENT: Approved for public release;
distribution unlimited

The views, opinions and/or findings contained in this report are those of the author(s) and should not be construed as an official Department of the Army position, policy or decision unless so designated by other documentation.

DTIC QUALITY INSPECTED 3

19980223 079

REPORT DOCUMENTATION PAGE			Form Approved OMB No. 0704-0188	
Public reporting burden for this collection of information is estimated to average 1 hour per response, including the time for reviewing instructions, searching existing data sources, gathering and maintaining the data needed, and completing and reviewing the collection of information. Send comments regarding this burden estimate or any other aspect of this collection of information, including suggestions for reducing this burden, to Washington Headquarters Services, Directorate for Information Operations and Reports, 1215 Jefferson Davis Highway, Suite 1204, Arlington, VA 22202-4302, and to the Office of Management and Budget, Paperwork Reduction Project (0704-0188), Washington, DC 20503.				
1. AGENCY USE ONLY (Leave blank)		2. REPORT DATE October 1997	3. REPORT TYPE AND DATES COVERED Final (1 Jun 94 - 28 Sep 97)	
4. TITLE AND SUBTITLE Development of a Novel Intravenous Membrane Oxygenator			5. FUNDING NUMBERS DAMD17-94-C-4052	
6. AUTHOR(S) Heinrich, Shelly, B.S., Hewitt, Todd, M.S. Hout, Mariah, M.S., Lund, Laura, M.S., Federspiel, William, Ph.D., Hattler, Brack, M.D., Ph.D.				
7. PERFORMING ORGANIZATION NAME(S) AND ADDRESS(ES) University of Pittsburgh Pittsburgh, Pennsylvania 15260			8. PERFORMING ORGANIZATION REPORT NUMBER	
9. SPONSORING / MONITORING AGENCY NAME(S) AND ADDRESS(ES) U.S. Army Medical Research and Materiel Command Fort Detrick, Maryland 21702-5012			10. SPONSORING / MONITORING AGENCY REPORT NUMBER	
11. SUPPLEMENTARY NOTES				
12a. DISTRIBUTION / AVAILABILITY STATEMENT Approved for public release; distribution unlimited			12b. DISTRIBUTION CODE	
13. ABSTRACT (Maximum 200 words) The Intravenous Membrane Oxygenator (IMO) at the University of Pittsburgh is intended to provide temporary and portable respiratory support to military and civilian personnel whose lungs are acutely damaged and impaired. The current IMO device consists of several hundred hollow fiber membranes (HFMs) manifolded to gas supply lines for O ₂ delivery, CO ₂ removal, and helium supply to a balloon integrally located within the fiber bundle. Rapid pulsation of the balloon generates additional convective flow of blood across the HFMs and enhances the rate of O ₂ delivery and CO ₂ removal. This report describes key progress in the following areas: 1) hollow fiber membrane evaluation; 2) IMO prototype design development; 3) in-vitro gas exchange performance and characterization of the IMO; and 4) acute and chronic animal studies. The IMO prototypes developed under this contract exchanged O ₂ and CO ₂ at rates equal to or exceeding our design target for gas transfer per fiber surface area. This target is based on attaining 50% of the normal baseline metabolic requirements for O ₂ supply and CO ₂ removal with an IMO device of 0.4 to 0.5 m ² fiber surface area. The next phase of IMO development has already begun and involves scaling-up to full-size IMO devices intended for human implantation.				
14. SUBJECT TERMS Intravenous Oxygenator, Artificial Lung, Respiratory Assist			15. NUMBER OF PAGES 154	
			16. PRICE CODE	
17. SECURITY CLASSIFICATION OF REPORT Unclassified	18. SECURITY CLASSIFICATION OF THIS PAGE Unclassified	19. SECURITY CLASSIFICATION OF ABSTRACT Unclassified	20. LIMITATION OF ABSTRACT Unlimited	

—

7

TABLE OF CONTENTS

FOREWORD.....	i
LIST OF FIGURES.....	iv
LIST OF TABLES.....	viii
1. INTRODUCTION.....	1
1.1 Rationale for an Intravenous Membrane Oxygenator (IMO).....	1
1.2 Design Goals for the IMO Device.....	4
1.3 The Implantable Sized IMO Prototype (IMO-D).....	5
1.4 Overview of Current Development Approach and Report.....	9
2. PRINCIPLES OF EXCHANGE IN THE IMO.....	10
2.1 Effective Exchange Permeability of an IMO Device.....	10
2.2 Hollow Fiber Membrane Permeability.....	11
2.3 Liquid Boundary Layer Permeability.....	16
2.4 IMO Exchange Permeability Design Goal.....	19
3. HOLLOW FIBER MEMBRANE EVALUATION.....	23
3.1 Rationale for HFM Permeability Studies.....	23
3.2 Methods for Determining Fiber Permeability.....	26
3.3 Permeabilities of Commercial Fibers.....	32
3.4 Development of Fiber Coatings.....	36
4. IMO D PROTOTYPE DEVELOPMENT.....	39
4.1 Summary of Prototypes Developed.....	39
4.2 Analysis of Balloon Pulsation.....	42
4.3 Analysis of Sweep Gas Pathway.....	51

5. IN-VITRO GAS EXCHANGE PERFORMANCE.....	56
5.1 In-Vitro Characterization Testing.....	56
5.2 Predicting Gas Exchange in Blood.....	60
5.3 First Improvements in Balloon Pulsation.....	62
5.4 IMO Devices with Kinked Fibers.....	66
5.5 IMO Devices with Modified Helium Pathway.....	67
5.6 IMO Devices with Constrained Fibers.....	76
5.7 Summary of IMO Development History.....	83
6. IN-VIVO IMO STUDIES.....	85
6.1 Experimental Methods.....	85
6.2 Acute Animal Experiments.....	90
6.3 Chronic Animal Implantation Studies.....	105
6.4 Implications of In-Vivo versus In-Vitro Testing.....	110
7. THE NEXT GENERATION IMO (IMO G).....	115
7.1 Design Review of the Current Pneumatic Delivery System.....	115
7.2 Performance of the Improved Pneumatic Delivery System.....	121
7.3 Fiber Fabric Development.....	128
8. SUMMARY AND CONCLUSIONS.....	137
9. REFERENCES.....	140
10. BIBLIOGRAPHY.....	142
11. PERSONNEL.....	144

LIST OF FIGURES

Figure 1.1 Intended <i>in-situ</i> placement of the IMO device.	3
Figure 1.2 Schematic of existing implantable-sized IMO prototype (D series).....	7
Figure 2.1 Illustration of porous and composite hollow fiber membranes.	12
Figure 2.2 Fiber permeability with gas-filled and liquid-filled pores.....	14
Figure 2.3 Growth of diffusional boundary layer on surface contacting flow stream.....	18
Figure 2.4 Implications of transverse versus longitudinal flow to fibers on mass transfer.....	20
Figure 2.5 Relationship between overall IMO exchange permeability, K , and O_2 exchange rate for IMO device in blood.	21
Figure 3.1 Effect of HFM oxygen permeability on the oxygen delivery in blood of an intravenous gas exchange device having a liquid phase permeability, K_l , just great enough to meet the design specification for oxygen delivery.....	24
Figure 3.2 Schematic of diffusion chamber apparatus and components for measurement of hollow fiber membrane permeability.....	27
Figure 3.3 Schematic of diffusion chamber apparatus	28
Figure 3.4 Sample data set used to estimate the carbon dioxide permeability of the TRC composite fiber in water at 37°C.....	31
Figure 3.5 Summary of HFM oxygen and carbon dioxide permeability measurements.....	33
Figure 3.6 Fiber wetting test of coated vs. uncoated fibers using a surfactant	38
Figure 4.1 Schematic of the balloon plethysmograph, designed to analyze balloon pulsation dynamics.....	43
Figure 4.2 (a) Frequency spectrum for the D03 device (unmodified) and (b) D08 prototype (modified.)	44
Figure 4.3 Trade-off between critical frequency and oxygen flow rate for various oxygen inlet tube diameters.....	47
Figure 4.4 Impact of the timing parameters on state of balloon failure.	49
Figure 4.5 Pressure drop - flow rate relationship in IMO series D prototypes (D07 and D08)..	52

Figure 4.6 Distribution of the pressure drop in IMO D device (D02). a) Pre-fiber component, experimental and theoretical; b) Intra-fiber component, experimental and theoretical; c) Post-fiber component.	55
Figure 5.1 Schematic of IMO <i>in-vitro</i> characterization loop.	57
Figure 5.2 Measurement variability associated with sampling and repeated measurement condition.	59
Figure 5.3 Data analysis methodology for estimating O ₂ exchange in blood from measurements of O ₂ exchange in water.	61
Figure 5.4 O ₂ exchange of IMO prototypes in blood versus water. a) Estimates in blood from measurements in water. b) Measurements in blood versus measurements in saline.	63
Figure 5.5 Comparison of O ₂ exchange rates for IMO prototypes before (D03) and after (D04) partial modification of helium pathway.	65
Figure 5.6 Gas exchange performance of IMO prototypes with kinked (D06) and unkinked fibers (D04).	68
Figure 5.7 Gas exchange performance of the D08 series IMO prototypes with the redesigned helium pathway.	69
Figure 5.8 Effect of balloon inflation/deflation timing on O ₂ exchange.	71
Figure 5.9 Gas exchange performance of recent IMO prototype D08 with modified helium pathway and optimal balloon pulsation timing parameters.	73
Figure 5.10 Gas exchange with integral balloon versus a separate stand-alone balloon placed behind the prototype.	75
Figure 5.11 Schematic illustrating loss of relative fiber-fluid motion.	77
Figure 5.12 Improvements in gas exchange during prototype development. Actual bench test measurements and projected <i>in-situ</i> exchange rates.	79
Figure 5.13 Gas exchange performance of the most recent IMO prototype shown in the context of the IMO prototype development history.	82
Figure 5.14 Summary of the developmental history of IMO prototypes in terms of their maximum levels of gas exchange accomplished.	84
Figure 6.1 Schematic of <i>In-vivo</i> experimental setup.	88
Figure 6.2 Gas exchange performance of IMO prototypes in first two acute animal experiments.	91

Figure 6.3 Gas exchange performance in acute animal experiments with continuous heparin infusion.	93
Figure 6.4 Gas exchange performance in acute animal experiment using Carmeda coated IMO device.	95
Figure 6.5 Summary of initial gas exchange rate in acute animal implants.	96
Figure 6.6 Comparison of gas exchange rates in awake versus anesthetized animals during the D07 series <i>in-vivo</i> trials.	97
Figure 6.7 Effects of balloon pulsation <i>in-vivo</i> vs. <i>in-vitro</i>	99
Figure 6.8 Effects of ventilatory challenge on gas exchange <i>in-vivo</i>	100
Figure 6.9 Animal hemodynamics during acute implantation of IMO device.	101
Figure 6.10 Plasma free hemoglobin during acute animal implant.	103
Figure 6.11 Acute <i>in-vivo</i> exchange rates of constrained (D14.2) vs. free fiber (D07.6) devices	104
Figure 6.12 Gas exchange during chronic implantation of IMO devices in D07 series.	106
Figure 6.13 Gas exchange during chronic implantation of IMO device with silicone coated fibers.	108
Figure 6.14 Comparison of gas exchange over time of the silicone coated fiber D09.3 vs. a regular microporous fiber prototype D07.8.	109
Figure 6.15 <i>In-Vivo</i> gas exchange performance of the D14 prototype. The exchange rates appear independant of the balloon pulsation frequency.	111
Figure 6.16 Normalized gas exchange rates of D17-1 at varying beat rates, flow rates, and test section diameters.	113
Figure 7.1 Schematic of the current pneumatic delivery system.	116
Figure 7.2 Predicted average PO ₂ in the fiber bundle of a current design full size IMO prototype.	118
Figure 7.3 Measured and predicted pressure drop across the current design helium pathway. ..	120
Figure 7.4 Schematic of the improved pneumatic delivery system.	122
Figure 7.5 Measured pressure drop of oxygen under positive pressure across the improved O ₂ inlet pathway.	123

Figure 7.6 Measured pressure drop across the helium pathway normalized to fluid properties and gas flow rate.	125
Figure 7.7 Drive pressure required to operate a 70 ml balloon.	126
Figure 7.8 Performance of the improved pneumatic delivery system.	127
Figure 7.9 Engineering mass transfer correlations for cross flow in different hollow fiber modules.	129
Figure 7.10 Scanning electron microscopy picture of the Hoechst Celanese Celgard 240 fiber fabric, our “golden standard” for fiber fabric.....	132
Figure 7.11 The first Prodesco made fiber fabric, Flat Weave B. Crimping of the fibers is apparent.....	133
Figure 7.12 Prodesco made flat weave D fiber mat. The fibers appear less crimped than those of the flat weave B.	134
Figure 7.13 The pressure drop flowrate relationship for gas flow through Prodesco’s Flat Weave D.	135
Figure 8.1 Summary of the current status of IMO development with respect to a planned four-phase development effort required to bring the IMO to clinical trials.	139

LIST OF TABLES

Table 3.1	Summary of fiber properties and permeabilities.....	32
Table 4.1	Prototype summary.....	40
Table 4.2	Dimensions of unmodified D03 helium pathway.....	46
Table 4.3	Dimensions of modified D08 helium pathway.....	46
Table 6.1	Summary of first series of acute <i>in-vivo</i> IMO tests.....	92

1. INTRODUCTION

This is the final report for contract DAMD17-94-C-4052: "Development of a Novel Intravenous Membrane Oxygenator". The report describes progress and highlights of the ongoing development of an intravenous membrane oxygenator (IMO) in the Artificial Lung Laboratory of the McGowan Center for Artificial Organs at the University of Pittsburgh. The University of Pittsburgh IMO device is being designed and developed for the temporary support of soldiers and civilians with acute respiratory failure, whose respiratory systems are unable to maintain adequate gas exchange and who need supplemental support until their lungs return to normal function. For the military, this would include soldiers engaged in chemical warfare with gaseous agents injurious to the lungs. Likewise, as exemplified by the recent terrorist attacks in the subways of Japan, the civilian population is not immune from chemical attack. Although neurotoxic agents were used in the Japanese subway attack, chemicals capable of causing severe pulmonary damage were also available to this terrorist sect. Had they been used, the need for pulmonary support for a large number of civilians would have existed in a setting where the lungs are severely compromised and incapable of adequate gas exchange by traditional ventilator therapy. Accordingly, the availability of a simple device capable of pulmonary support for a large number of potential victims is the military mission for our development of an intravenous membrane oxygenator.

Parts of this introductory section of the final report originally appeared in the annual reports from the project, but are also included in this report for completeness. The introduction here presents the rationale and need for an IMO device, highlights the principal design goals for its development, reviews past IMO prototypes leading to the work described here, and summarizes the overall approach of the development phase funded under this contract.

1.1 Rationale for an Intravenous Membrane Oxygen (IMO)

Adult respiratory distress syndrome (ARDS) refers to hypoxemic (low arterial PO_2) respiratory failure arising from a variety of disorders or insults which increase

pulmonary capillary permeability, cause pulmonary edema and alveolar flooding, and reduce gas exchange as a result. The general therapeutic action for ARDS sufferers is to support gas exchange while treating the acute event or disease precipitating the ARDS response. These ARDS precipitators can range from pneumonia, shock, trauma, fluid aspiration, and inhalation of smoke and toxic gases, to name just a few. Annually, about 150,000 people within the U.S. suffer from ARDS, and the mortality rate for adults remains at about 50% (Fazzalari et al, 1994). An intravenous oxygenator would be of great benefit in treating these patients, as well as soldiers who develop ARDS in combat and other military situations.

The preferred method of treatment for people in end-stage ARDS is mechanical ventilation with high inspired O₂ gas concentration. The positive lung airway pressures and excessive volumes associated with ventilation, however, can lead to barotrauma (eg. pneumothorax), volutrauma, and impairment of cardiovascular function (Weinberger, 1992). Furthermore, high O₂ concentration can be toxic to alveolar cells, especially those responsible for surfactant production. Accordingly, even under optimal conditions, mechanical ventilatory support can lead to a worsening of the state of the ARDS lung and the health of the patient. Patients requiring aggressive mechanical ventilatory support can be supported alternatively with extracorporeal oxygenation (ECMO). However application of ECMO is complicated, labor intensive, expensive, and subject to mechanical failure of the pumping system associated with the oxygenator (Fazzalari et al, 1994). Furthermore, the complicated nature of ECMO makes it an unsuitable therapy for emergency application outside of specially trained and equipped centers.

A clear need exists in standard clinical settings, as well as in adverse settings such as combat, for respiratory assistance therapy that is effective, easy to use, portable and economic. The IMO device being developed at the University of Pittsburgh has the potential to provide such a therapy. The device consists of a bundle of hollow fiber membranes which are manifolded to gas supply and removal lines. A pulsating balloon is centrally located within the fiber bundle to provide enhanced fluid mixing. The device is intended to reside in the inferior vena cava, right atrium and superior vena cava, with the membrane fiber axis parallel to the direction of blood flow (Figure 1.1). The device will be

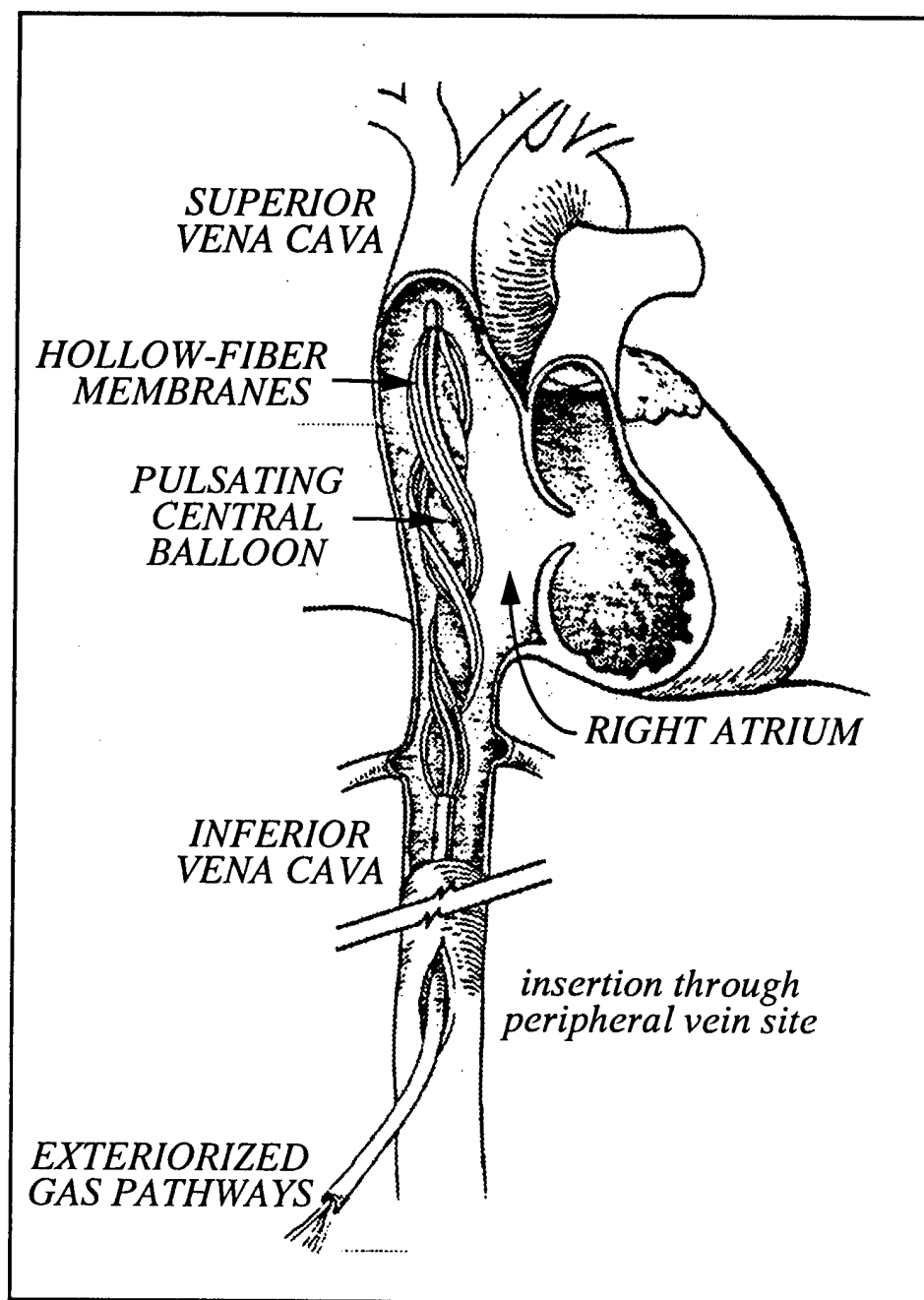


Figure 1.1 Intended *in-situ* placement of the IMO device.

inserted at a femoral vein access site with minor surgery or with percutaneous insertion via a facilitating introducer. Once situated within the vena cava, the IMO device will be capable of augmenting gas exchange at the appropriate level even in end-stage ARDS cases. The device will be relatively portable and user-friendly, and hence will not restrict application to specialized hospitals and support staff. Its ultimate suitability for field hospital use means that the IMO device can be an effective respiratory therapeutic for military personnel with ARDS resulting from combat and/or noncombat related insults.

1.2 Design Goals for the IMO Device

The intravenous membrane oxygenator must be able to exchange sufficient oxygen and carbon dioxide to support respiratory function of end stage ARDS sufferers. What that level of exchange is can be difficult to prescribe, but some guidance is provided by recent clinical findings with the IVOX intravascular oxygenator (Conrad et al., 1994). Based on these studies, we have set the target exchange rate goal for the IMO device as one-half the rate of resting O_2 consumption and CO_2 elimination in normal adults. Average resting exchange rates in adults are 270 ml/min for O_2 and 240 ml/min for CO_2 (Grodins and Yamashiro, 1978). *Accordingly, the IMO device must be capable of exchanging about 120 ml/min to 135 ml/min of O_2 and CO_2 at normal cardiac outputs in the range of 4-6 L/min.*

The insertion and placement of an IMO device within the vena cava gives rise to pertinent size constraints. The device should be insertable into the vena cava through a pathway originating in the femoral vein. Accordingly, the IMO device must be able to assume a maximum diameter of about 1/2" for insertion. Once inserted peripherally and guided into the superior and inferior vena cava, the IMO device must be able to distribute its hollow fiber membranes well within the vena cava cross-section. The more recent IMO prototypes, which will be further described in Section 5 of this report, use constrained fiber bundles rather than the free fiber bundles of earlier prototypes. These constrained fiber IMO prototypes achieve good levels of gas exchange when their fibers are uniformly spaced and well distributed around the central pulsating balloon of the IMO device. Thus,

the IMO design must allow the fibers of the device to be compressed or “furled” into a tight bundle for insertion, but freed for proper fiber distribution once the device is in position within the vena cava. The length of the fiber bundle of an IMO device should be suitable for implantation in a variety of patients. The appropriate length of the fiber bundle for an adult male of average weight and height is estimated at about 35 cm.

The IMO device must also achieve an adequate gas flow rate for CO₂ removal (about 3-5 L/min estimated) under a relatively small vacuum pressure, in order to maximize the transmembrane oxygen tension gradient for O₂ transfer. Since the device achieves effective O₂ delivery and CO₂ removal via active mixing of the blood (via the centrally located balloon), hemolysis and biomechanical-induced cellular trauma should be within acceptable limits. Finally, reliability and durability are required of any prototype that is intended for treatment of ARDS, since the required duration of implant may be two to three weeks. In particular, the IMO device must provide consistent blood oxygenation and carbon dioxide removal while in contact with blood over the intended implant period.

1.3 The Implantable-Sized IMO Prototype

Earlier development work *before the contract period* assessed preliminarily the gas exchange performance of several different IMO prototype designs designated Prototypes A through F (Hattler et al., 1994). The best gas exchange performance in those studies occurred for the Prototype F device, which used a dense fiber mat in a scrolled position around the central balloon. The subsequent development efforts aimed at scaling up Prototype F devices, however, were unsuccessful. The denser fiber mats which were used in Prototype F presented a substantial resistance to blood flow through the device, and the resulting pressure drops were too large to be compatible with the venous circulation. Furthermore, the denser fiber mats of scaled up Prototype F devices would ultimately present substantial difficulties with insertion through a peripheral venous access site, and hence the design itself was ultimately not considered appropriate for development of an implantable version of the device. *Accordingly, the IMO development efforts during the contract period have shifted focus back to the simpler Prototype D device, which presents*

a markedly smaller resistance to blood flow per fiber area compared to other prototypes, and which configures more easily to the maximum size constraint consistent with peripheral venous insertion. Overall, development work on the Prototype D device during the contract period has increased its gas exchange level significantly above that of the earlier Prototype F device, yet the device still remains insertable and would engender a relatively small pressure drop in-situ (Federspiel et al, 1997)

The work under the current contract began with developing the IMO Prototype D into an implantable-sized version of the device. The implantable-sized IMO Prototype D consists of a bundle of narrow hollow fiber membranes which are arranged around a centrally positioned elongated balloon (Figure 1.2; also the IMO depicted in Figure 1.1 represents a Prototype D device). The first versions of this IMO device under the contract (D1 through D14) used freely floating ("free") hollow fibers, wherein the ends of the fibers were potted into gas supply and exhaust manifolds but the fibers were otherwise free and untethered between the manifolds. Towards the end of this contract success was achieved with IMO Prototype D designs based on "constrained" fiber bundles, wherein fibers configured as fabrics or mats were used in place of free fibers. The constrained fiber bundles maintained relatively uniform fiber spacing around the central balloon and led to marked improvements in gas exchange performance. A pneumatic delivery shaft incorporates three gas pathways in a concentric annular fashion to provide the O₂ inlet pathway, the O₂ and CO₂ exhaust pathway and the pathway for balloon pulsation. The balloon is rhythmically inflated and deflated using helium gas and a standard Datascope intra-aortic balloon pump console. The balloon pulsations (inflation/deflation) provide a means for active mixing of blood around the fiber membranes, thus enhancing gas (O₂/CO₂) exchange. The incorporation of a pulsating balloon, which generates three-dimensional convective mixing of the blood flow around the hollow fibers (as confirmed by earlier laser-based flow visualization studies, see Hattler et al, 1992), distinguishes our IMO prototype design from those of others. Nevertheless, successful development of a Prototype D device requires strict optimization of the augmentation of gas exchange associated with balloon pulsation.

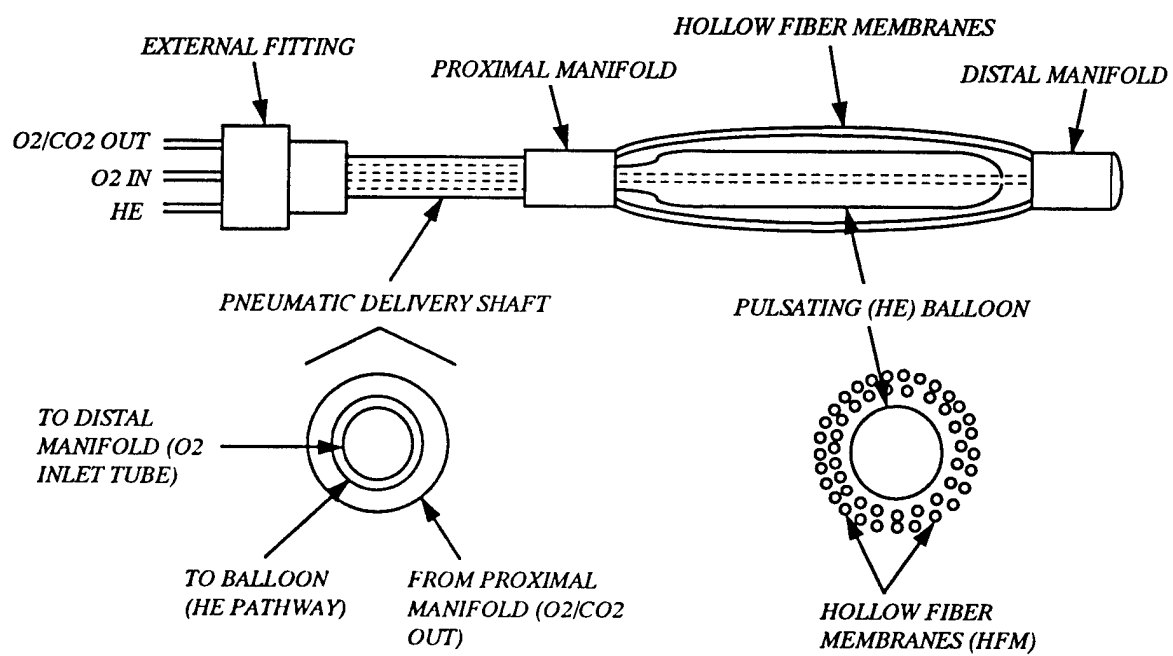


Figure 1.2 Schematic of existing implantable-sized IMO prototype (D series).

Our past development work demonstrated the benefit of balloon pulsation, but we have yet to realize its full potential. The principal resistance to exchange in fiber oxygenators is associated with imperfect mixing in the blood phase subjacent to the fibers (see Section 2). In principle then, increasing the intensity of balloon pulsation will increase mixing and improve exchange rate (up to a limit imposed by the fiber permeability, which would be an exchange rate appreciably above our design goal). Previous prototypes have always seen a clear limit to the augmentation of gas exchange associated with balloon pulsation. Our development work during the contract period focused on systematically identifying, studying and eliminating limitations to gas exchange in IMO prototypes, thus improving the efficiency of gas exchange in the IMO. Part of the gas exchange limitation arose from excessive pneumatic flow resistance in our helium pathway. We found that the resistance of the helium pathway compromised full balloon inflation and deflation (pulsation) above about 60-80 beats per minute. The helium pathway was redesigned in the second year of the contract and the resulting improved IMO prototypes have been extensively studied. These current IMO prototypes can pulsate effectively (i.e. with full balloon inflation and deflation) up to 160-180 beats per minute. As will be further described in this report, performance tests on these newer IMO prototypes indicated that further optimization was needed in constraining and positioning fibers around the central balloon to realize the full benefit of the increased pulsatility of the current IMO prototypes. The experimental evidence provided in this report indicates that *a D series prototype IMO device with optimized balloon pulsation, fiber constraint and positioning around the balloon produces sufficient exchange augmentation that will enable us to achieve the requisite O_2/CO_2 exchange for effective treatment of ARDS.* Based on the testing, evaluation, and development of IMO prototypes under the current contract we have demonstrated proof-of-principle for the IMO in scaled-down devices, with fiber bundle lengths half of what would be implantable in human adults. We have already begun the next step of scaling up the implantable IMO prototypes to full operational size and of demonstrating sufficient gas exchange levels in the full-size IMO devices.

1.4 Overview of Current Development Approach and Report

The IMO developmental approach used during this contract has been designed to facilitate prototype design changes, and to expedite careful and extensive device evaluation, which then enabled systematic device evolution. The testing phase consisted of extensive bench testing, and acute and chronic animal testing in calves. The overall approach can be broadly categorized as follows:

- 1) Studies to evaluate and develop candidate hollow fiber membranes for the IMO design. These studies are described in Chapter 3.
- 2) Studies characterizing the pneumatic performance of the IMO devices *in-vitro* with respect to balloon pulsation and the gas flow dynamics of the sweep gas pathway. These studies are described in Chapter 4.
- 3) Studies of the gas exchange capacity and performance of IMO devices in bench characterization tests during the development phase. These studies are described in Chapter 5.
- 4) Studies which examine IMO device performance *in-vivo* in both acute and chronic implantations into calves of similar size to adult humans. These studies are described in Chapter 6.

The testing and development work described above demonstrated proof-of-principle for the IMO in scaled-down prototypes (shorter fiber bundle lengths than ultimately could be implanted). The scale-up of the IMO to full-size devices is described in Chapter 7.

2. PRINCIPLES OF EXCHANGE IN THE IMO

This section briefly reviews the theoretical background relevant to gas exchange in IMO devices. It is based on an introductory section presented originally in the first annual report and have been revised and presented again here for completeness. This background will be useful to the discussions in subsequent sections concerning IMO device performance *in-vitro* and *in-vivo*, and evaluation of candidate hollow fiber membranes. Most importantly, the concept of an effective exchange permeability for an IMO device is introduced and is related to its principal underlying determinants: the fiber membrane permeability and the liquid-side (blood-side) boundary layer permeability. The effective gas exchange permeability of an IMO device represents a mass transport coefficient for overall gas exchange. As such, it provides a useful gauge for evaluating the efficiency of gas exchange associated with the device, and for interpreting performance and evaluating progress during IMO device development.

2.1 Effective Exchange Permeability of an IMO

The effective or overall exchange permeability, K , of an IMO device represents the rate of gas exchange normalized to fiber surface area and to the gas partial pressure differences driving exchange. Focusing on O_2 as the species of interest, the overall IMO device O_2 exchange rate, VO_2 , is given by

$$VO_2 = KA(\overline{P}_g - \overline{P}_l)$$

where \overline{P}_g and \overline{P}_l are the *average* O_2 partial pressures¹ in the gas and liquid (blood) phases, respectively, and A is the fiber membrane surface area. A similar relationship can be written to define the effective exchange permeability of the device for CO_2 . The effective exchange permeability of an IMO device represents a useful parameter for interpreting results because it most closely reflects transport *diffusional resistance* to gas exchange, with permeability and

¹ Relating the average partial pressures in the blood or gas phases to the blood and gas inlet and outlet partial pressures goes beyond the scope of this summary. Nevertheless, a simple arithmetic average of inlet and outlet partial pressures often provides a useful estimate of exchange performance in an IMO device.

resistance being inversely related. Accordingly, permeability provides a measure of the relative efficiency of gas exchange of an IMO device, independent of other issues such as convective flow.

In general, because of imperfect convective mixing within blood and gas phases, exchange involves diffusion not only through the fiber wall, but through the gas and blood phases as well. The diffusion coefficient within the gas phase is relatively large, however, and so transport resistance there can generally be neglected. Accordingly, the overall permeability of an IMO device has two principal determinants:

$$\frac{1}{K} = \frac{1}{K_m} + \frac{1}{K_l}$$

where K_m , and K_l represent the individual permeabilities of the fiber membrane and liquid (blood) phases, respectively. The reciprocal relation arises because the individual contributions represent resistances in series, which add directly to determine overall resistance. One implication of the relationship above is that the overall permeability, K , is always less than the smallest of the permeabilities, K_m , and K_l . In simple terms, the transport process with the smallest permeability controls gas exchange in the overall device. Thus, development efforts should always focus principally on increasing the smallest permeability associated with the device.

2.2 Hollow Fiber Membrane Permeability

Hollow Fiber Membranes. Hollow fiber membranes (HFMs) can be categorized according to different wall morphologies (Figure 2.1). Porous fiber membranes are the most common HFMs used for oxygenator design. The porous HFMs have fixed submicron pores within the wall that are contiguous from outer to inner lumen. Accordingly, the polymer material generally does not determine exchange performance and behavior as much as the pore size and characteristics. The key parameters in this regard are the mean pore size, d_p , and the wall porosity, ϵ , which represents the fractional wall volume consisting of pores. One important polymer-related fiber property is the hydrophobic versus hydrophilic nature of the fiber. Generally, hydrophobic fibers are used in oxygenators because they resist fluid wetting under normal transmural pressure differences. As will be elucidated below, fiber wetting can markedly reduce the exchange permeability of the fiber.

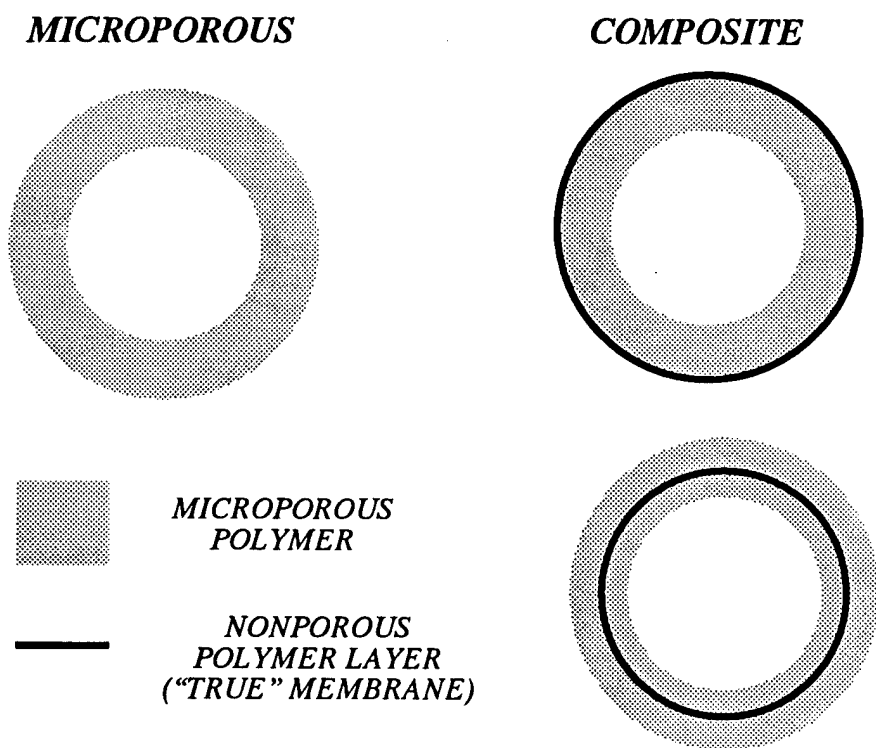


Figure 2.1 Illustration of porous and composite hollow fiber membranes.

The composite fibers employ a thin true membrane (nonporous polymer layer) for liquid and gas segregation within a porous wall for mechanical support and optimal gas permeability. Figure 2.1 illustrates a composite fiber which has a nonporous polymer coating on the outside (coated fiber), as well as a composite fiber with the nonporous polymer layer sandwiched in the middle of the microporous wall. To the best of our knowledge the latter type of composite fiber is commercially available only as the Mitsubishi MHF fiber.

Gas Permeability of Hollow Fiber Membranes. Predicting the exchange capacity of a particular HFM requires knowing the permeability, K_m , of the fiber membrane. This value is not usually available, however, in the specifications provided by the fiber manufacturer. Indeed K_m values can be difficult to determine experimentally for several reasons. If K_m is measured in a system with gas on one side of the membrane and liquid on the other, the measurement is easily affected by unmixed liquid boundary layers adjacent to the surface of the fiber wall. These unmixed boundary layers present an additional resistance to diffusion, and hence reduce the effective permeability measured. If K_m is measured in a system with gas on both sides of the membrane, bulk gas flow can occur through the walls of porous fibers if total pressure is not the same on both sides of the membrane. Thus, the measured permeability may be appreciably larger than if a liquid were on one side of the membrane, as in the actual case for the IMO device.

The theoretically expected values of hollow fiber permeability are illustrated in Figure 2.2. In the limit of completely gas filled pores diffusion theory predicts that fiber permeability depends on fiber wall porosity, ϵ , thickness, h , pore tortuosity, τ , and the value of the Knudsen diffusion coefficient in the gas phase, D_g . For representative values of these parameters relevant to available hollow fiber membranes a fiber permeability of $K_m \sim 10^{-2}$ ml O_2 /cm²/s/cmHg is predicted. Indeed Kamo *et al.* (1990) reported an experimentally measured value of 6.7×10^{-2} ml O_2 /cm²/s/cmHg for the Mitsubishi KPF fiber in gas-membrane-gas system. A permeability value of $K_m \sim 10^{-2}$ ml O_2 /cm²/s/cmHg for porous HFMs represents an enormous O_2 exchange capacity which is never realized in an oxygenator device. Putting this value in perspective, an

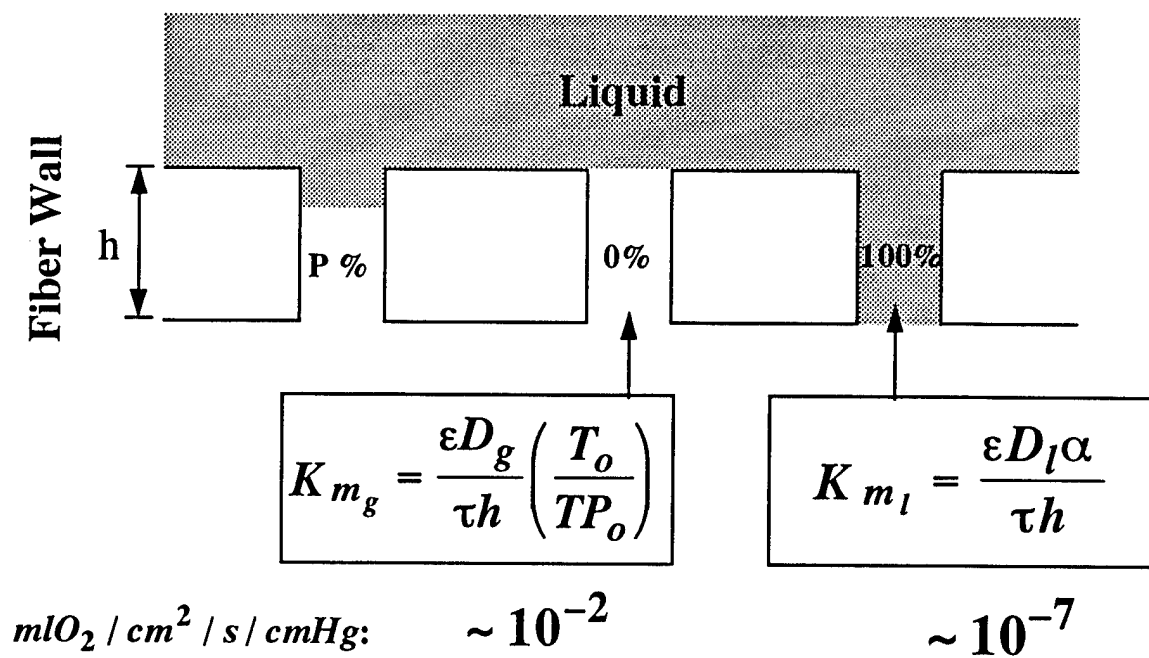


Figure 2.2 Fiber permeability with gas-filled and liquid-filled pores.

IMO device with 0.5 m^2 surface area of these fibers, and with an average 70cmHg PO_2 difference between the gas and blood phases, could transfer approximately 200 L/min of O_2 across the membrane, a transfer capacity much greater than needed to saturate blood flowing at physiological flowrates. This exchange rate is several thousand fold greater than actually occurs because substantial resistance to exchange resides within the blood phase, in small imperfectly mixed boundary layers adjacent to the fiber wall surfaces. Hence, the overall effective exchange permeability within an IMO device is substantially less than the permeability of the individual porous HFMs composing the device.

Liquid infiltration into gas filled pores can markedly diminish the exchange performance of an HFM. Even with hydrophobic HFMs, evidence suggests that the pores do not remain completely gas filled, but that liquid does penetrate into the fiber wall (Qi and Cussler, 1985). For entirely liquid filled pores (Figure 2.2), the fiber membrane permeability, K_m , depends on the solubility, α , and the diffusion coefficient, D_l , of the diffusing gas in the liquid filling the pores (as well as on fiber wall porosity and pore tortuosity, as for the gas-filled pores). Hence the value of K_m is markedly reduced because the diffusion coefficient for O_2 in water is about $2 \times 10^{-5} \text{ cm}^2/\text{s}$, substantially less than that in gas, and because the capacity (or solubility) of O_2 in a liquid is small. For the same pore tortuosity and membrane thickness as in the previous example, diffusion theory for O_2 diffusion through water filled pores predicts a fiber permeability of $K_m \sim 10^{-7} \text{ ml O}_2/\text{cm}^2/\text{s}/\text{cmHg}$, a reduction in exchange capacity of nearly 5 orders of magnitude compared to gas-filled pores within the fiber wall. Thus, there is a clear benefit to using hydrophobic HFMs with nonwetting properties in an IMO device. Even so, Qi and Cussler (1985) measured K_m for the Celgard X20, a polypropylene hydrophobic porous HFM, and concluded that the situation rests somewhere between gas-filled and liquid-filled pores. Their measured K_m value (converted to units used here) was $K_m \sim 2 \times 10^{-4} \text{ ml O}_2/\text{cm}^2/\text{s}/\text{cmHg}$.

The permeability of a composite HFM is markedly affected by the characteristics of the true membrane used within the porous fiber wall. In general, homogeneous polymer films have low gas permeabilities. Permeation of a gas species across nonporous polymers involves

absorption of gas molecules on the polymer surface, diffusion through the polymer molecular matrix, and desorption of the gas species at the opposite surface. Kamo *et al.* (1990) measured the membrane permeabilities of the Mitsubishi composite HFMs. The MHF M series incorporates a 1/2 micron polyurethane true membrane and had $K_m = 1.6 \times 10^{-5}$ ml $O_2/cm^2/s/cmHg$. The MHF L series, with a 1 micron polyurethane true membrane, had $K_m = 0.9 \times 10^{-6}$ ml $O_2/cm^2/s/cmHg$. These permeabilities are markedly smaller than those applicable to porous HFMs and indicate that the true membrane component of composite HFMs dictate the overall exchange permeability of the fiber.

2.3 Liquid Boundary Layer Permeability

The liquid (blood) phase permeability, K_l , accounts for diffusion from the fiber surface through the imperfectly mixed liquid boundary layers which arise adjacent to the fiber surfaces. Even a relatively small (micron size) unmixed liquid layer can reduce K_l appreciably below the fiber K_m , and limit overall exchange. Furthermore, generating convective mixing on the scale of microns subjacent to a surface is difficult, and so diffusional boundary layers will always be present and will impact upon exchange. For simple liquids like water, the permeability of a liquid boundary layer of thickness δ_{bl} can be expressed as

$$K_l = \frac{\alpha D}{\delta_{bl}}$$

where α and D are the gas solubility and diffusion coefficient in the liquid respectively. The liquid boundary layer thickness, δ_{bl} , can be considered an average distance that the gas must diffuse away from the fiber before being swept out of the IMO device by the bulk flow of liquid. Accordingly, the value of δ_{bl} depends principally on the flow dynamics in the liquid phase, which is complicated in the IMO device. The principal role of balloon pulsation in the IMO device is to maximize convective mixing within the blood phase so that the diffusional boundary layer thickness is minimized, and the permeability maximized.

Generally, the permeability of the liquid boundary dominates (limits) exchange in oxygenator devices. For example, the K_l value for O_2 diffusing through a water boundary layer of 10 micron in thickness is about 9×10^{-6} ml $O_2/cm^2/s/cmHg$. Assuming a hydrophobic porous fiber, the value for K_m is in the range of 10^{-2} to 10^{-5} ml $O_2/cm^2/s/cmHg$, provided the fiber is not completely wetted. Accordingly, a liquid boundary layer of 10 micron, just a fraction of the fiber size, has an O_2 permeability appreciably below that of the fiber membrane, or $K_l \ll K_m$. Under these conditions, the overall IMO gas exchange permeability would be dictated by the liquid boundary layer, and

$$K \approx K_l.$$

Only under conditions of markedly reduced K_m , as would accompany for example complete fiber wetting, would the permeability of a porous HFM have an appreciable influence on IMO exchange performance. Nevertheless, we include K_m in the overall exchange relation as a reminder that fiber permeability can potentially affect exchange performance. The permeability of composite hollow fiber membranes is reduced by the presence of the true membrane and may become comparable to that of the liquid boundary layer. For example, the permeability of the Mitsubishi composite fiber falls in the range of 10^{-6} ml $O_2/cm^2/s/cmHg$. As a result, the overall exchange rate in an IMO device utilizing these composite fibers can potentially be affected by the permeability of the fibers themselves. These issues are important to the IMO development process and will be discussed further when results from fiber permeability studies are presented in Section 3 of this report.

The dependence of the liquid boundary layer permeability on the boundary layer thickness has important implications for design of fiber modules in an artificial lung. Simple boundary layer theory for a developing mass transfer boundary layer along a flat surface predicts that the boundary layer grows as the square root of distance along the surface (Figure 2.3). Thus, the permeability of the liquid boundary layer varies as $K_l \sim l^{-1/2}$ and considerable advantage can be gained from orienting the exchange surfaces to minimize this length l . For hollow fiber membranes this translates to generating flow perpendicular (transverse) rather than parallel (longitudinal) to

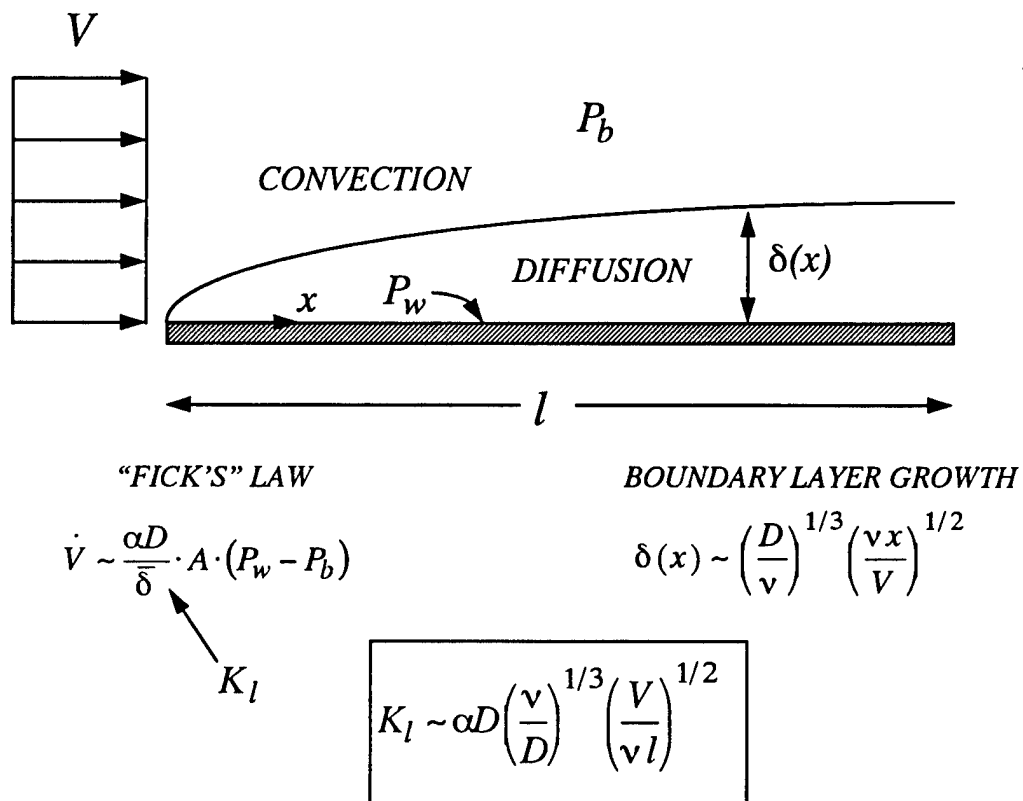


Figure 2.3 Growth of diffusional boundary layer on surface contacting flow stream.

the fiber axes. With transverse flow to the fibers, the fiber surface along the flow direction scales as the diameter, d , of the fibers, while with longitudinal flow the fiber surface along the flow direction scales as the length L of the fiber. Thus simple boundary layer theory predicts that the ratio of gas exchange permeability in transverse versus longitudinal flow would be

$$K_i^{trans} / K_i^{long} \sim \sqrt{L/d}$$

For fiber lengths and diameters characteristic of an intravenous oxygenator ($L/d \sim 1000$) this translates into an advantage for transverse flow of at least ten-fold (Figure 2.4)

2.4 IMO Exchange Permeability Design Goal

The design goal for O_2 exchange rate in an IMO can also be expressed as the required effective permeability, K , of a device accomplishing the desired exchange. This involves rearranging Eq. 2.1, and for a given VO_2 , estimating the mean O_2 partial pressures within the gas and blood phases under typical operation. The mean O_2 partial pressure within the gas phase is relatively simple to estimate. Gas enters the IMO device at 100% O_2 and leaves with only minor dilution by CO_2 . Assuming that gas flows under a vacuum pressure of 25 cmHg relative to atmospheric pressure ($P_0=76$ cmHg), the mean O_2 gas tension within the gas phase would be about 62 cmHg. Estimating the mean O_2 partial pressure in the blood phase requires specifying the blood flow rate, the inlet blood PO_2 (venous PO_2), and the relationship between blood O_2 content and partial pressure (i.e. the blood O_2 capacity curve, which accounts for the oxygen carrying capacity of hemoglobin and for dissolved oxygen; see Reeder, 1986). Thus, for a given O_2 exchange rate and blood flowrate, the change in O_2 content of blood can be computed. Then, using the inlet (or venous) PO_2 and the blood O_2 capacity curve, the outlet (or arterial) PO_2 can be computed and used to determine the mean blood O_2 partial pressure required for Eq. 2.1.

The relationship between the effective permeability, K , of an IMO device and the resulting O_2 exchange rate, VO_2 , is shown in Figure 2.5. The blood parameters used in Figure 2.5 correspond to standard AAMI conditions for testing blood oxygenators, with a blood flow of 4

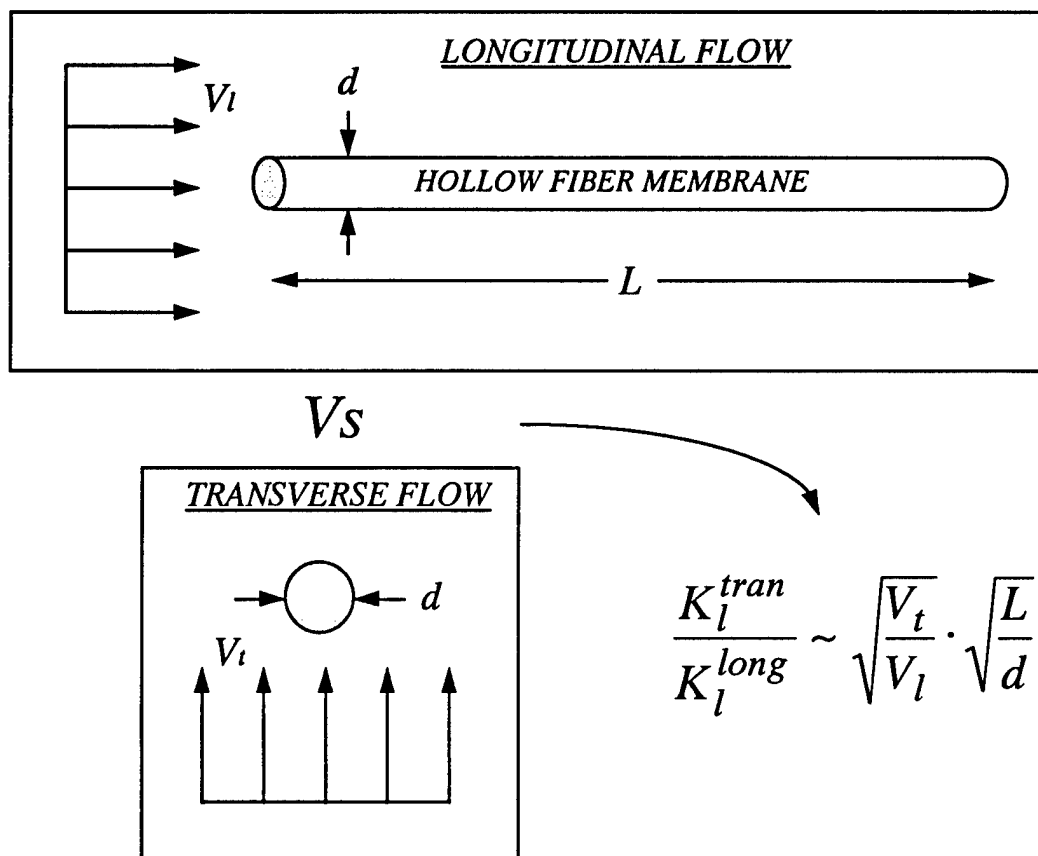


Figure 2.4 Implications of transverse versus longitudinal flow to fibers on mass transfer.

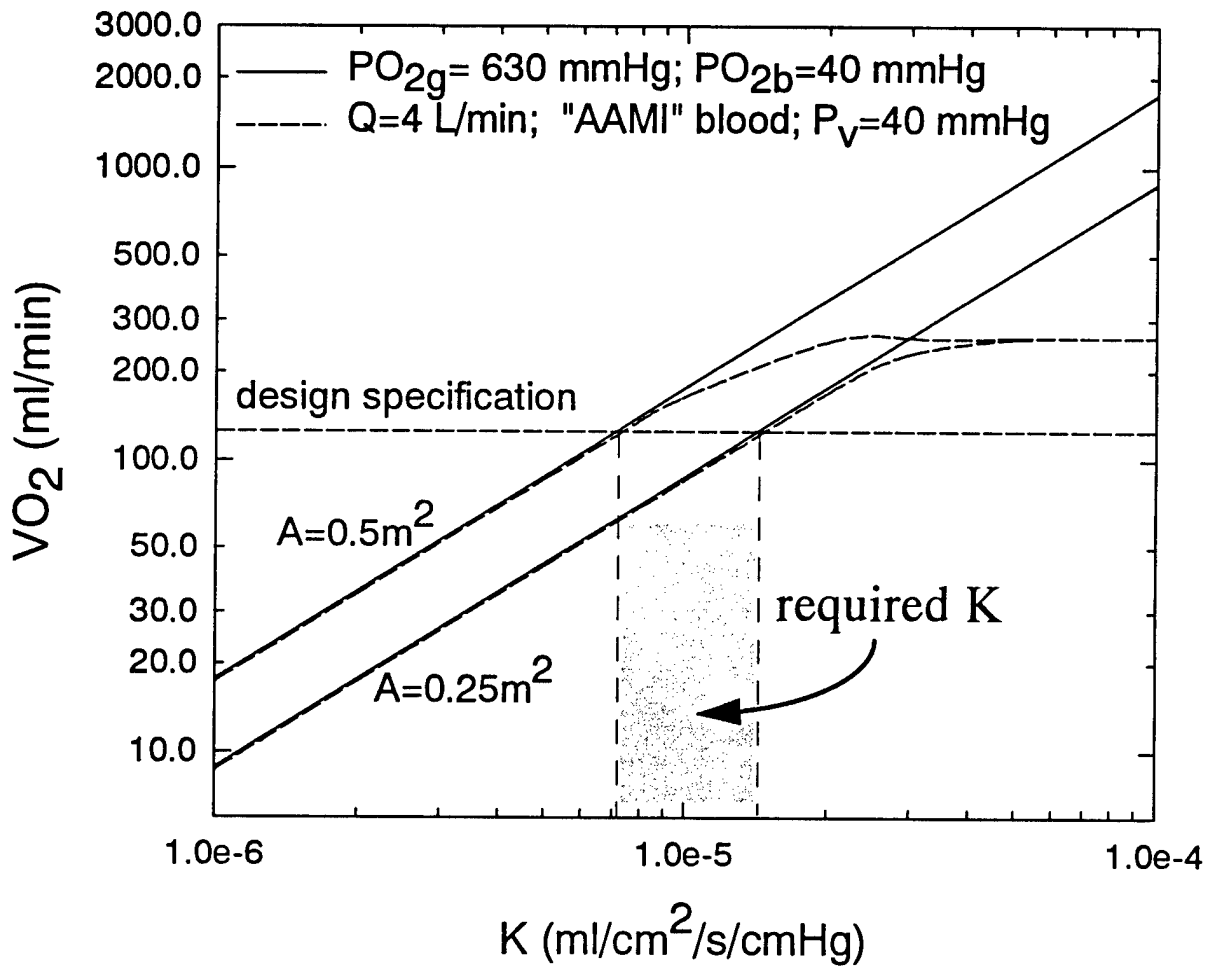


Figure 2.5 Relationship between overall IMO exchange permeability, K , and O_2 exchange rate for IMO device in blood.

L/min and an inlet blood PO_2 of 40 mmHg. Relationships are shown for IMO devices with total fiber surface areas, A , of $0.5m^2$ and $0.25m^2$, and the level of oxygen exchange corresponding to our design goal is indicated. Accordingly, this analysis indicates that an IMO device with fiber area in the range indicated requires an overall exchange permeability, K , in the range:

$$7 \times 10^{-6} \text{ ml O}_2 / \text{cm}^2 / \text{s} / \text{cmHg} \leq K \leq 1.5 \times 10^{-5} \text{ ml O}_2 / \text{cm}^2 / \text{s} / \text{cmHg}.$$

This permeability range provides an alternative gauge, in addition to VO_2 and the area normalized VO_2 , for assessing progress during the IMO development phase.

3. HOLLOW FIBER MEMBRANE EVALUATION

3.1 Rationale for HFM Permeability Studies

The fundamental gas exchange element of the IMO is the hollow fiber membrane (HFM). Extracorporeal artificial lungs in use clinically employ thousands of microporous-walled HFMs in ensemble arrangements or bundles which vary among the designs. Indeed, the delivery rate of oxygen and the removal rate of carbon dioxide depend directly on the gas species dependent mass transfer coefficient (or in perfusion nomenclature, the overall gas exchange permeability) of the HFM bundle constituting the artificial lung device. The overall gas exchange permeability, K (refer to equation in Chapter 2), of any oxygenator device represents the serial mass transfer resistances associated with the gas phase flowing through the fibers, with the fiber wall, and with the blood phase flowing through the interstices of the fiber bundle. In practice, mass transfer resistance of the gas phase is negligible, and typically in extracorporeal oxygenators, so is that associated with the HFM wall. However, the gas permeability of hollow fiber membranes assumes considerably greater importance in the design of an intravenous artificial lung device such as the IMO. Because the IMO must reside within the vena cava and not restrict blood flow returning to the heart, the total fiber surface area is approximately 4-6 times less than that of extracorporeal devices. Thus, design strategies for meeting gas transfer requirements rely on mechanisms for increasing convective mixing in the blood and reducing blood-side mass transfer resistance.

The natural result of reducing blood-side mass transfer resistance is to increase the effect of fiber wall resistance on the overall device permeability. To illustrate this point, Figure 3.1 shows a plot of the rate of oxygen delivery of a typical intravenous gas exchange device as a function of the permeability of the fibers used. In order to deliver 135 ml $O_{2(STP)}/\text{min}$ (IMO design goal), a device consisting of 0.5 m² of fiber surface area must have a liquid boundary layer permeability of approximately 1×10^{-5} ml/s/cm²/cmHg, assuming very high membrane permeability. However, as seen in Figure 3.1, as the membrane permeability for this device drops to 1×10^{-4} ml/s/cm²/cmHg, it begins to affect the delivery rate of the device and at 2×10^{-5} ml/s/cm²/cmHg, it reduces the delivery rate

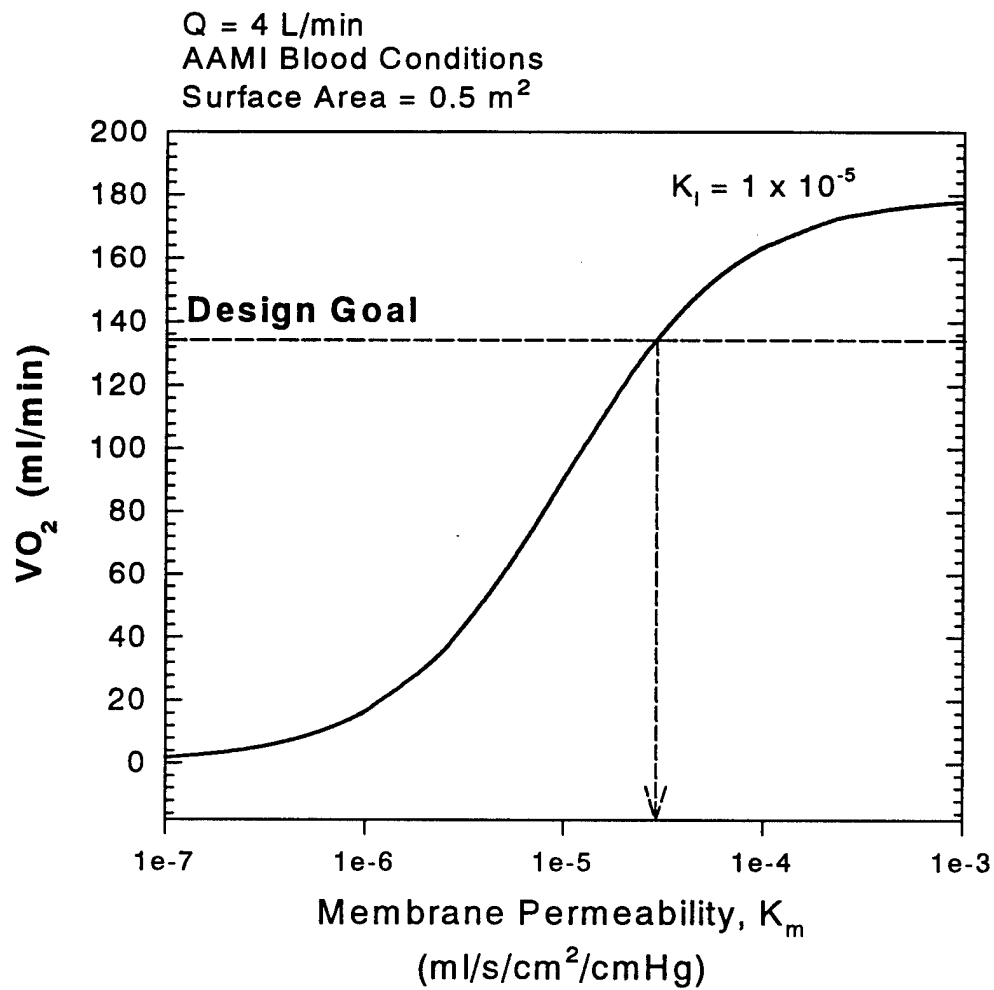


Figure 3.1 Effect of HFM oxygen permeability on the oxygen delivery in blood of an intravenous gas exchange device having a liquid phase permeability, K_l , just great enough to meet the design specification for oxygen delivery.

to below the design specification. This means that membrane permeability cannot necessarily be ignored, and in fact, the best HFMs commercially available for use with intravenous gas exchange devices have oxygen permeabilities in the range of 8×10^{-6} to 4×10^{-5} ml/s/cm²/cmHg (Lund et al, 1996) which fall right into the region of influence.

Fibers selected for intracorporeal oxygenators must furthermore be resistant to wetting of membrane walls by blood serum, a common problem in extracorporeal oxygenators which can lead to device failure within days. Strategies for resistance or blockage of wetting include using fibers with markedly reduced pore size and/or composite fibers consisting of a thin nonporous (true) membrane layer either coating the exterior of, or sandwiched within, a standard microporous wall. In both cases, the very strategies meant to resist fluid wetting also diminish fiber wall permeability. This is especially so in composite fibers, where the nonporous polymer layer can represent an appreciable impediment to diffusion.

Accordingly, selection of an appropriate hollow fiber membrane the IMO requires knowing the gas permeability of the candidate fibers and ensuring that fiber permeability does not potentially compromise gas exchange within the artificial lung device. A simple measurement apparatus and methodology was developed to measure hollow fiber membrane permeability in a *gas-liquid* environment (gas on one side of the fiber wall, liquid on the other) similar to that which the fibers of the IMO would be exposed. For microporous fibers, permeability measurements made in a gas-gas system, although much easier, would be enhanced by convective flow through the pores of the fiber walls due to unavoidable pressure differences in the gas outside of the fibers versus that on the inside. Furthermore, gas-gas measurements would fail to reflect interactions of the fluid with the membrane surface characteristics which might effect fiber performance, even for composite fiber types. Thus accurate assessment of fiber performance for use with the IMO requires evaluation in a similar environment.

The permeability measurement apparatus was used to measure the oxygen and carbon dioxide permeabilities of a variety of HFM types, both microporous and composite. Most of the fibers tested are available commercially, however, some were developed privately for specific purposes and provided to us in small samples for research.

3.2 Methods for Determining Fiber Permeability

The principal components of the fiber permeability measurement procedure are depicted in Figure 3.2. The central component is a diffusion chamber (Figure 3.3) which consists of a parallel arrangement of hollow fiber membranes submerged in a stirred liquid bath of fixed volume (300 cc). For each membrane type, approximately 90 fibers of 10 centimeters in length are manifolded in a parallel arrangement to gas flow channels extending from interchangeable lids mounted to the diffusion chamber with screws. The temperature of the liquid bathing the fibers is controlled at 37°C by flowing water from a constant temperature circulating bath through a small steel tube heat exchanger fixed within the liquid volume. The diffusion chamber is also equipped with compliance balloons for accommodating small liquid volume changes and sealed ports for insertion of a temperature sensor. The liquid is stirred by a quadruple pitched-blade stainless steel impeller, 6 cm in diameter, attached to a shaft which passes through an O-ring bearing at the base of the chamber. The chamber is positioned above and coupled to a 1/8 HP (1800 rpm) dc motor driven by a speed controller. The stir rate is measured by using the Hall effect sensor of an electromagnetic tachometer.

The permeability of the system is determined by studying the rate at which the test gas of interest is removed through the fibers from the initially saturated liquid volume. The system permeability is a function not only of the permeability of the fiber wall but also of the liquid boundary layer at the surface of the fibers. By varying the level of stirring of the liquid bathing the fibers, the liquid boundary layer can be reduced. Extrapolating the system permeability measurements to an infinite level of stirring effectively eliminates the liquid boundary layer component to the system permeability thus revealing the fiber permeability.

To measure the system permeability for a given stir rate, the liquid bath is first equilibrated with high concentrations of the test gas of interest, using either 100% oxygen or carbon dioxide gas drawn under vacuum through the lumen of the fibers. Then, at time

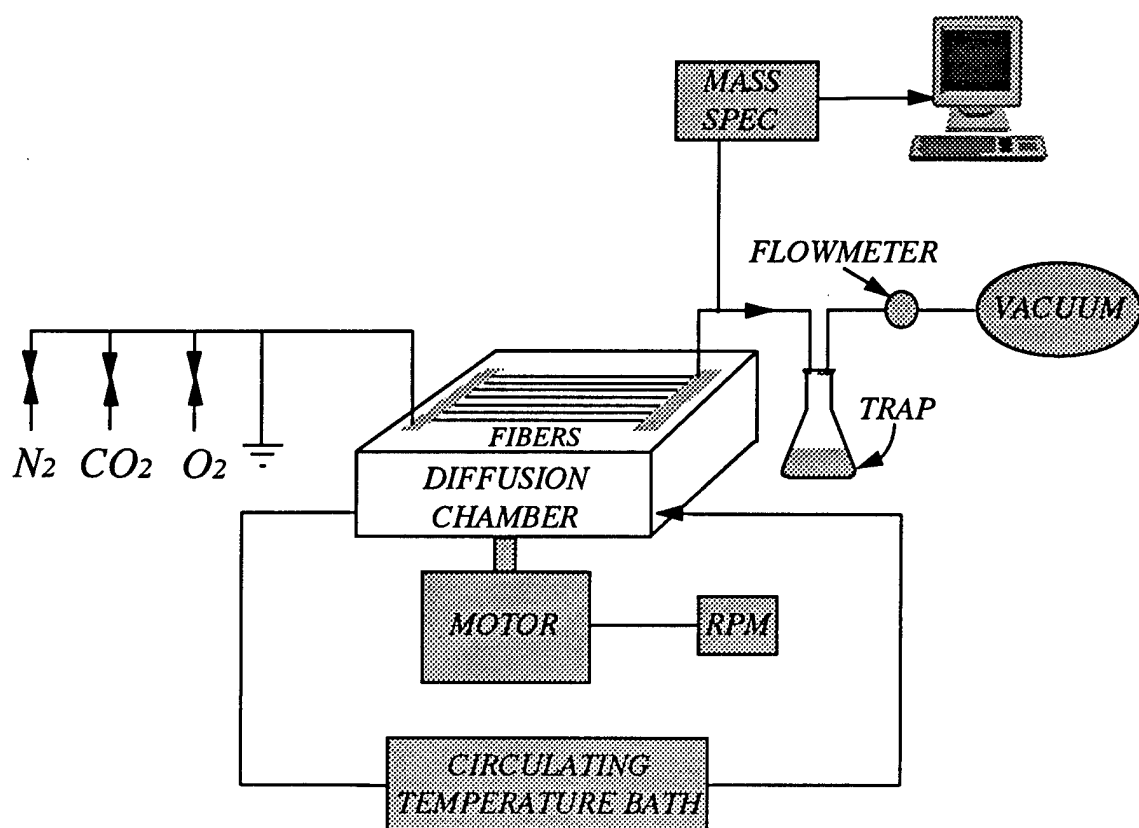


Figure 3.2 Schematic of diffusion chamber apparatus and components for measurement of hollow fiber membrane permeability.

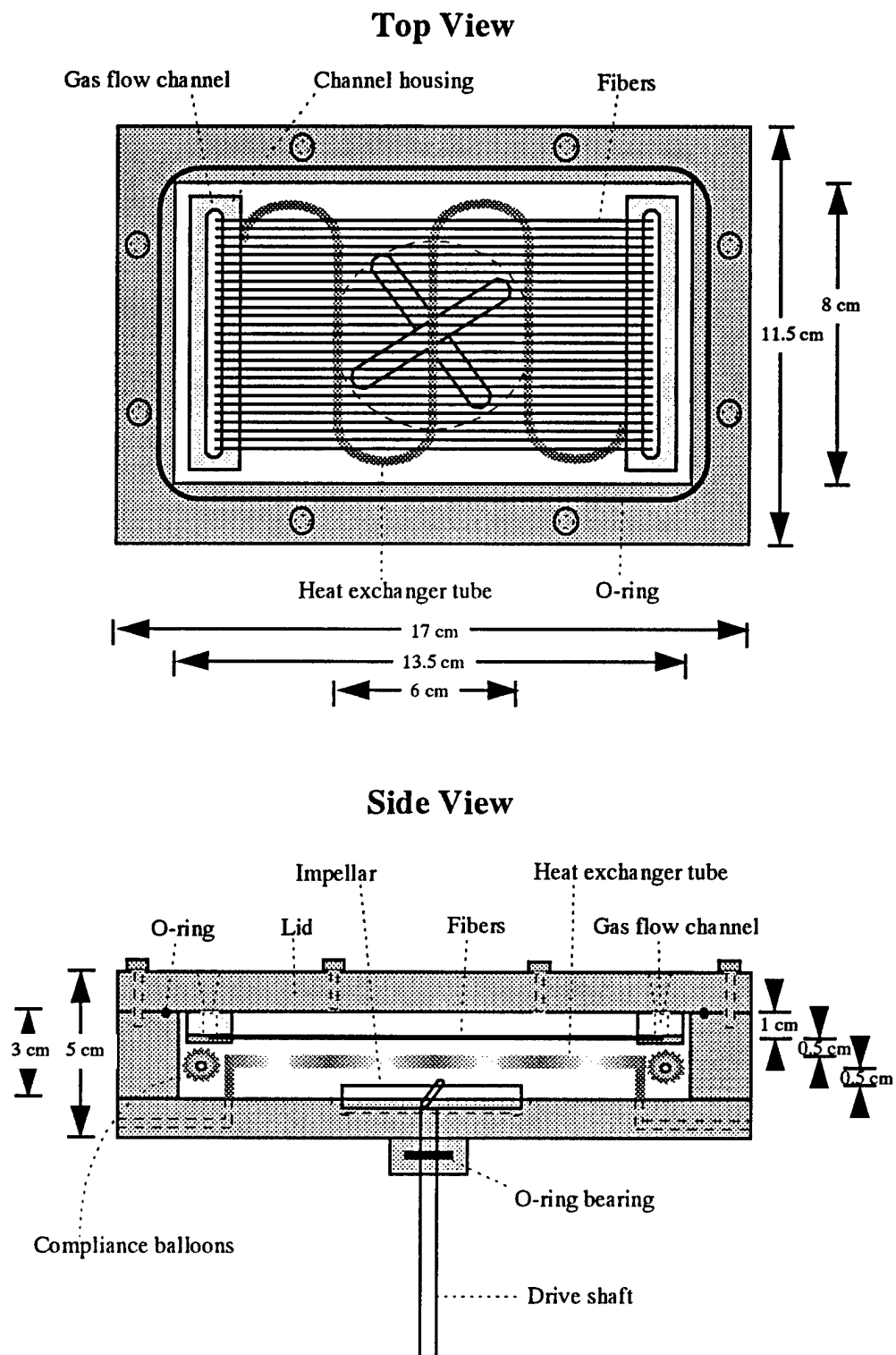


Figure 3.3 Schematic of diffusion chamber apparatus

zero, the fiber gas source is switched to pure nitrogen to flush the system of test gas, and the change in test gas concentrations (O_2 or CO_2) exiting the fiber bank is continuously measured using a medical gas analyzer (Marquette Electronics, Milwaukee, WI) and recorded on a personal computer with an A/D board. The rate of the exponential washout of O_2 or CO_2 from the diffusion chamber is determined from these measurements and used to calculate the effective permeability of the fiber-liquid system, and to estimate the fiber membrane permeability, as described below.

Calculation of Effective System Permeability From conservation of mass, the governing equation for species mass transfer from the liquid into the fiber is given by:

$$\alpha V \frac{dP_o}{dt} = -KA[P_o(t) - \bar{P}_i(t)] \quad (3.1)$$

where $P_o(t)$ is the partial pressure of the gas species in the liquid at time t , and $\bar{P}_i(t) = \frac{1}{L} \int_L P_i(z,t) dz$, and is the average test gas partial pressure within the fibers, K is the effective, or overall, system permeability, A is the fiber surface area, V is the volume of liquid in the chamber and α is the solubility of the test gas in the liquid. Accordingly, the solutions for the test gas partial pressures in the liquid and in the fiber are given by,

$$P_o(t) = P_o^i e^{-\lambda t}, \text{ and } P_i(z,t) = P_i^i(z) e^{-\lambda t} \quad (3.2)$$

where P_o^i is the partial pressure of the mass species in the liquid at $t = 0$, and $P_i^i(z)$ is the partial pressure distribution of the mass species in the fiber at $t = 0$, and λ is the exponential washout rate constant. Substituting Eqs. 3.2 into 3.1 yields the following expression for the rate constant λ ,

$$\lambda = \frac{KA}{\alpha V} \left[1 - \frac{\bar{P}_i^i}{P_o^i} \right] \quad (3.3)$$

where \bar{P}_i^i represents the average of $P_i^i(z)$ over the fiber length. If the rate of flush gas flow through the fibers is sufficiently high, then the average partial pressure of the test gas

within the fibers will remain appreciably below that within the liquid, and $\bar{P}_i^i / P_o^i \ll 1$. Under these conditions, the washout rate constant is directly proportional to the system permeability,

$$\lambda = \frac{KA}{\alpha V} \quad (3.4)$$

and is independent of the flush gas flow rate through the inside of the fibers. Thus equation 3.4 can be used directly to determine the overall system permeability, K , from the measured rate constant, λ .

Calculation of Membrane Permeability The total resistance to mass transfer in the liquid-fiber system is the inverse of the overall system permeability, K . As such, $1/K$ is determined by the sum of the resistances of the membrane and liquid boundary layers in series:

$$\frac{1}{K} = \frac{1}{K_m} + \frac{1}{K_l} \quad (3.5)$$

where K_m and K_l are the respective permeabilities of these phases. A general correlation for the liquid boundary layer permeability would be of the form $K_l = \hat{a} Re^\beta Sc^\gamma$, where \hat{a} , β , and γ are constants, Re is the Reynolds number, and Sc is the Schmidt number (Bird, Stewart, and Lightfoot, 1960). An appropriate characteristic velocity in Re is ΩL , the product of stir bar rotation rate and length. Thus, for a given fluid and stir bar/diffusion chamber geometry, the liquid boundary layer permeability simplifies to $K_l = a\Omega^\beta$, where a is a constant dependent on fluid, gas species and geometric parameters, and the correlation exponent, β , is a property of the liquid flow pattern within the diffusion chamber. Substituting for K_l , Eq. 3.5 becomes,

$$\frac{1}{K} = \frac{1}{K_m} + \frac{1}{a\Omega^\beta} \quad (3.6)$$

By using nonlinear regression to fit Eq. 3.6 to measured values of K versus Ω , the parameters K_m , a , and β can be determined. Figure 3.4 shows a sample set of K versus Ω

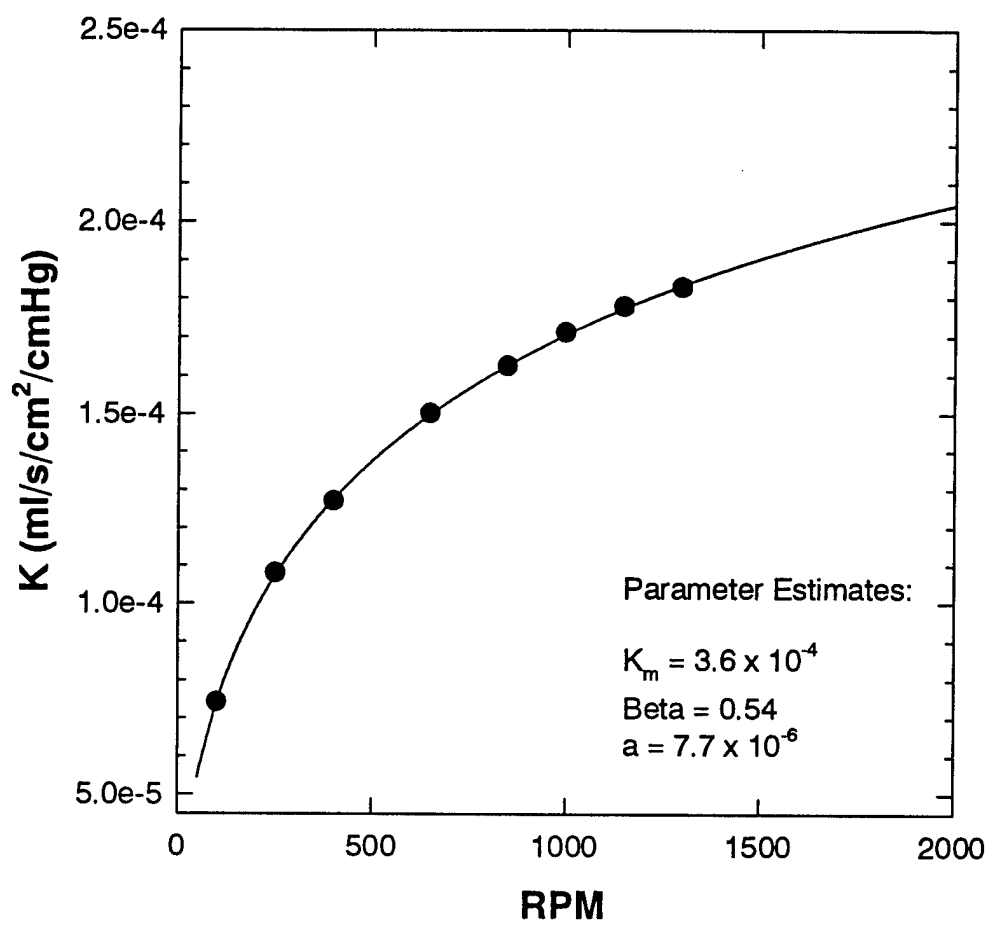


Figure 3.4 Sample data set used to estimate the carbon dioxide permeability of the TRC composite fiber in water at 37°C.

data used to determine the CO₂ permeability of the TRC fiber (see section 3.3). The line through the data points is the regression of Eq. 3.6 to the data points resulting in the fitted parameters K_m , a , and β summarized in the inset.

3.3 Permeabilities of Commercial Fibers

The properties of all fibers studied during the contract period are listed in Table 3.1 below, as well as the measured oxygen and carbon dioxide permeabilities, also shown graphically in Figure 3.5.

Table 3.1 Summary of fiber properties and permeabilities.

Fiber	Type	OD / ID (microns)	Pore Size / Porosity (microns) / %	Permeability (ml/s/cm ² /cmHg)	
				O ₂	CO ₂
KPF 190 ¹	Microporous	244 / 200	0.04 / 45%	2.9×10^{-5}	7.6×10^{-4}
KPF 280 ¹	Microporous	380 / 280	0.04 / 45%	1.4×10^{-5}	2.8×10^{-4}
PRF x30 ²	Microporous	300 / 240	0.02 / 40%	2.5×10^{-5}	6.4×10^{-4}
Oxyphan ³	Microporous	380 / 280	< 0.2 / 55%	7.2×10^{-5}	1.7×10^{-3}
MHF 200 ¹	Composite	262 / 209	N/A	7.9×10^{-6}	9.5×10^{-5}
TRC ⁴	Composite	245 / 200	N/A	3.9×10^{-5}	3.4×10^{-4}
Bend ⁵	Composite	381 / 280	N/A	4.8×10^{-5}	1.6×10^{-4}

¹ Mitsubishi Rayon Co., Tokyo, Japan

² Hoechst Celanese, Charlotte, NC

³ Akzo Nobel, Wuppertal, Germany

⁴ Surface Engineering Technologies, Salt Lake City, UT (coated KPF 190 fibers)

⁵ Bend Research, Bend, OR (coated Oxyphan fibers)

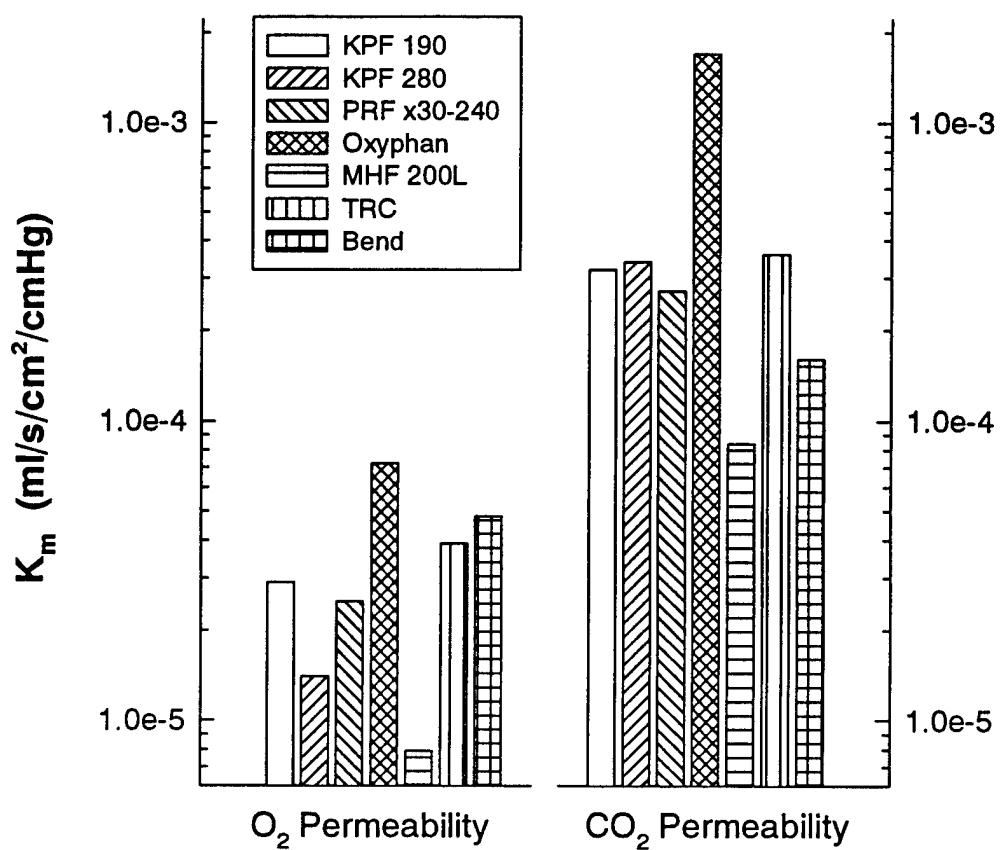


Figure 3.5 Summary of HFM oxygen and carbon dioxide permeability measurements.

The design constraint for O₂ gas exchange of IMO prototypes requires that the O₂ permeability of its fibers be greater than about $K_m \sim 1 \times 10^{-5}$ ml/cm²/s/cmHg (Figure 3.1). The oxygen permeabilities of all microporous fibers are great enough so as not to have a significant effect on IMO performance. In a gas-liquid environment, gas exchange across the wall of a microporous fiber occurs principally due to Knudsen diffusion through gas filled pores. Permeability is thus a function of pore size, wall thickness and porosity, as evidenced by the greater permeabilities of the Oxyphan fiber which has the largest pore size and porosity, and by the greater permeability of the KPF 190 fiber versus that of the KPF 280 due to a thinner wall. KPF porous fiber has suitable gas exchange permeability for IMO prototypes. Despite their high permeabilities, microporous fibers are subject to permeability degradation when exposed to blood due to liquid infiltration of the pores. Composite fibers, by nature of their nonporous layer, are resistant to wetting but have reduced permeability due to the greater resistance to diffusion of gas through this layer compared to diffusion through the gas filled pores. The MHF 200 fiber is constructed with a 1 micron nonporous polyurethane layer sandwiched between the porous walls. Although resistant to complete wetting (but perhaps not to partial wetting), its oxygen permeability of 7.9×10^{-6} ml/s/cm²/cmHg indicate that it would not be a suitable fiber candidate for the IMO.

The TRC (thrombo-resistant coating) fiber, is a KPF 190 microporous fiber coated on the exterior with an ultrathin solid membrane layer of siloxane less than one micron in thickness. Surprisingly, the O₂ permeability of the TRC composite fiber was measured to be 3.9×10^{-5} ml/s/cm²/cmHg. Even with a solid membrane coating, its O₂ permeability is greater than that of the KPF 190 microporous fiber from which the TRC fiber is fabricated. This result is exciting because it means that a fiber exists which not only possesses a great enough permeability for the design specifications of the IMO, but which is also resistant to wetting and will thus maintain its permeability for longer periods of time.

Although it seems counterintuitive that a composite fiber could have a greater permeability than the microporous fiber from which it is constructed, for a very thin true membrane layer and for a fiber in a gas-liquid environment, this result is most definitely

possible. In a gas-liquid system, the walls of a microporous HFM constructed with a hydrophobic material will in theory be gas filled, provided that the pressure difference across the gas-liquid interface at the mouth of the pores is not great enough to overcome the hydrophobic capillary forces which tend to repel liquid out of the pores (this pressure is estimated to be approximately 900 cmHg for the average pore size specifications of the KPF 190 and 280E fibers). However, assuming the permeability of a microporous fiber to be based entirely on Knudsen diffusion through 100% gas filled pores, the permeability to carbon dioxide of the KPF 190 HFM is expected to be approximately 1×10^{-2} ml/s/cm²/cmHg which is more than ten times greater than the measured carbon dioxide permeability of this fiber in water. This difference is consistent with the resistance of a water layer having a thickness of only 1% of the fiber wall thickness, i.e. 0.25 microns for the KPF 190. This suggests that at the interface of the liquid with the outer surface of the microporous fibers, there exists thin "pockets" of liquid which are unaffected, or undisturbed, by mixing of the liquid phase. These pockets might possibly be due to surface irregularities or a convex liquid-gas interface meniscus protruding into the pores. Nevertheless, their effect on the ability of that fiber to transfer oxygen or carbon dioxide in a gas-liquid environment is in essence a property of that fiber and must therefore be reflected by the membrane permeability. This underscores the importance of measuring HFM permeability in a gas-liquid environment for selection of an optimal fiber to be used to design an intravenous gas exchange device.

To validate the HFM permeability estimates measured with the diffusion chamber, TRC composite fiber permeability measurements were compared with measurements made in a gas-gas system. In a gas-gas system, the solid exterior layer of the TRC fiber prevents convectively induced gas flux through the fiber wall. Accordingly, measurements made in a gas-liquid versus gas-gas system should be similar. The CO₂ permeability of this fiber measured in the gas-gas system was found to be 3.1×10^{-4} ml/s/cm²/cmHg, and the estimate obtained using the diffusion chamber was 3.4×10^{-4} ml/s/cm²/cmHg. The permeability of the fiber measured with the diffusion chamber differs by only 10% with respect to that measured using the gas-gas system procedure. The slight difference is

within the error of both measurement procedures and therefore cannot be considered physically significant at this time.

3.4 Development of Fiber Coatings

The results of diffusion chamber testing suggest that an optimal fiber for the IMO is a microporous membrane with a true membrane coating on the outer surface of the fiber. To explore the possibility of obtaining a customized coated fiber, a collaborative effort was initiated with Bend Research Inc. of Bend, Oregon. This collaboration was funded by an SBIR Phase I grant from the National Institutes of Health. The results are germane to the work done under this contract, and hence are reported here for completeness. The ultimate goal of this collaboration is to develop a hollow fiber membrane specifically suited for the IMO device. To achieve this goal requires a fiber which is durable, has high permeability to oxygen and carbon dioxide, is resistant to wetting (i.e. permeability degradation caused by liquid penetration into the porous walls of the fiber), and which is resistant to thrombus formation at the blood-fiber interface. In the first phase of development of this fiber, the coating process was identified and refined to achieve a consistently uniform and defect-free non-porous layer over the exterior surface of a microporous hollow fiber membrane. Using this process, the preliminary fiber sample consisted of a commercially available polypropylene microporous fiber (Oxyphan, Table 3.1) coated with a non-porous layer of PDMS (poly dimethyl siloxane).

Evaluation of the preliminary sample of coated fibers consisted of measuring their permeabilities to oxygen and carbon dioxide in a gas-liquid environment, and assessing their wettability. The oxygen and carbon dioxide permeabilities of the coated samples were measured to be 4.8×10^{-5} and 1.6×10^{-4} ml/s/cm²/cmHg, respectively (Table 3.1, Figure 3.5). In comparison, the oxygen and carbon dioxide permeabilities of the uncoated Oxyphan fibers were measured to be 7.2×10^{-5} and 1.7×10^{-4} ml/s/cm²/cmHg. The permeabilities of the coated fibers, although slightly less than those of the uncoated microporous fibers, are great enough so as not to significantly effect the overall gas exchange permeability of an intravenous membrane oxygenation device such as the IMO (Figure 3.1).

A wetting model was developed and used to confirm the resistance to wetting of the coated fibers as opposed to microporous fibers which clinically have been found to wet out after exposure to human blood over a period of 8-12 hours. Because of the difficulty in actually testing the fibers with blood, a model was developed whereby the fibers were submerged in the diffusion chamber and exposed to a surfactant solution of sodium dodecyl sulfate (SDS). SDS is an amphipathic molecule made up of a polar, or hydrophilic, head group and two non-polar, or hydrophobic, hydrocarbon chains. When exposed to a hydrophobic material such as polypropylene in water solution, the hydrophobic tails of the SDS molecules coat the surface of the hydrophobic material so as to minimize the free energy of the system, rendering the surface hydrophilic. Both coated and uncoated fibers were exposed to the same concentrations of the SDS solution for a period of approximately eight hours, and the system permeability was measured at consistent conditions (Figure 3.6). The uncoated microporous fiber demonstrated slow degradation in permeability until the surfactant was actually visible in the gas flow exiting the fibers, whereas the coated fiber showed no change in permeability over the same period of exposure.

Future efforts towards fiber development will be focused primarily on the attachment of heparin molecules to the PDMS fiber coating to reduce thrombus formation by the fibers in blood. In addition, the diffusion chamber is currently being used to explore the actual mechanisms responsible for the clinical wetting of microporous fibers. We are focusing this research on the role of certain blood proteins and phospholipids as possible surfactants which act to make the walls of the pores hydrophilic, thus causing them to fill with fluid.

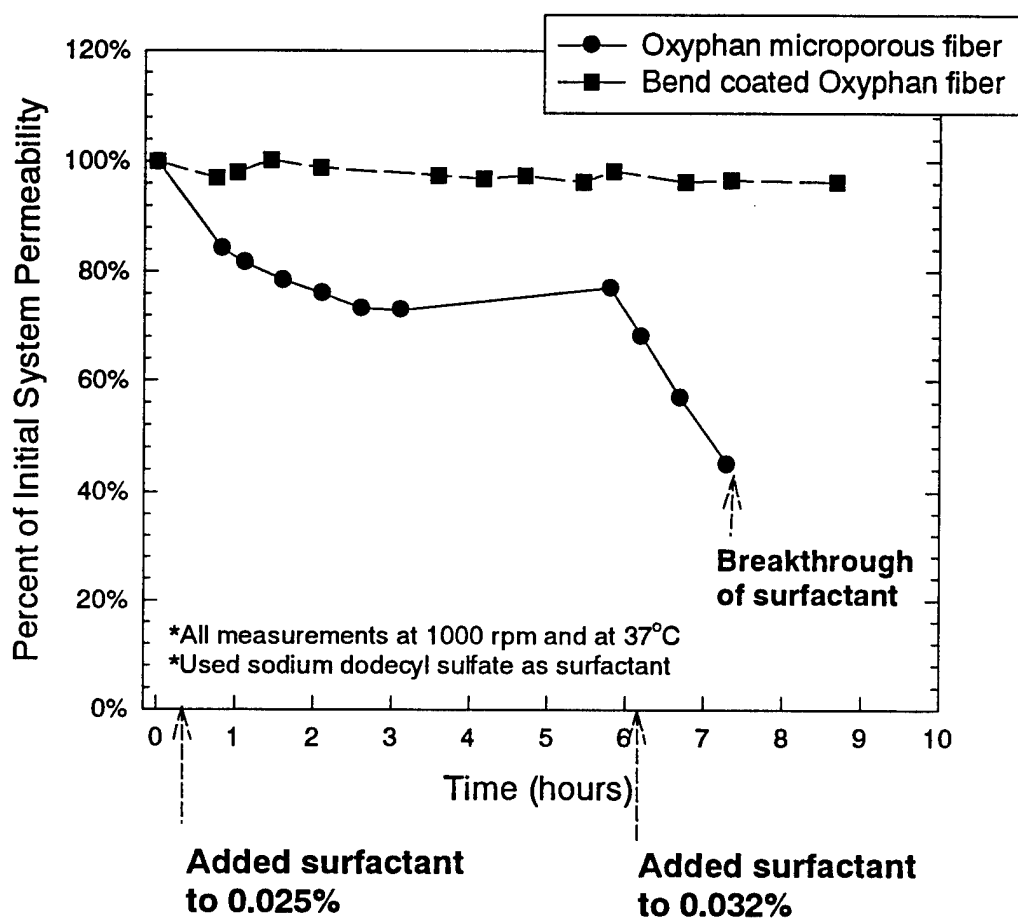


Figure 3.6 *In-vitro* fiber wetting test of coated versus uncoated Oxyphan fibers using a surfactant solution of sodium dodecyl sulfate.

4. IMO D PROTOTYPE DEVELOPMENT

4.1 Summary of Prototypes Developed

As described in section 1.3, IMO fabrication during this contract focused on the implantable sized prototype referred to as IMO D. Thirty-five IMO D series prototypes have been fabricated and tested during the entire contract period. Not all devices were identical and different D series devices signify design changes made to continually improve overall device performance. This section summarizes principle design changes during the evolution of the IMO over the contract period. Table 4.1 lists the pertinent information for each device. One major design change involved the helium pathway for balloon pulsation. The nature and rationale for these design changes are described further in section 4.2. Analysis and evaluation of the sweep gas pathway are elucidated in section 4.3. The *in-vitro* (bench test) gas exchange performance of the IMO prototypes during the design evolution are detailed in chapter 5. Chapter 6 follows with a description of the *in-vivo* testing of the D series IMO prototypes.

The first implantable sized IMO D prototypes (D01-D02) incorporated the MHF 200 composite hollow fiber membrane (see section 3.3) in their fiber bundles. The gas exchange performance of these devices significantly decreased due to the reduced permeability of the MHF 200 fiber (see Figure 3.5), and by the compromised balloon pulsation dynamics due to the mentioned problems in the helium pathway. Prototypes D04 and above used noncomposite hollow fiber membranes and the D04-D07 series had some improvement in balloon pulsation due to particular changes in the helium pathway configuration. The ten devices which comprise the D07 series were fabricated for an extensive series of *in-vivo* tests, accompanied by thorough bench testing beforehand. These devices used the Medtronic PRF microporous fibers which are resistant to plasma infiltration during extended blood contact. The last four D07 devices were Carmeda coated (covalently bound heparin) to help prevent blood coagulation on the fibers *in-vivo*.

Table 4.1 Prototype Summary

Prototype	Date Received	Fiber Type	Number of Fibers	Surface Area (m ²)
D01	2/15/95	MHF 200-L	960	.2691
D02	2/22/95	MHF 200-L	960	.2691
D03	4/17/95	MHF 200-L	960	.2691
D04	6/6/95	KPF-190-M	1008	0.15517
D05	8/7/95	MHF-200-L	966	0.27075
D06	9/6/95	KPF-190-M	1100	0.1702
D07.1	10/13/95	PRF-240	708	0.1334
D07.2	11/2/95	PRF-240	720	0.1356
D07.3	10/30/95	PRF-240	696	0.1311
D07.4	11/7/95	PRF-240	732	0.1379
D07.5	11/16/95	PRF-240	720	0.1356
D07.6	11/16/95	PRF-240	720	0.1356
D07.7	11/16/95	PRF-240	720	0.1356
D07.8	11/16/95	PRF-240	720	0.1356
D07.9	11/16/95	PRF-240	720	0.1356
D07.10	11/28/95	PRF-240	720	0.1356
D08.1	12/19/95	PRF-240	720	0.1356
D08.2	12/20/95	PRF-240	720	0.1356
D09.1	2/7/96	TRC-4.0	1008	0.1583
D09.2	2/7/96	TRC-4.0	1010	0.1586
D09.3	2/15/96	TRC-4.0	1008	0.1583
D09.4	2/15/96	TRC-4.0	1008	0.1583
D10	4/16/96	KPF-190-M	1008	0.1551
D11	4/16/96	KPF-190-M	1008	0.1551
D12	4/14/96	KPF-190-M	1020	0.1570
D13	4/14/96	PRF-240	720	0.1357
D14.1	6/11/96	KPF-280-E mat	385	0.0850
D14.2	10/26/96	KPF-280-E mat	385	0.0850
D15.1	7/18/96	KPF-280-E mat	580	0.1859
D15.2	8/14/96	KPF-280-E mat	580	0.1895
D15.3	9/5/96	KPF-280-E mat	580	0.1895
D16	10/28/96	KPF-280-E mat	385	0.0850
D17.1	12/19/96	Celgard 240 mat	665	0.1284
D17.2	2/28/97	Celgard 240 mat	665	0.1284
D17.3	2/28/97	Celgard 240 mat	665	0.1284

More extensive modifications to the helium pathway were made to improve balloon pulsation dynamics of the IMO. Prototypes D08 and above all incorporated these improvements to the helium pathway (further described in section 4.2). The D09 series used a composite hollow fiber membrane, the TRC fiber (a microporous fiber with a true outer membrane), which had an appreciably greater gas permeability than the previous MHF 200 composite fiber (refer to Figure 3.5).

A series of design modifications were done to explore the effects of fiber distribution, both within the cross-section of the vessel and around the central balloon. Prototypes D06 and D12 were fabricated with kinked (crimped) fiber bundles. The use of crimped fibers, as used in the clinically tested IVOX device, helps improve fiber distribution within the vessel cross-section. Several devices were explored which involved potential improvements to fiber distribution around the central balloon. The D13 device used braided fibers as a means to keep the fibers better constrained and well distributed around the central balloon. The D10 device used plastic mesh both inside and outside of the fiber bundle as another way to constrain the fibers within the bundle.

The best means found for constraining the fibers around the central balloon and for maintaining uniformity of fiber spacing involved using fiber fabrics or mats in place of free fibers within the fiber bundle. The D14 device used the KPF 280 fiber mat which incorporated fibers with a relatively large outer diameter of 380 microns. Although the use of fiber mats appeared attractive, the diameter of the KPF 280 fibers limited the number of fibers allowable within the fiber bundle due to size constraints and therefore decreased fiber surface area unacceptably. The only other available fiber mat with smaller fibers is the Hoechst Celanese Celgard 240 hollow fiber array, which uses fibers with a 300 micron outer diameter. Three D17 devices with the Celgard 240 fiber array were fabricated and tested in various *in-vitro* experiments, as well as an *ex-vivo* animal experiment. Currently, the D17 devices are our most successful prototypes, demonstrating the greatest gas exchange levels per unit fiber. The use of fibers in fabrics or mats will be the fiber configuration chosen for the new IMO G series currently under fabrication (section 7.2). This new series also incorporates redesigned gas pathways, a central balloon twice the

current size, and double the fiber surface area of previous prototypes. These changes anticipate the near future scale up of the IMO for eventual human clinical use.

4.2 Analysis of Balloon Pulsation

Balloon pulsation is intended to enhance IMO gas exchange efficiency by providing active mixing and thereby reducing the boundary layer limitation of gas transfer. In many of the older IMO prototypes, however, balloon pulsation had little or no effect on oxygen exchange rates. For instance, the maximum oxygen transfer rate in the D03 device was achieved without any balloon pulsation, with the balloon in a static inflated state. Extensive experimental and theoretical analysis has since led to several changes in both the internal IMO geometry and drive system operation which have significantly improved gas exchange performance in the implantable-sized, D series IMO prototypes.

Experimental Characterization of IMO Balloon Pulsation Dynamics Early gas exchange experiments showed that balloon motion had little impact on oxygen transfer rates, which we suspected was due to incomplete inflation/deflation of the balloon at higher frequencies. Testing this required devising a method for examining the inflation-deflation amplitude as a function of balloon pulsation frequency. As described below, we developed a plethysmograph to characterize balloon dynamics over a broad range of operating frequencies.

Figure 4.1 shows the balloon plethysmograph which was designed and built to analyze balloon pulsation dynamics. The device consists of a thin-walled acrylic chamber with four pressure taps located at various positions and a small hole in the top which allows for the addition and removal of water. The hole also contains an O-ring groove and an O-ring, which provide an air-tight junction between the chamber and a split seal. After the chamber is partially filled with water, the split seal is tightly clamped around the pneumatic delivery catheter of the device and secured in the O-ring junction, such that the prototype is submerged. Inflation and deflation of the balloon cyclically compresses and expands the volume of trapped air within the chamber, thereby creating periodic pressure swings. These pressure changes are measured through a fluid-filled catheter connected to one of the pressure taps, and the pressure wave amplitude is adjusted by adding or

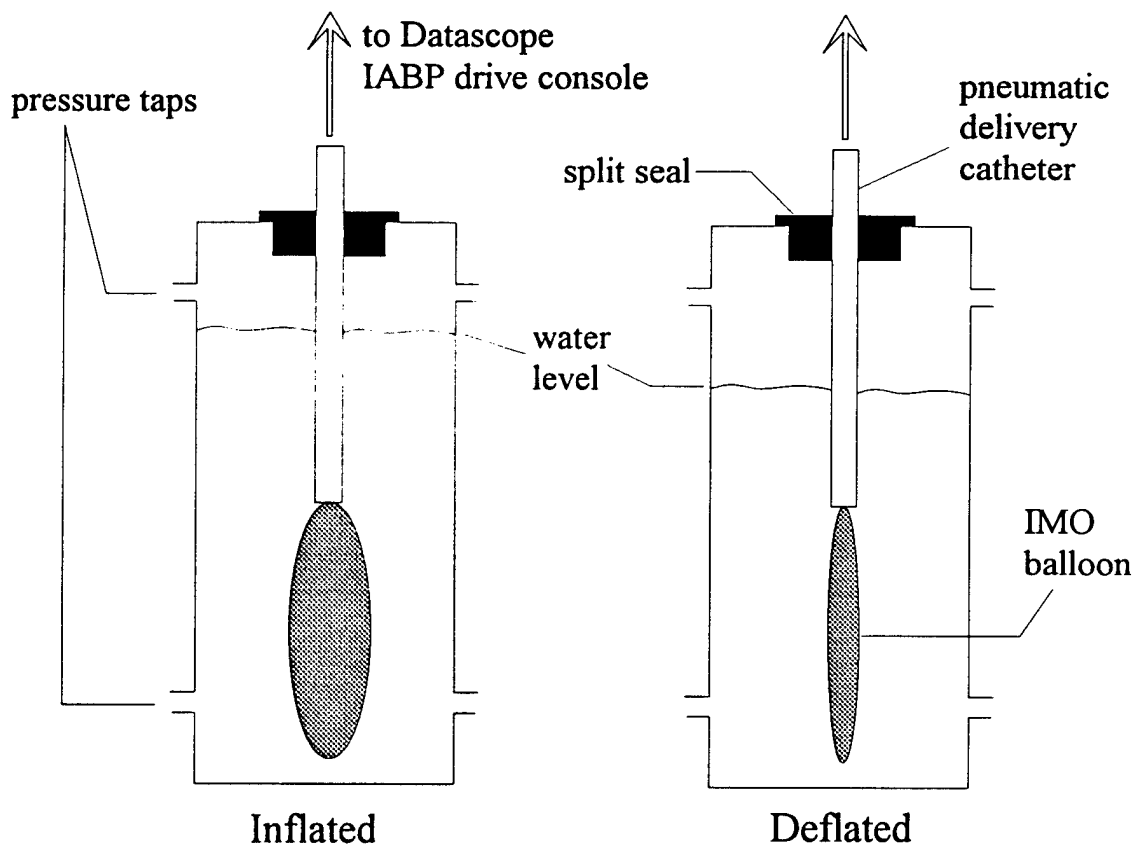


Figure 4.1 Schematic of the balloon plethysmograph which is used to characterize balloon dynamics over a broad range of operating frequencies.

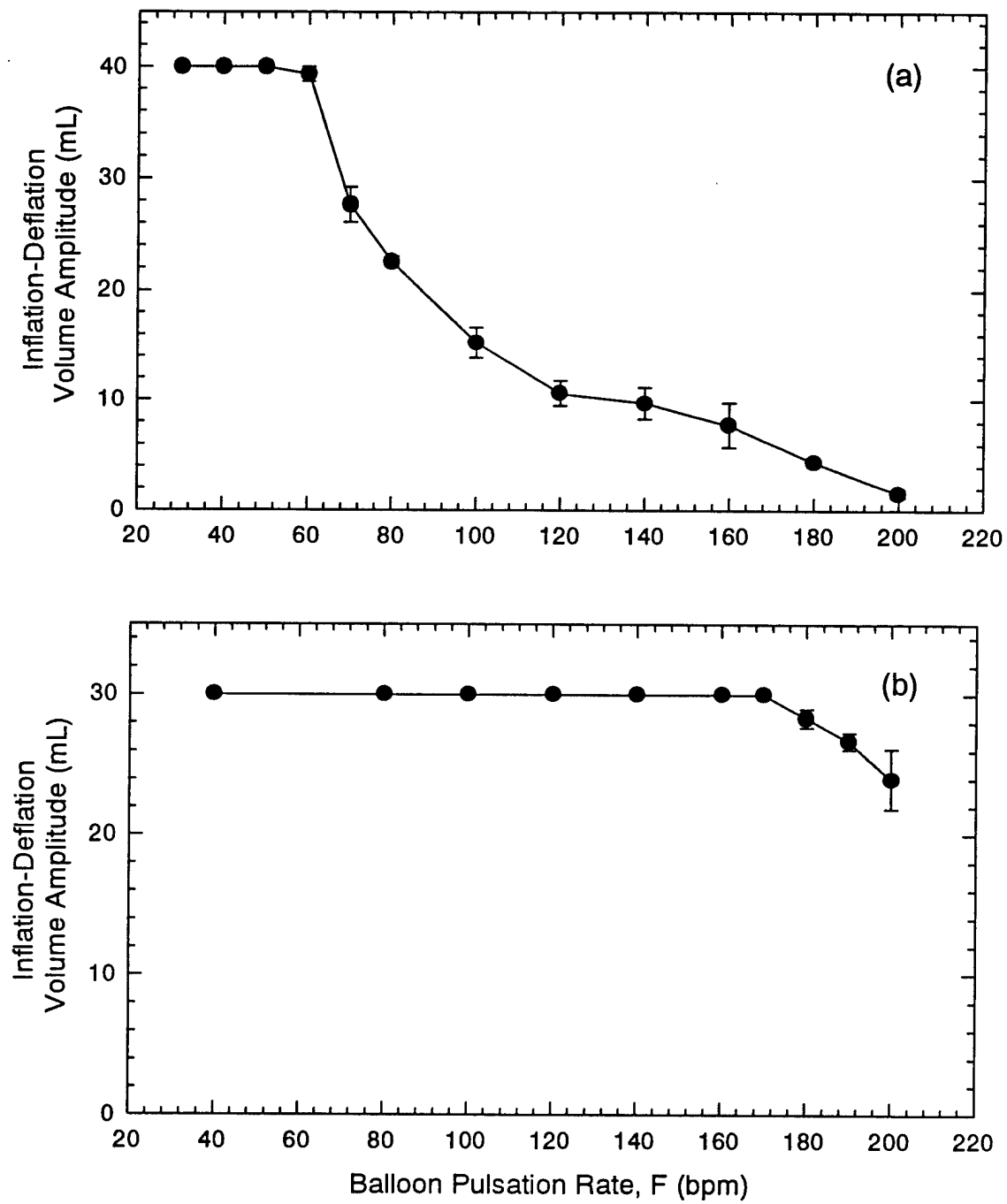


Figure 4.2 (a) Frequency spectrum for the D03 device (unmodified) and (b) D08 prototype (modified.)

removing water until the peak pressure is about 30 mmHg (to minimize the back-pressure which counteracts balloon inflation). Use of a fluid-filled catheter prevents distortions in measured pressure due to gas compressibility. The pressure waveform is then converted to a volume waveform (e.g., $V_b(t)$) using the Ideal Gas Law.

The frequency spectrum consists of the inflation-deflation volume amplitude plotted as a function of pulsation frequency. The frequency spectrum for the D03 device, one of the earlier implantable-sized IMO prototypes made prior to design changes in pneumatic pathways, is shown in Figure 4.2 (a). While the balloon fills and empties completely at low frequencies, the inflation-deflation amplitude decreases rapidly beyond 60 bpm. The maximum frequency at which the balloon can inflate and deflate completely (60 bpm for the D03 device) is the "critical frequency." Beyond the critical frequency, balloon pulsation gradually diminishes and can no longer enhance the gas exchange rate. Thus, testing of the D01-D03 IMO prototypes indicated no balloon enhancement of gas exchange beyond 60 bpm.

Helium Pathway Modification The comparatively low critical frequency of the D03 device (60 bpm) prompted us to carefully examine the design of the helium pathway. Table 4.2 shows the dimensions of the helium pathway for the D03 device. The pathway consists of three different sections in series; an entrance tube, a long annular pathway and a short annular pathway. The annular pathways consist of the spaces between the oxygen inlet tube and the outside wall of the pneumatic delivery shaft. Since the caliber of the short annular pathway is very small, its resistance to helium flow is very large potentially limiting helium flow through this section. The flow resistance of this segment could be reduced by either increasing the outside diameter of the pneumatic delivery shaft or decreasing the size of the oxygen inlet tube. The overall size of the pneumatic delivery catheter is limited by physiological considerations (it must be small enough to fit into the femoral vein without impeding venous blood flow), so increasing the size of the helium pathway can only be achieved by decreasing the size of the oxygen inlet tube and potentially increasing the resistance to oxygen delivery. A trade-off exists therefore between improved balloon pulsation performance and increased resistance to oxygen

delivery, necessitating the consideration of both factors in redesigning the pathway dimensions.

Table 4.2: Dimensions of Unmodified D03 Helium Pathway			
pathway	outer diameter (in)	inner diameter (in)	length (in)
IMO entrance tube		0.076	2.5
long annular path	0.148	0.128	7.0
short annular path	0.136	0.128	1.4

Figure 4.3 illustrates the trade-off between critical frequency and oxygen flow rate (for a given pressure drop in the sweep gas pathway) as the outer diameter of the oxygen inlet tube is varied. The critical frequency (f_{crit}) of the helium pathway was determined with the steady, compressible Poiseuille flow model, while turbulent flow theory was applied to the oxygen delivery pathway. Figure 4.3 indicates that the critical frequency can be increased markedly with only a slight decrease in oxygen delivery tube size, and thus with only a minor decrease in oxygen flow rate. For instance, reducing the oxygen inlet tube diameter from 0.124 inches to 0.112 inches increases the critical frequency from 50 to 200 bpm, but leads to a less than 1% decrease in oxygen flow rate at a constant pressure driving force.

The pneumatic analysis indicated in Figure 4.3 led to modifications in the helium pathway such that the oxygen inlet tube was made smaller and the helium pathway became substantially larger. The dimensions of the modified (D08-series) helium pathway are shown in Table 4.3. These changes resulted in a substantial improvement in the balloon pulsation capability of the D08 device, as illustrated in Figure 4.2(b). While the critical frequency of the D03 device was only about 60 bpm, the D08 prototype can pulsate effectively as high as 160-170 bpm.

Table 4.3: Dimensions of Modified D08 Helium Pathway			
pathway	outer diameter (in)	inner diameter (in)	length (in)
IMO entrance tube		0.076	2.5
annular path	0.115	0.073	

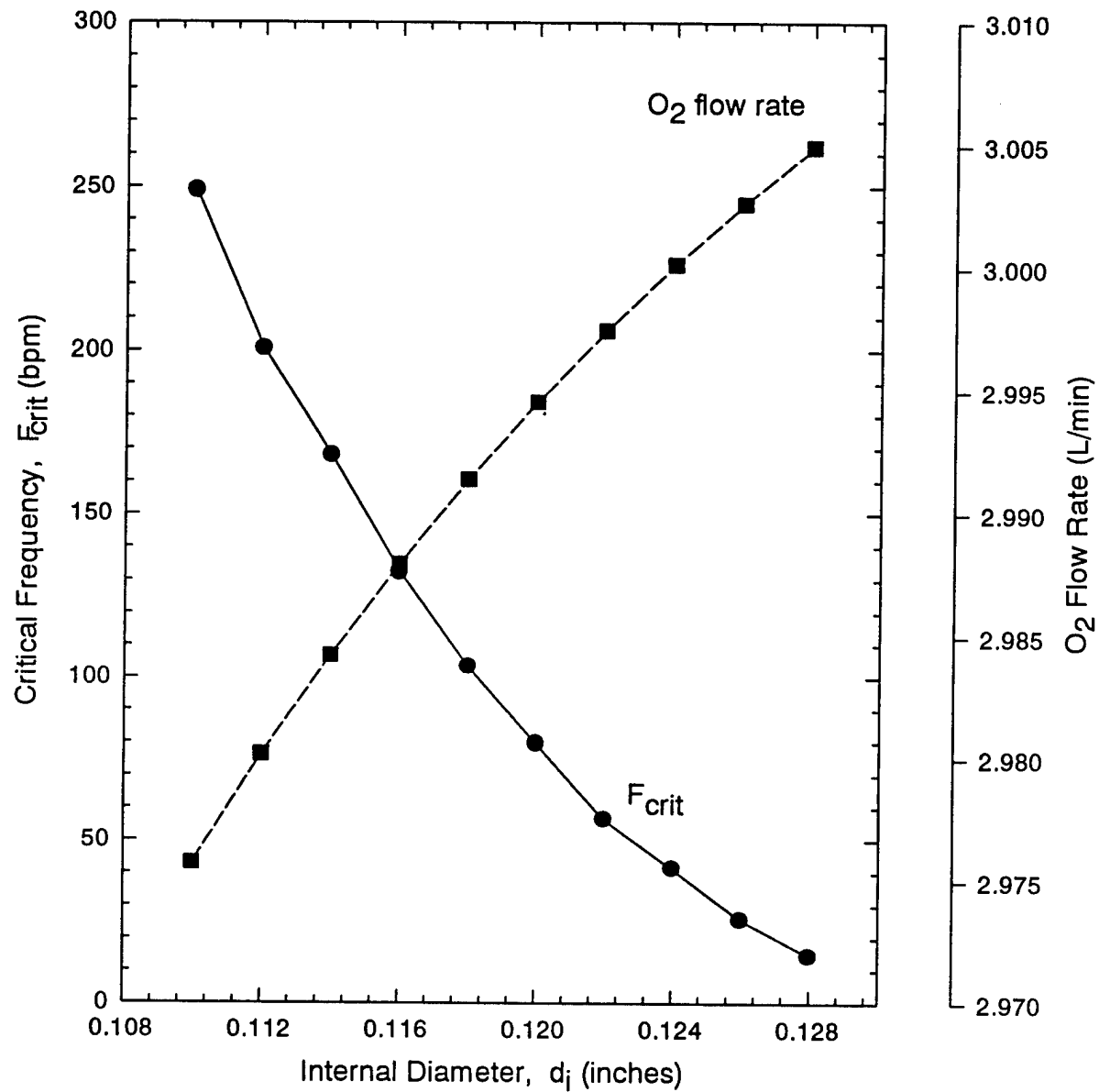


Figure 4.3 Trade-off between critical frequency and oxygen flow rate for various oxygen inlet tube diameters.

Effective Drive System Operation While the changes made to the helium pathway substantially improved the balloon pulsation performance of the D08-series and later prototypes, the balloon pulsation will eventually fail at very high frequencies even in the modified devices. Failure of balloon pulsation means that the balloon no longer fills or empties completely. Beyond the critical frequency, balloon pulsation may fail in either a deflated or inflated state. An inflation-deflation amplitude of 50%, for instance, could indicate that the balloon is completely empty at end-deflation but only half full at end-inflation, or conversely, that the balloon is full at end-inflation but is still half full at end-deflation (or anything between these extremes). For gas exchange, the balloon pulsation should fail in the inflated state, since an inflated balloon detracts from the cross-sectional area available for flow and therefore increases the longitudinal fluid velocity (thereby diminishing boundary layer effects and enhancing gas exchange). The following section describes how the inflation-deflation timing controls on the drive system can be optimally set to ensure that, beyond the critical frequency, balloon pulsation fails in the inflated state.

The Datascope Intra-Aortic Balloon Pump (IABP) drive console has two controls which vary the inflation-deflation timing ratio. These are the "IAB inflation" and "IAB deflation" knobs, which provide for earlier/later inflation and earlier/later deflation, respectively. Each knob can be set at a value between -4 and +4, where -4 is for earlier inflation/deflation and +4 is for later inflation/deflation. If the inflation knob is set at -4, the balloon inflates immediately after end-deflation, whereas a setting of +4 introduces a delay between end-deflation and the start of the next inflation period. These knobs can therefore be adjusted to produce a wide variety of inflation-deflation waveform patterns which may affect gas exchange rates.

Figure 4.4 shows the maximum volume of the balloon (at end-inflation) as a function of frequency for a variety of inflation-deflation timing settings. The timing parameter, T , is defined as the difference between the deflation and inflation knob settings, such that $T=8$ corresponds to latest deflation (+4) with earliest inflation (-4). This

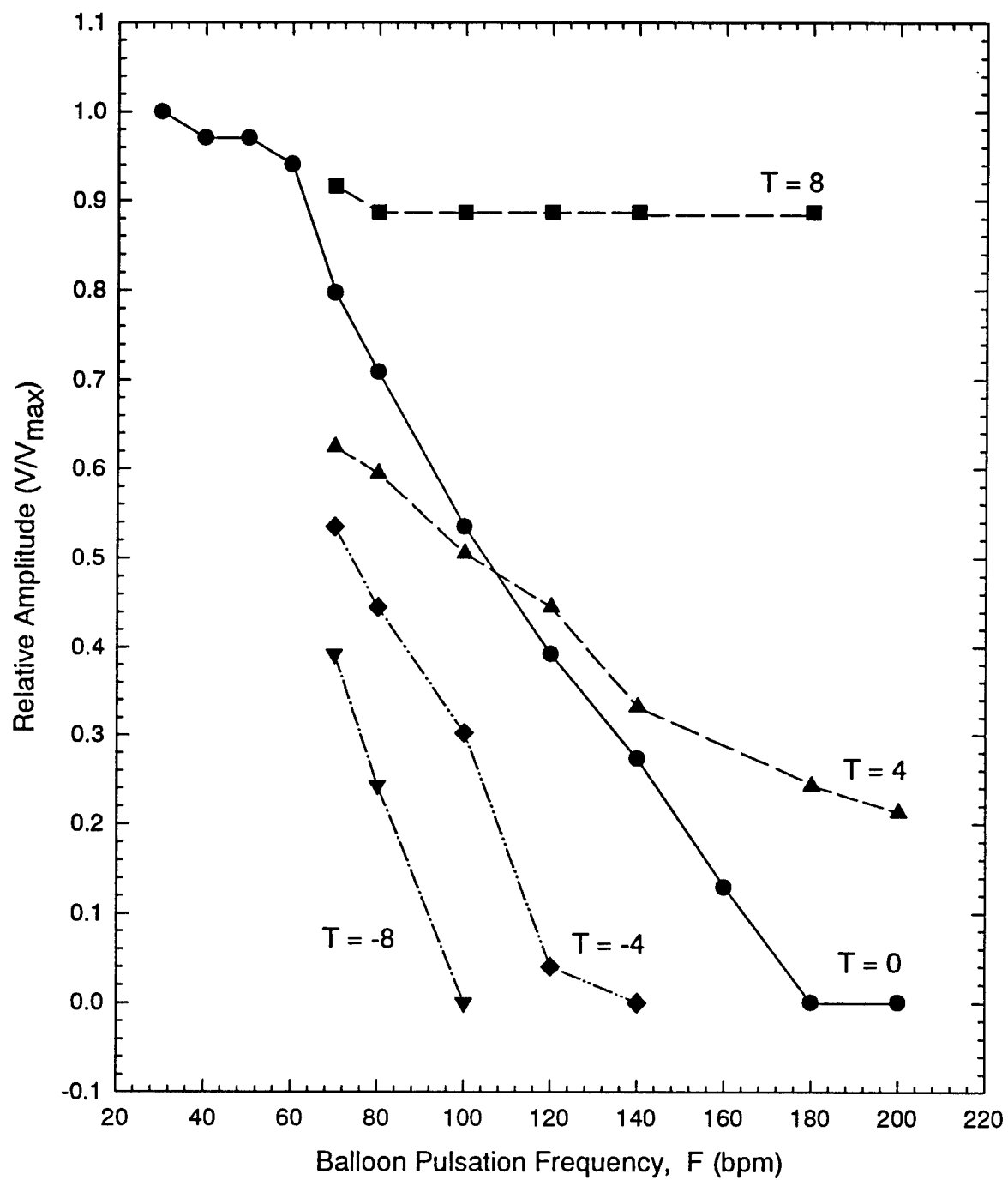


Figure 4.4 Impact of the timing parameters on state of balloon failure.

prototype has a critical frequency of about 80 bpm, which is relatively independent of the timing parameter. Beyond the critical frequency, however, the timing controls have a significant impact on the state of balloon failure. For $T=8$, the balloon remains completely full at end-inflation even beyond the critical frequency, despite incomplete emptying. When $T=-8$, however, the balloon quickly tends towards the deflated state. As described above, complete filling of the balloon is desirable for gas transfer so that pulsation fails with the balloon inflated. Accordingly, the timing parameters on the IABP console are now optimally set to yield earlier inflation/late deflation ($T=6-8$) beyond the critical frequency. This ensures a relatively gradual decrease in gas transfer during IMO operation beyond the critical frequency.

Implications of Device Scale-Up The changes made to the helium pathway have significantly improved the balloon pulsation characteristics of the D08 series and later prototypes. Our current devices, however, are scaled-down versions of the ultimate implantable-sized IMO D series device. For instance, D08 is 20 cm long with a 30 mL balloon and 0.13 m^2 of fiber surface area. The final IMO devices for clinical use must have about $0.4-0.5 \text{ m}^2$ of surface area to provide the targeted levels of gas exchange. Scale-up therefore requires increasing both the fiber length and fiber packing density of the IMO. The maximum allowable length of a device is about 40 cm given the constraints imposed by intravenous placement. Thus the ultimate IMO clinical device will be about twice as long as the D08 device and will have a balloon size of about 60-70 mL, concordant with the length of the fiber bundle.

The current helium pathway allows for relatively high critical frequencies (160-180bpm) in scaled-down IMO prototypes. It will not suffice for scaled-up 40 cm IMO devices. For example, the critical frequency of D08 with a 30 mL balloon is about 170 bpm. If the D08 balloon were 60 mL, twice as much flow would be required and the period of balloon inflation would therefore be twice as long. This means that the critical frequency of the D08 device with a 60 mL balloon would be about 85 bpm for the same helium pathway. Clearly, to obtain the desired balloon pulsation rates of 160-180 bpm in a scaled-up 40 cm device, it will be necessary to redesign the helium pathway. These pneumatic considerations of IMO device scale-up are described further in Chapter 7.

4.3 Analyses of Sweep Gas Pathway

The flow dynamics of the sweep gas pathway within the IMO device directly influence the gas exchange rates for both oxygen and carbon dioxide. The principle driving force for gas exchange is the difference between the partial pressure of oxygen or carbon dioxide in the sweep gas and that in the blood phase. If carbon dioxide is allowed to accumulate in the fiber bundle, the driving gradient for carbon dioxide exchange will be diminished. Therefore, the sweep gas must flow quickly enough to minimize the build-up of carbon dioxide. Any increase in the sweep gas flow rate, however, decreases the pressure of the sweep gas in the fiber bundle. Since the partial pressure of an element in a gas mixture is directly proportional to the total pressure of the mixture, the partial pressure of oxygen in the sweep gas decreases with increasing sweep gas flow rate. Effective transfer of both O_2 and CO_2 therefore requires a pathway with minimal pneumatic (gas flow) resistance. As part of development efforts towards improving gas exchange performance, we studied the pressure drop-flow rate relationship in the sweep gas pathway of the current implantable-sized D series IMO.

Measurement of Pressure Drop - Flowrate Relationship The pneumatic resistance in various regions of the sweep gas pathway was measured experimentally for seven IMO D series devices. Four devices were from the D07 series used in acute *in-vivo* testing and contained 720 fibers of .025 cm inner diameter and 20 cm length. Two devices were from the D08 series, and featured the modified helium pathway. Modifications to the helium pathway did necessitate reductions in size of part of the sweep gas pathway. Though these devices had identical fiber bundles to those of the D07 series, their oxygen inlet tubes had reduced diameter to accommodate the helium pathway. One device was also used from the D02 series, which contained 960 fibers of 0.02 cm. inner diameter and 37 cm length. This device was fitted with additional pressure taps at the inlet and outlet manifolds to provide greater resolution of the pressure distribution within the IMO.

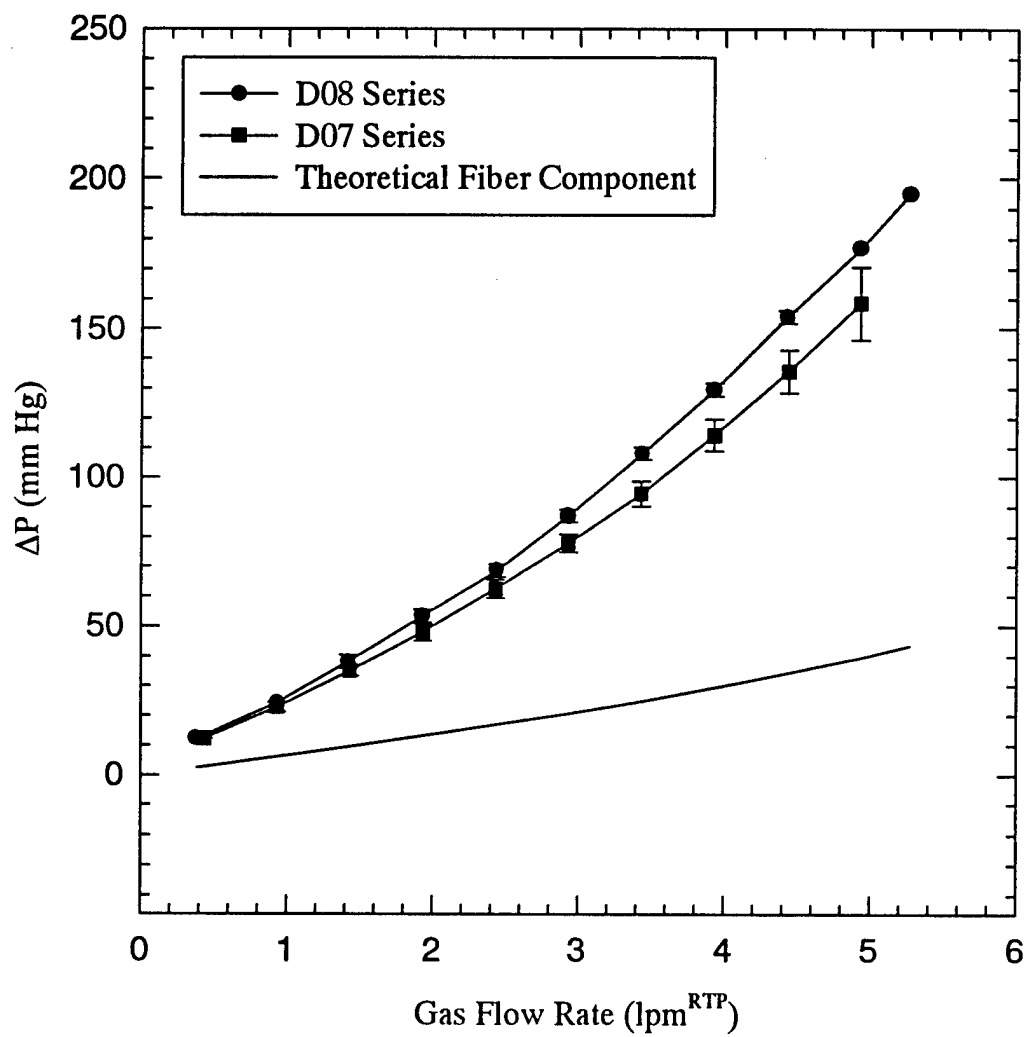


Figure 4.5 Pressure drop - flow rate relationship in IMO series D prototypes (D07 and D08).

The total pressure drop required to drive vacuum flow through the IMO D07 and D08 series devices in the range from 0 to 5 L/min. is shown in Figure 4.5. Gas flow rates from 3 to 6 L/min. are required for maximal CO₂ exchange, and the D07 and D08 series devices would require no more than 200 mm Hg to operate at these flow rates. Even if the entire reduction in pressure occurred before the fiber bundle, the PO₂ in the fibers would only be reduced by 25 percent.

Gas flow through the fiber bundle obeys compressible Poiseuille theory (Federspiel et al, 1996) and is given by: $P_o - P_l = 2RP_{atm}Q_{RTP}$ where P_o and P_l are the pressures at the upstream and downstream ends of the fiber bundle, $R = 128 \mu l / N\pi d^4$ and represents the Poiseuille resistance, Q is the gas flow rate at standard temperature and pressure, μ is the gas viscosity, l is equal to the length of the fiber bundle, d is the inner diameter of the fibers, and N represents the number of fibers in the bundle. Thus, the pressure drop due to the fiber bundle can be estimated and compared to the overall pressure drop shown in Figure 4.5. Most of the pressure drop in these devices occurs outside the fiber bundle. Thus, scaling up the membrane surface area of an IMO device by increasing the length of the fiber bundle may only have a small impact on the overall pressure drop through the device. Furthermore, it became imperative to examine more closely the elements of the sweep gas pathway to determine where principle flow resistances resided, and deduce whether modifications could help reduce them.

The distribution of pressure loss through the IMO was studied by incorporating additional pressure taps at the inlet and outlet manifolds of an older IMO device (D02 series), and the results are shown in Figure 4.6 a through c. Note that the total pressure drop through this device (approximately 400 mm Hg at 5 L/min.) is higher than that of the D07 and D08 series prototypes because the smaller diameter fibers of the D02 device increase the resistance of its fiber bundle three-fold over those of the D07 and D08 series devices. The distribution of the total pressure drop between pre-fiber, intra-fiber, and post-fiber components of the IMO device is shown in Figure 4.6 a, b, and c respectively. The pre-fiber component of the pressure drop (Figure 4.6a) is small and agrees well with predictions based on flow through the O₂ inlet tube, which suggests that the pressure drop in the inlet manifold is minimal. The fiber component of the total pressure drop (Figure

4.6b) accounts for nearly half of the flow resistance, due to the decreased diameter of the fibers and the increased length of the fiber bundle compared to the D07 and D08 series prototypes. The experimental results compare well with those predicted for compressible Poiseuille flow through the fiber bundle. The post-fiber component of the pressure loss (Figure 4.6c) also accounts for a large percentage of the total pressure drop. Although it has no effect on the mass transfer capabilities of the device, it may be desirable to redesign this part of the pathway to reduce the power needed to pump the sweep gas.

The driving gradient for oxygen exchange is directly proportional to the average pressure of the sweep gas in the fiber bundle. In a scaled-up IMO prototype (see Chapter 7), the lengths of the O₂ inlet tube and the fiber bundle will be increased, thus increasing the pre-fiber and intra-fiber components of the pressure drop. This increase can be easily quantified using the results of Figures 4.6 a and b, which indicate that the pre-fiber component and the intra-fiber component of the pressure drop can be accurately modeled using theoretical predictions. Therefore, the average pressure of the sweep gas in the fiber bundle can be predicted for a scaled-up IMO and the subsequent reduction in the driving gradient for oxygen exchange can be determined without actually building the prototype. If the pressure of the sweep gas is too low at the operating gas flowrate, the O₂ inlet pathway can be redesigned to lower its pneumatic resistance.

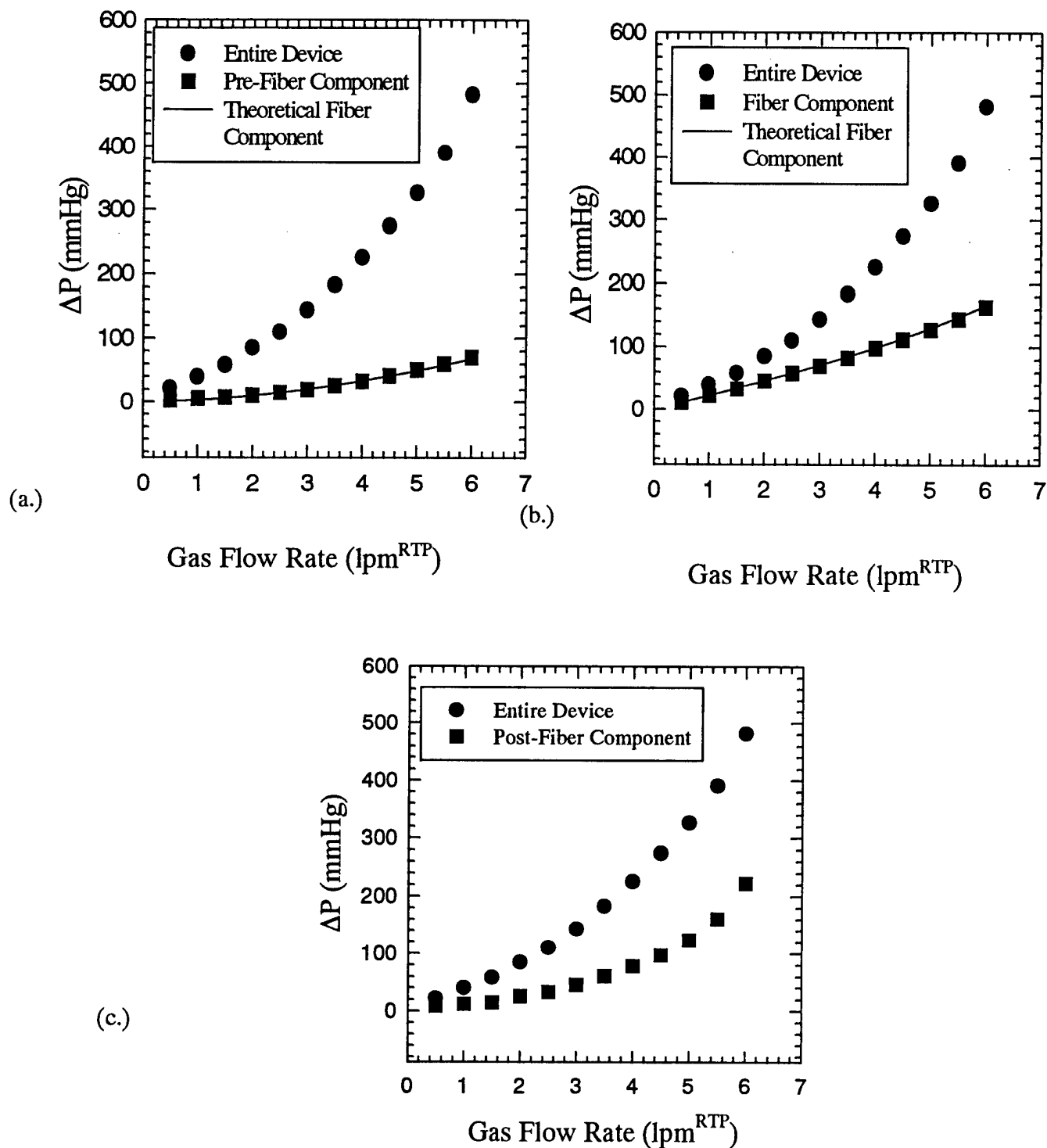


Figure 4.6 Distribution of the pressure drop in IMO D device (D02). a) Pre-fiber component, experimental and theoretical; b) Intra-fiber component, experimental and theoretical; c) Post-fiber component.

5. IN-VITRO GAS EXCHANGE PERFORMANCE

The IMO design evaluation and development process requires that extensive gas exchange performance studies be readily and repeatably made in a convenient *in-vitro* bench test system. The bench test system allows for determining the oxygen exchange rate of IMO prototypes (as an index of their gas exchange capacity) over a full range of their balloon pulsation rates. This section describes the development of the IMO design during the contract period from the perspective of gas exchange performance in these *in-vitro* bench tests. Complementary acute and chronic animal testing of select IMO prototypes during the development is described in the following chapter.

5.1 *In-Vitro* Characterization Testing

Apparatus and Procedure IMO prototypes are bench-tested in the perfusion loop shown in Figure 5.1 using distilled water as the test fluid medium. The apparatus and procedure for characterization testing of IMO prototypes was described in detail in our first annual report, and will only be summarized here for completeness. The loop consists principally of a mock “vena cava” test section (a 1 inch ID rigid plexiglass or flexible Silicone tube) within which the IMO device is placed, and a centrifugal pump for providing a steady dc flow rate of water through the system. The perfusion loop also contains an extracorporeal oxygenator module used as a deoxygenator and heat exchanger, compliance chambers for damping fluid pressure oscillations engendered by balloon pulsation, and liquid sampling ports for measuring the PO_2 in the water pre and post test section. A static in-line mixer is used downstream of the compliance chamber but before the downstream sampling port to assure total mixing of the fluid leaving the test section before the sampling site. Ancillary equipment to the perfusion loop includes gas and liquid-side flow meters, along with pressure taps distributed along the mock vena cava. The IMO device is placed within the test section, which is perfused from 1 to 6 L/min with distilled water at 37°C (standard flowrate condition during pulsation tests is 3 L/min unless otherwise stated). Pure O_2 sweep gas is run through the IMO device under vacuum at 3 L/min. Distilled water flowing through the tube is sampled before and after the IMO device and the difference in O_2 partial pressure created by the prototype is determined by injecting these samples in a Radiometer ABL

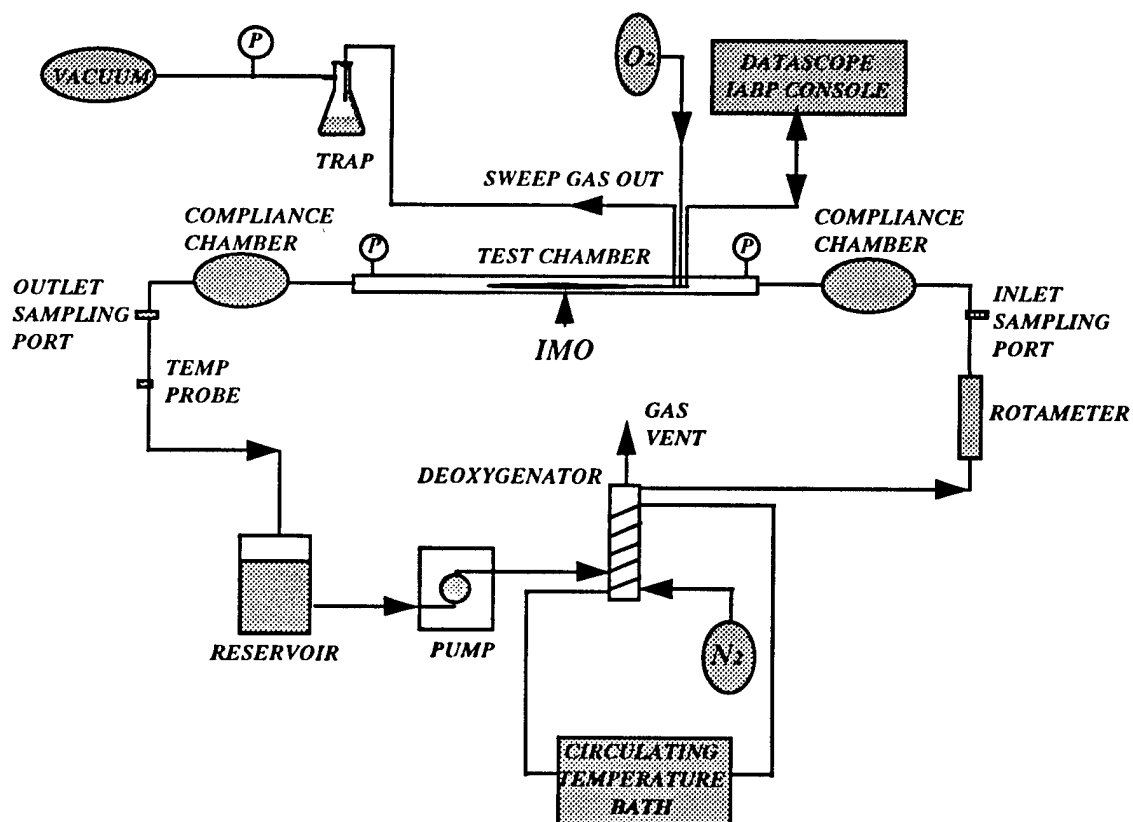


Figure 5.1 Schematic of IMO *in-vitro* characterization loop.

330 blood gas analyzer. The rate of O_2 exchange is computed from the product of the PO_2 difference in water across the test section, water flow rate, and the solubility of O_2 in the water. At a given water flow rate, the O_2 exchange rate (VO_2) is measured over a range of balloon pulsation rates up to about 180 bpm, depending on the pulsation ability of the IMO prototype.

Measurement Variability Our bench test characterization system enables us to fundamentally study the gas exchange enhancement resulting from balloon activation over a range of possible balloon pulsation frequencies. In anticipation of these fundamental studies, we undertook a close examination of our *in-vitro* test apparatus and protocol. We sought to understand the origin of any measurement variability in the characterization of IMO prototypes and to improve our testing protocol to properly account for this variability. This is important since the value of characterization testing ties directly to repeatability of measured gas exchange performance for a given prototype.

Figure 5.2 shows the results of a systematic examination of measurement variability associated with the characterization of prototypes within the model vena cava in terms of their O_2 exchange rate. Shown are coefficients of variation (CV) for measured O_2 exchange associated with multiple determinations of a particular measurement or condition. For example, for a given bulk flowrate in the test loop and balloon pulsation rate, the CV associated with repeated sampling is small, less than 3% (left most bar). Similarly, if either the flowrate or balloon pulsation rate is changed then reset to their original values, the resulting gas exchange CV's are also very small (BPM and Flow bars). In contrast, if the orientation of the IMO prototype within the model vena cava is changed by rotating the device within the test chamber, the gas exchange CV is appreciable, being about 15 to 20%, depending on pulsation conditions. This indicates that gas exchange has greatest sensitivity to the particular position or orientation of the prototype when placed within the model vena cava. The effect of orientation on gas exchange performance was determined using a free fiber prototype. The orientation effect appears less pronounced for the constrained fiber prototypes.

Thus, the same IMO prototype tested on two separate occasions may exhibit differences in respective gas exchange levels of 15 to 20% depending on particular prototype position from one test to another. Because of this, we changed our prototype characterization protocol to

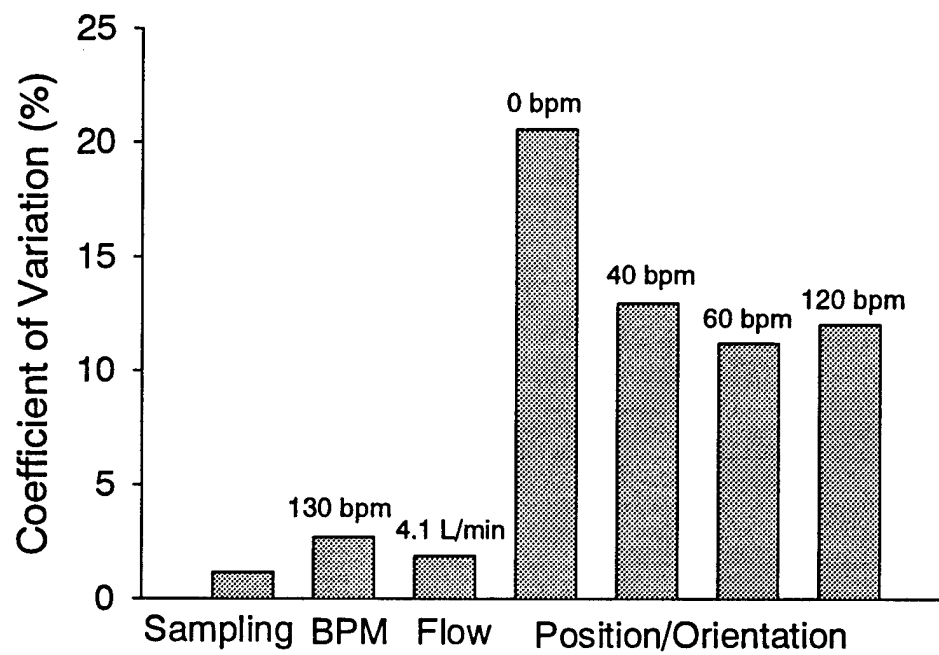


Figure 5.2 Measurement variability associated with sampling and repeated measurement condition.

average over the variability associated with prototype orientation. Thus, rather than performing repeated sampling for gas PO_2 as in our original protocol (at one prototype orientation), we now perform single gas exchange measurements at three different orientations of the prototype within the test chamber (model vena cava). At a given flow rate through the test section and a balloon pulsation rate, exchange measurements are made with the prototype in angular orientations of 0, 120 and 240 degrees rotation. The gas exchange performance of the prototypes is expressed then as mean and standard deviation over the orientations tested. With this revised protocol, gas exchange characterizations of a particular IMO prototype done on different occasions (days) will more closely agree with one another (since orientation differences are averaged over), and any differences that now exist between characterization tests of different prototypes can be more directly ascribed to real variations in gas exchange performance.

5.2 Predicting Gas Exchange in Blood

Bench characterization testing of the IMO prototypes uses distilled water as the test fluid rather than blood. This expedites prototype testing and evaluation, and enables multiple experiments to be performed on a single prototype to maximize information gained on the gas exchange characteristics of a given prototype. Estimating the exchange performance in blood from water testing is important because a given prototype exchanges more gas in blood than in water under equivalent conditions. Since water testing is simpler and more expedient, the development time and effort associated with design evaluation, design change/adjustment, and design re-evaluation is shortened.

In the first Annual Report we described our data analysis methodology for estimating gas exchange performance in blood from that measured in water, and in the past year we have gone further in evaluating this methodology. Briefly, the methodology involves a dimensionless analysis of the *in-vitro* O_2 exchange data in water, which then is used to estimate exchange performance for bench testing in blood under physiological flow conditions. The overall procedure is illustrated in Figure 5.3 and is adopted from that developed and evaluated by Vaslef et al (1994) for extracorporeal artificial lungs. At a given pulsation rate, the exchange rate, VO_2 , is determined over the relevant flow rate range, Q . The exchange rate is then recast as a device mass transfer coefficient, K , which represents the exchange rate per unit area and unit partial pressure difference

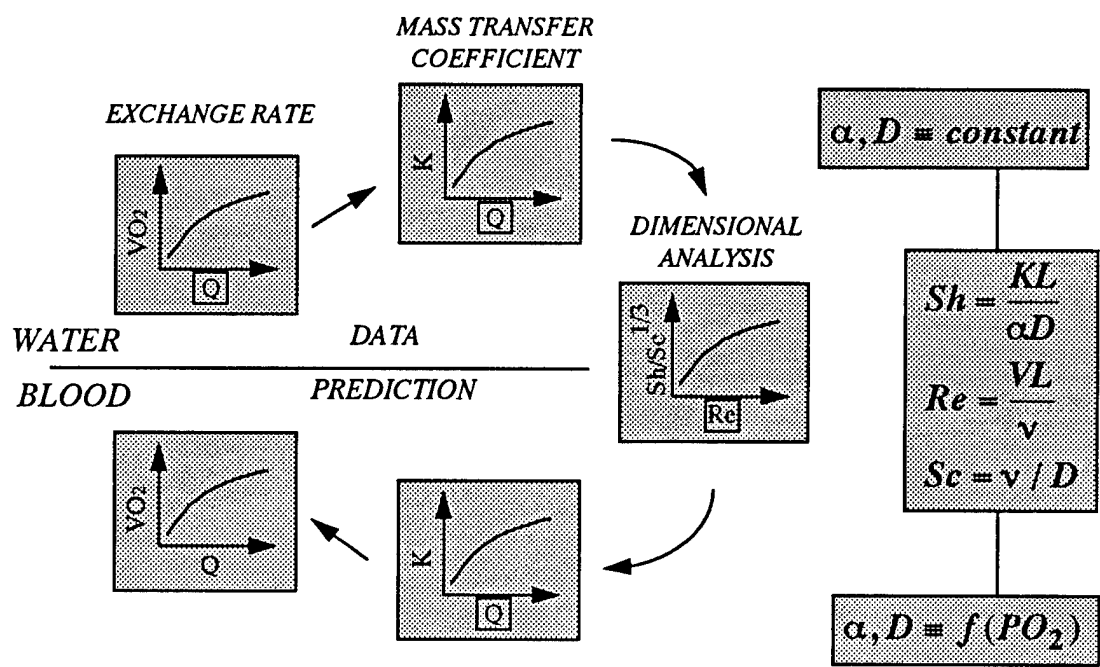


Figure 5.3 Data analysis methodology for estimating O_2 exchange in blood from measurements of O_2 exchange in water.

between gas and liquid phases. The dimensionless form of the K, Q relationship is $Sh/Sc^{1/3}$ versus Re , where Sh , Sc , and Re are the Sherwood, Schmidt, and Reynolds numbers, respectively, as defined in Figure 5.3. The dimensionless form is fluid invariant (applies to blood and water equally) since the oxygen solubility and diffusivity in the liquid, α and D respectively, and the liquid kinematic viscosity, ν , are used in the scaling. Accordingly, the dimensionless relationship can be recast into a K, Q form for blood, provided α and D account for O_2 binding to hemoglobin in blood (Vaslef, 1994), and hence the VO_2 versus Q relationship for blood can be computed.

The estimation of O_2 exchange rate in blood from water testing is evaluated in Figure 5.4. In Figure 5.4a the symbols represent the measured O_2 exchange rate in water flowing from 1 to 5 L/min. This data underwent the dimensionless analysis illustrated in Figure 5.3, and the predicted exchange rate in blood (for standard AAMI conditions) is shown in Figure 5.4a as the solid line (blood prediction). The analysis for this IMO prototype indicates an exchange rate in blood that is 2.4 fold greater than that in water. In general, all IMO prototypes which have been tested and analyzed in this manner suggest a broader range of 2 to 3 fold greater O_2 exchange rate in blood than in water. In Figure 5.4b, all available past data for the O_2 exchange rate of IMO prototypes tested in blood are compared to their respective O_2 exchange rate in saline under (otherwise) equivalent conditions. The average ratio of O_2 exchange in blood versus water indicated by the ensemble experimental data is 2.9, a ratio which is consistent with the specific IMO predictions shown in Figure 5.4a.

5.3 First Improvements in Balloon Pulsation

Past performance data for gas exchange in IMO prototypes has indicated a maximal exchange rate with balloon pulsation rates of about 60-80 bpm with a decrease in gas exchange at higher pulsation frequencies. The first IMO D series prototypes (Prototypes D01-D03) with the implantable-sized, integrated pneumatic delivery shaft (see Figure 1.2) for sweep gas inflow and outflow, and for helium delivery to the balloon could only pulsate effectively to about 60 bpm because of the pneumatic impedance of the helium pathway within the device. The first year Annual Report presented gas exchange performance data for these first three insertable-sized

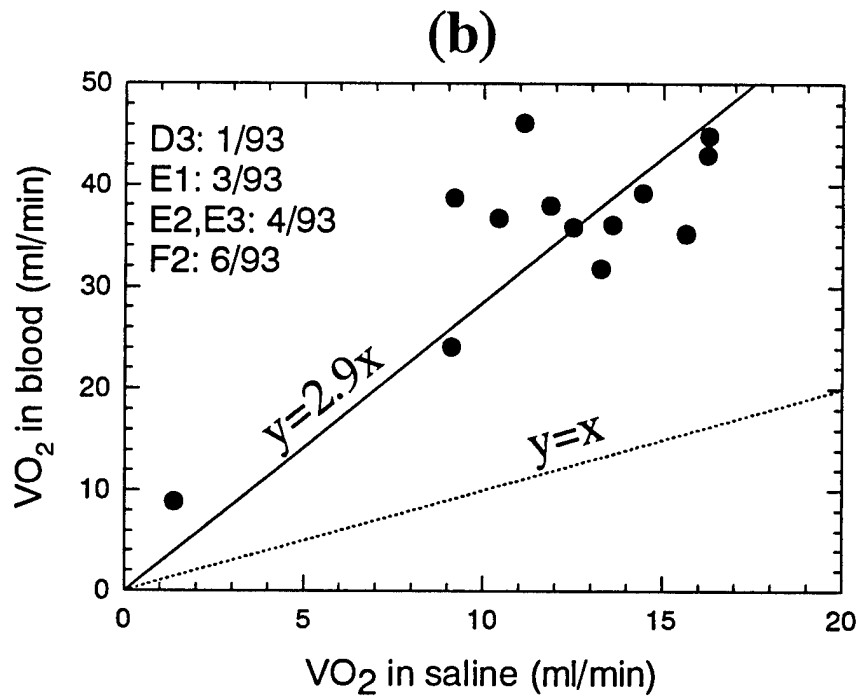
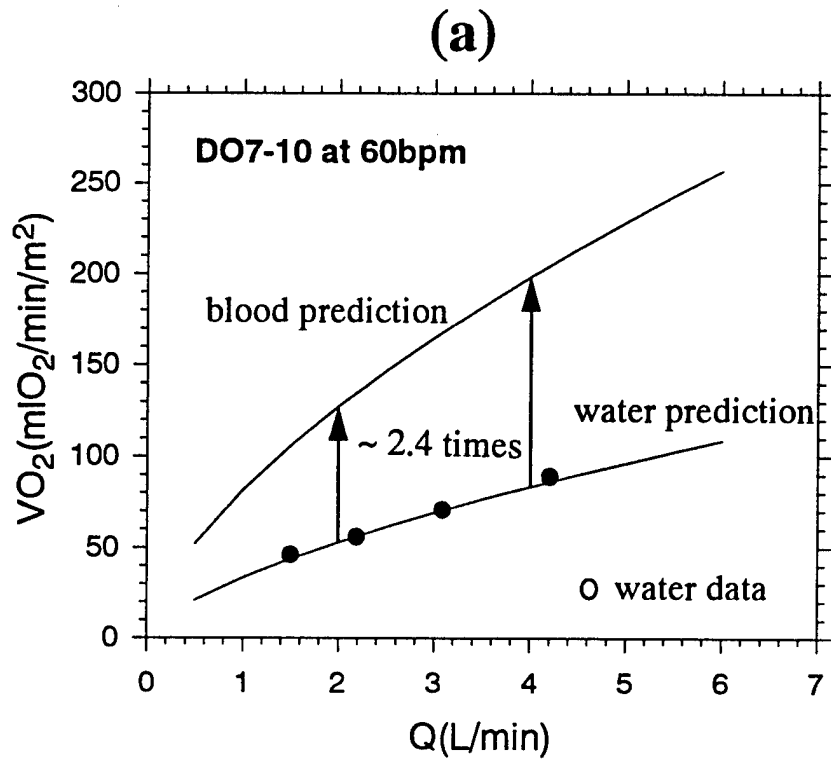


Figure 5.4 O₂ exchange of IMO prototypes in blood versus water. a) Estimates in blood from measurements in water. b) Measurements in blood versus measurements in saline.

IMO prototypes (D01-D03). This report will begin reviewing gas exchange performance with IMO device D04. Prototype D04 (received 6-6-95) was the first prototype fabricated after limitations associated with the helium pathway within the previous IMO devices (D01-D03) were identified. A simple modification of the helium pathway of IMO D04 eliminated some of the pneumatic resistance and resulted in significantly better balloon pulsation than the previous prototypes. Ultimately, further improvement in the helium pathway within the IMO prototypes was accomplished by switching to custom extruded gas delivery tubes with optimal dimensions (beginning with Prototypes D08 upward, see Section 4.2 and next section below). The scale-up of the IMO device (discussed in Chapter 7) describes a significant modification of the IMO design, use of multilumen tubing for the pneumatic delivery shaft to significantly improve the pneumatics of the helium and sweep gas pathways.

Extensive performance testing of IMO D04 has been completed and has provided valuable information relative to design development. Figure 5.5 summarizes O₂ exchange data for IMO Prototypes D03 (fabricated before design changes to helium pathway) and D04. For both prototypes, results are shown at several balloon pulsation rates and for the static balloon uninflated and inflated states. The key result is that O₂ exchange in D03 was greater with balloon pulsation than with the balloon static and uninflated. However, the O₂ exchange rate with pulsation was no more than that with the balloon left static and inflated. Thus, balloon pulsation in this prototype (and in other previous prototypes) was ineffective in augmenting dynamic mixing. Merely inflating the balloon accomplished comparable exchange rates as pulsating the balloon. This result from the characterization testing of IMO D03 (presented in our first Annual Report) was our first indication that problems existed with the pneumatic pathways within the implantable IMO D prototypes.

In contrast to the effect of balloon pulsation on gas exchange for IMO D03, the O₂ exchange rate in D04 with balloon pulsation was substantially greater than the exchange rate for static, uninflated *or static inflated*. Thus, the modifications to the helium pathway in D04 resulted in balloon pulsations which were effective in dynamically improving fluid mixing and gas exchange. These studies suggested that further improvements to the helium pathway would be beneficial to the gas exchange performance of IMO prototypes and should be explored. Figure 5.5

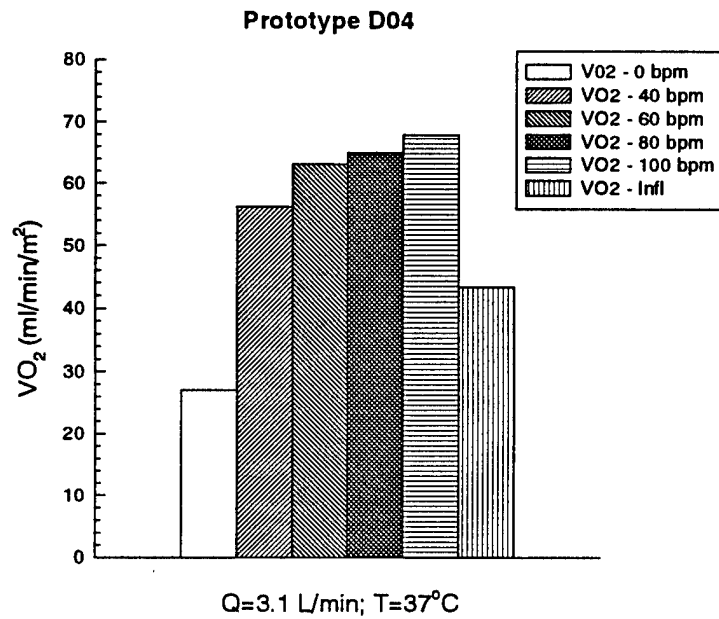
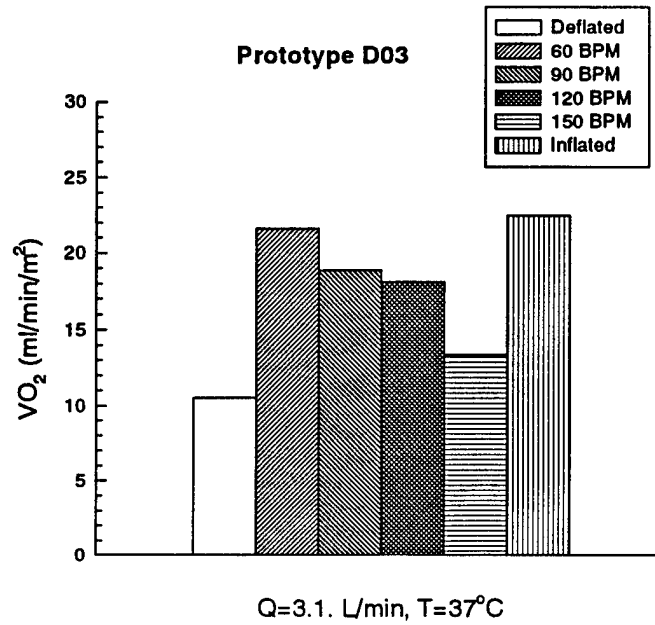


Figure 5.5 Comparison of O₂ exchange rates for IMO prototypes before (D03) and after (D04) partial modification of helium pathway.

also indicates that the O₂ exchange rate for Prototype D04 with a static inflated balloon was substantially greater than that for D03 under the same conditions. This was most likely due to better fiber constraint in the D04 prototype, which was shorter in length than D03. The shorter fiber length results in less tendency for the fibers to clump together and float up to the top of the balloon due to buoyancy forces when submerged in liquid. This difference in fiber arrangement of the prototypes (D03 vs. D04) was visually evident during testing. Thus, we also began exploring designs which better constrain the IMO fibers around the balloon when submersed.

5.4 IMO Devices with Kinked Fibers

The IVOX intravascular oxygenator employed kinked (or crimped) fibers in their bundle design as a means to distribute the fibers well within the available vessel cross-section and to eliminate blood flow shunting around the fibers. Kinked fibers undulate rather than run straight, and as a result have a reduced tendency to clump together and rise up to the top of the balloon. Kinked fibers tend to remain segregated and well distributed in the flow cross-section around the central balloon. The use of kinked fibers significantly improved gas exchange in the IVOX device (a passive oxygenator) but it was unclear whether use of kinked fibers would be beneficial to the IMO, wherein the pulsation of the balloon actively promotes fiber and fluid flow interaction (i.e. the IMO is an active oxygenator). Thus, we fabricated and tested an IMO prototype, D06, which was identical to D04 but with kinked fibers rather than straight fibers.

In preliminary testing, the O₂ exchange rate of the kinked prototype (D06) under static-inflated conditions was greater than that of the "control" IMO prototype (D04), due presumably to better fiber disposition to the flow with kinking. However, the O₂ exchange rate with balloon pulsation for the kinked fiber prototype was not greater than that for the control IMO. This suggested that the advantages of a kinked fiber may not be important when balloon pulsation is activated, or conversely that use of a kinked fiber may make balloon pulsation unnecessary. The kinked fibers in D06 during these preliminary tests, however, were not optimal.

After the initial performance testing of the D06 kinked prototype, we sent the prototype back to IMO fabrication to enhance the kinked nature of the fiber bundle by applying moderate heat to the fiber bundle while in an unstressed condition. The prototype was then re-tested in the mock loop and its performance compared to that before the enhancement, and to the control

prototype with straight fibers. The results for the enhanced prototype are summarized in Figure 5.6, where the latter date (10-25-95) indicates the kinked fiber prototype after "kink enhancement". With further kinking, the gas exchange rate in the static control case (no balloon pulsation) actually exceeded the highest rate achieved with balloon pulsation in the straight fiber prototype (occurring at 110 bpm for this prototype). This provided further evidence that kinked fiber prototypes may not benefit from incorporation of pulsating balloons (as we were able to pulsate them at that time). If so, kinked fiber prototypes might have greater gas exchange capacity by replacing the balloon space with additional fibers. The results in Figure 5.6 also raised new questions about the relation between balloon pulsation and augmenting gas exchange. Why did the additional convective flow generated by balloon pulsation have no apparent effect when the fiber membranes were kinked and well-distributed in the fiber cross-section?

The gas exchange testing with kinked and unkinked fiber IMO prototypes was performed before final modifications to the helium pathway were incorporated and before we learned the important benefit of constrained fiber bundles in pulsating IMO devices. The levels of gas exchange in the most recent IMO prototypes with constrained fiber bundles are significantly greater than the unkinked "control" IMO device used in Figure 5.6 for comparison. Thus, an IMO device based on kinked fibers without the pulsating balloon would be unlikely to provide comparable levels of gas exchange to our newest IMO design with pulsating balloon. Kinked fibers are not available commercially or readily for incorporation in IMO prototypes. Given the levels of gas exchange currently attained with (unkinked fiber) IMO prototypes, the development effort required to create kinked or crimped fibers for IMO prototypes was considered unwarranted.

5.5 IMO Devices with Modified Helium Pathway

The helium pathway was redesigned to reduce its pneumatic impedance and the resulting IMO prototypes (Prototypes D08 and higher) could pulsate effectively up to 150 or 160 bpm (see Chapter 4). These modified prototypes underwent gas exchange testing *in-vitro* (in water) to determine the degree to which improvements in balloon pulsation translated to better O₂ exchange performance. Figure 5.7 shows the gas exchange performance for a D08 series prototype, with

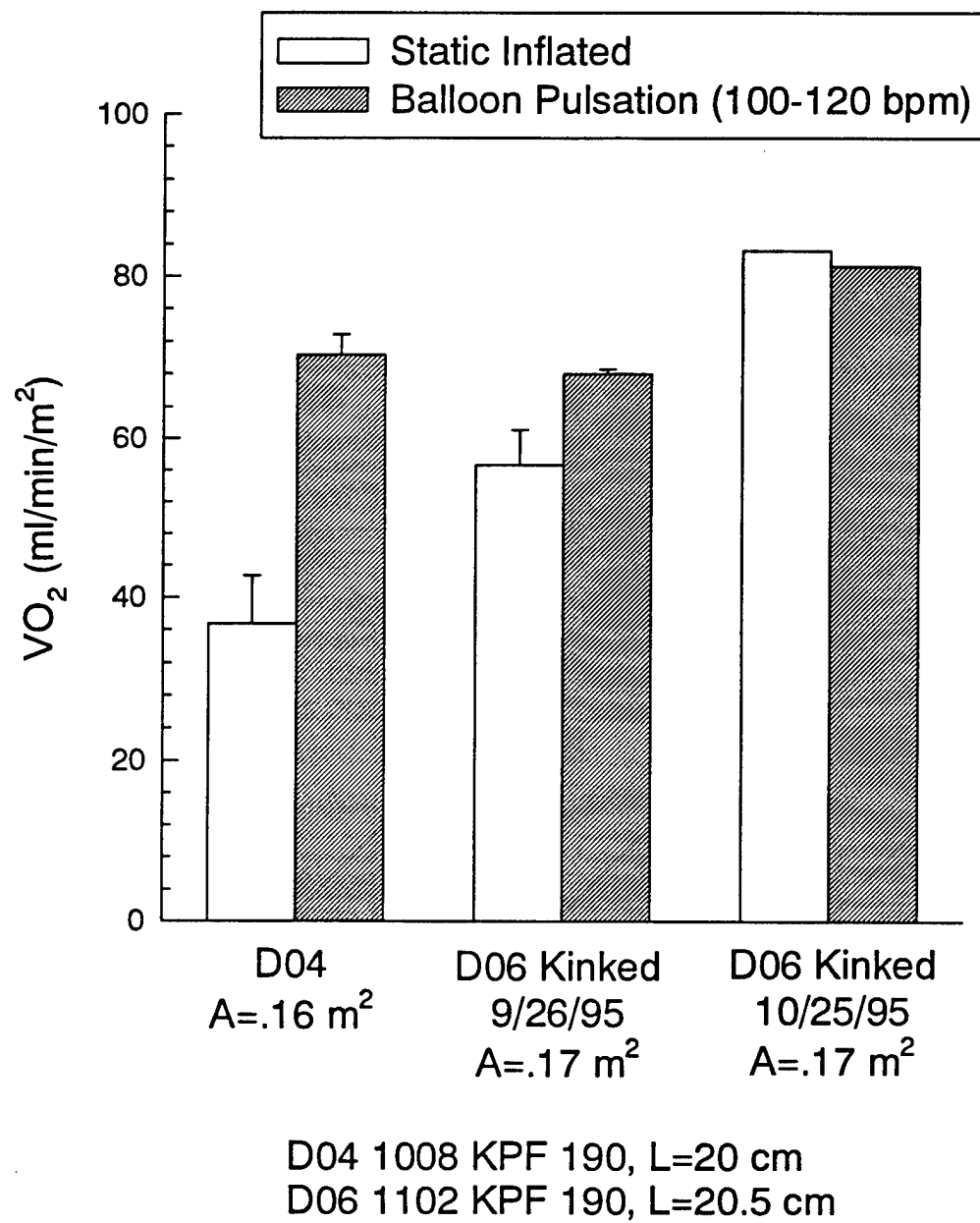


Figure 5.6 Gas exchange performance of IMO prototypes with kinked (D06) and unkinked fibers (D04).

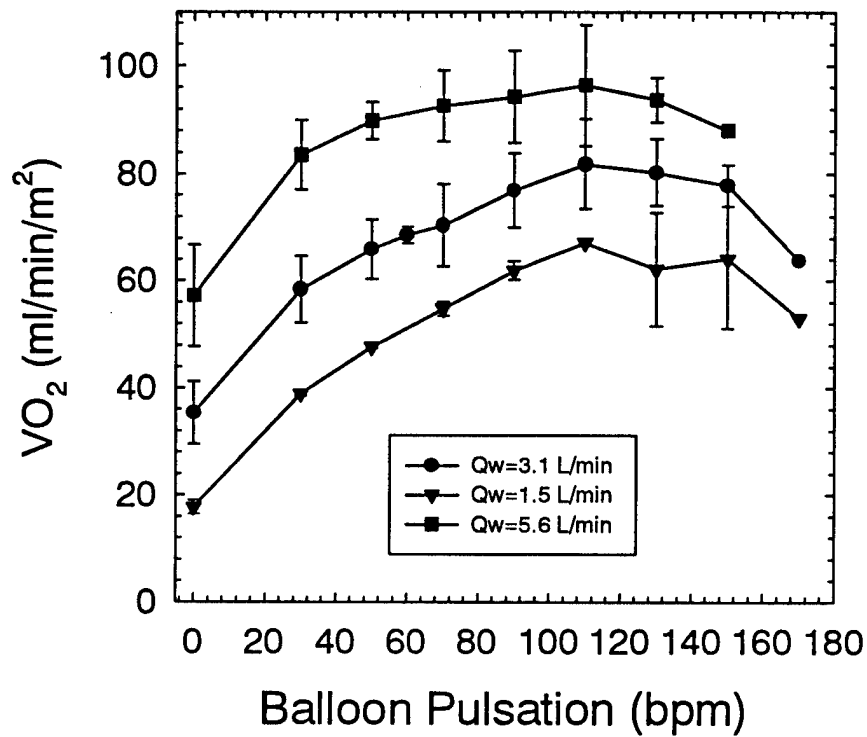


Figure 5.7 Gas exchange performance of the D08 series IMO prototypes with the redesigned helium pathway.

the redesigned helium pathway. O_2 exchange rates normalized to prototype surface area are shown versus the balloon pulsation rate. Results are given for flowrates in the test loop of 1.5, 3.1 and 5.6 liters/minute (lpm). The enhancement of gas exchange resulting from balloon pulsation shows an appreciable dependence on flowrate through the model vena cava. At all flowrates the augmentation appears to level off, then drop off as pulsation frequency goes from about 120 bpm to 140 bpm. This redesigned prototype, however, can pulsate effectively up to 160-170 bpm, as measured in our separate apparatus for determining the balloon pulsation frequency spectrum (see Chapter 4). Closer inspection of the gas exchange data indicated that in only one position (orientation), the prototype's gas exchange decreased in the 120 to 140 bpm range. This suggested that we examine more closely the driving of balloon pulsation with our Datascope Intra-Aortic Balloon Pump console to ensure that balloon inflation and deflation timing parameters were selected to optimize gas exchange. Our rationale was that the results in Figure 5.7 suggest that the balloon may have been activated under suboptimal parameters.

Figure 5.8 shows the results of examining gas exchange in this prototype as a function of the inflation/deflation timing of the balloon drive system (relative time spent in inflation compared to deflation). These results indicated that we could improve (optimize) gas exchange at the higher beat rates by operating with more time in balloon inflation versus deflation. This adjustment is less critical at lower frequencies, but becomes increasingly important at higher frequencies as we push the capabilities of our drive system. The current drive system, however, allows only a maximum inflation/deflation ratio of unity at the higher beat rates. Thus, we are exploring designs for our own balloon drive system with the capability of longer inflation timing at higher beat rates. Furthermore, based on the results shown in Figure 5.8 we have now adopted a specific set of inflation/deflation timing parameters with the existing drive system under which to operate our IMO balloons for optimal gas exchange.

The O_2 exchange rate versus balloon pulsation frequency for a modified IMO prototype (D08.2) operated under the new testing (i.e. orientation averaging) and balloon operation protocols is shown in Figure 5.9. Shown are the normalized O_2 exchange rates as a function of

DO8.1

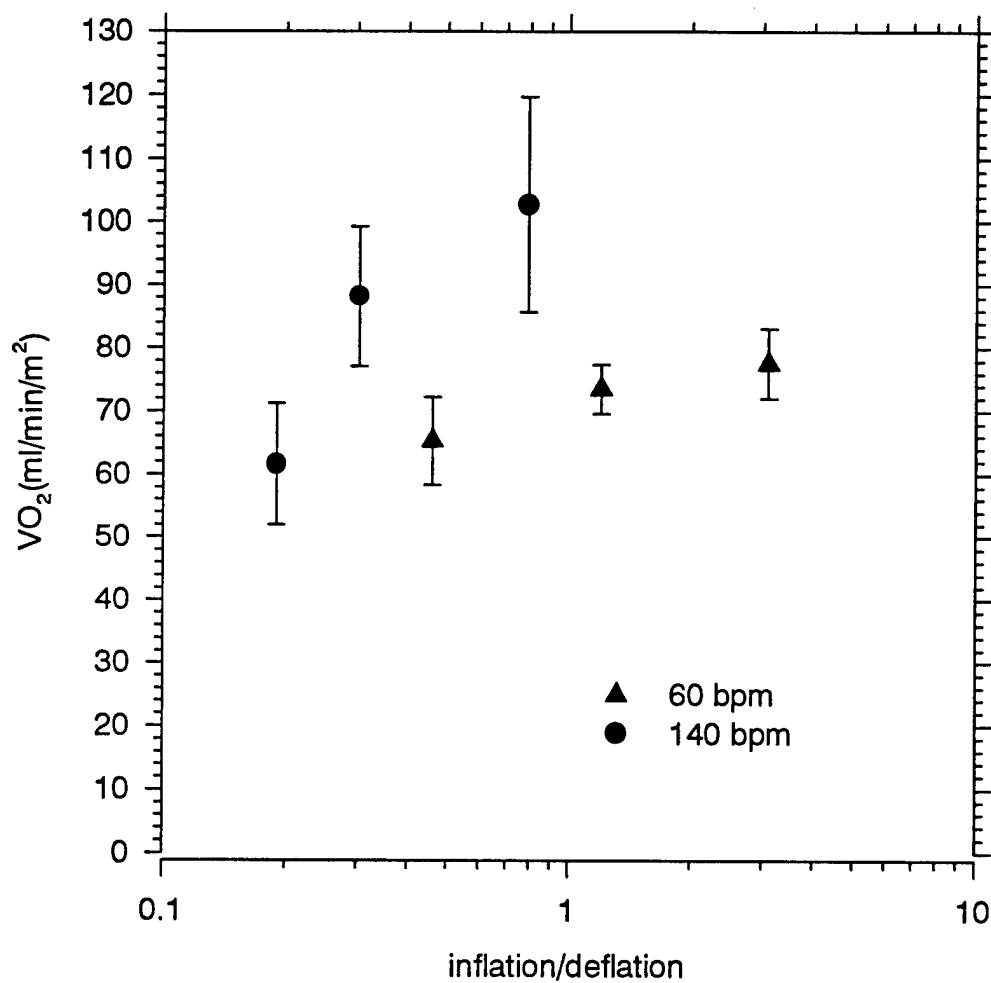


Figure 5.8 Effect of balloon inflation/deflation timing on O_2 exchange.

balloon pulsation rate for a flowrate of 3.1 lpm through the test section. The results in Figure 5.9 represent optimal achievable exchange rates (in water) with the redesigned helium pathway D series prototype (D08 and above). With no balloon pulsation (but the balloon static inflated), the O_2 exchange was about 45 ml/min/m² in water. With increasing frequency of balloon pulsation, the O_2 exchange rate continually increased up to 150 bpm, the highest beat rate tested. The maximal O_2 exchange rate was 90 ml/min/m² at the highest beat rate, which represents a doubling of gas exchange compared to the static prototype (with the balloon inflated). Thus, modifications to the helium pathway eliminated the drop in gas exchange which occurred above 60-80 bpm, which was associated with the balloon failing in earlier prototypes.

Although the balloons in these prototypes can pulsate effectively up to 150 bpm (see Chapter 4), the O_2 exchange rate essentially reaches a plateau with increasing frequency above about 80 bpm and there appears only a modest additional gain in gas exchange going up to the maximum frequency of 150 bpm. Since the balloon is able to fill and empty completely, the convective flow generated by the balloon at 150 bpm is nearly double that at 80 bpm, yet this additional convective flow energy appears to have little effect on reducing mass transfer resistance. Consider that in going from 60 bpm to 120 bpm the convective flow generated by the balloon has essentially doubled, but the gas exchange rate increases only a few percent for the D08 series prototype. In both prototypes, the overall enhancement due to balloon pulsation is just slightly less than 100%, or a near doubling of the gas exchange without balloon activation.

These results directed attention towards understanding the mechanisms underlying balloon enhanced gas exchange and establishing what factors may be responsible for the behaviors underlying Figure 5.9. In particular, we needed to establish why there was not a substantial increase in gas exchange with increasing frequency, and why we did not engender an enhancement greater than the doubling of gas exchange which is apparent in Figure 5.9. Recall that our original thinking was that this behavior was due to limitations in balloon pulsation because of the flow resistance of the helium pathway within our device. This interpretation was consistent with the balloon pulsation frequency spectrums of our early prototypes (see first Annual Report). The helium pathway was redesigned, however, and the prototypes tested here (results in Figure 5.9) can pulsate effectively (full balloon inflation and deflation) up to 150-170 bpm. Thus we cannot interpret the results shown in Figure 5.9 as an attenuation of balloon function.

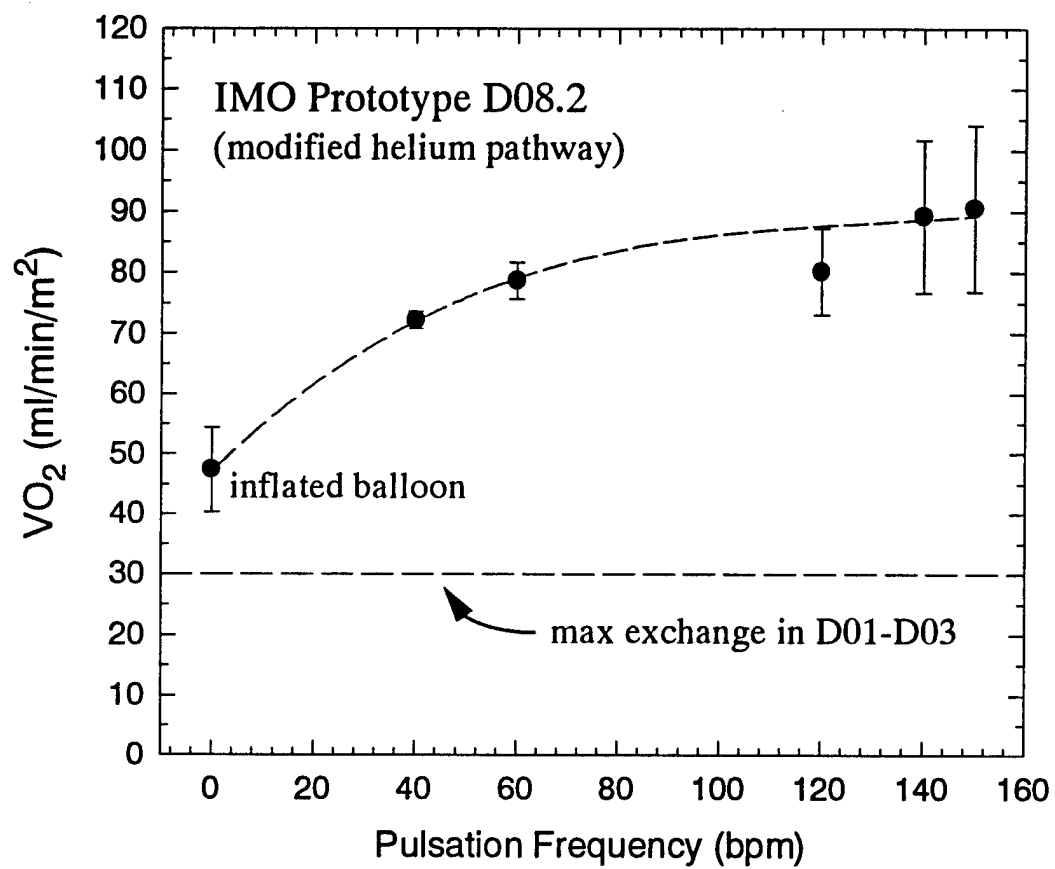


Figure 5.9 Gas exchange performance of recent IMO prototype D08 with modified helium pathway and optimal balloon pulsation timing parameters.

In principle, the augmentation of gas exchange with balloon pulsation should be associated with the convective flow generated by balloon activation, which runs perpendicular to the fibers (cross-flow). With cross-flow to the fibers, the thickness of diffusional boundary layers on the outside of the fibers is reduced, and as a result gas exchange is increased. Basic boundary layer theory would predict that for the same flow velocity perpendicular to a hollow fiber as parallel to a hollow fiber, gas exchange is greater (in cross-flow) by approximately the square-root of the length to diameter ratio of the fiber. That translates into expected enhancements with balloon pulsation of essentially an order-of-magnitude. The results in Figure 5.9, however, indicate that the maximum gas exchange with balloon activation is only double that without balloon activation, thus suggesting that the benefits of cross-flow to the fibers is not being fully realized. To explore this idea further we measured the gas exchange performance of an IMO prototype with balloon pulsation, and compared it to the gas exchange performance of the same prototype with an external, stand-alone balloon pulsating upstream of the device. The results are shown in Figure 5.10, where integral balloon refers to the IMO device tested with its own balloon pulsating, and stand-alone balloon refers to an external balloon pulsating while the integral balloon is quiescent. Gas exchange with integral pulsation is only slightly greater than that with the stand-alone balloon (Figure 5.10). Since the stand alone balloon is not within the fiber bundle, the convective flow generated by its activation is expected to be predominantly parallel to the fibers rather than cross-flow to the fibers, and stand-alone balloon pulsation represents adding pulsatility to the parallel (longitudinal) flow component. Thus, the results in Figure 5.10 suggest that the effect of (integral) balloon pulsation with the IMO device is essentially adding pulsatility (or otherwise disturbing) the longitudinal or parallel flow to the IMO device, rather than generating an effective cross-flow to the fibers. We expect that realizing an appreciable enhancement of gas exchange with balloon pulsation in an IMO device (above that shown in Figure 5.9) will require effective generation of cross-flow to the fibers.

What factors might be responsible for inadequate cross-flow to the fibers with balloon pulsation in our current prototypes? We can eliminate failure of the balloon to fill and empty since these prototypes can pulsate effectively to 150-170 bpm. Thus, at 120 bpm, for instance, the balloon is generating a radial convective flow of 3.6 L/min, comparable to the longitudinal flow component (3.1 L/min) used in characterization testing of IMO devices. Our principle hypothesis

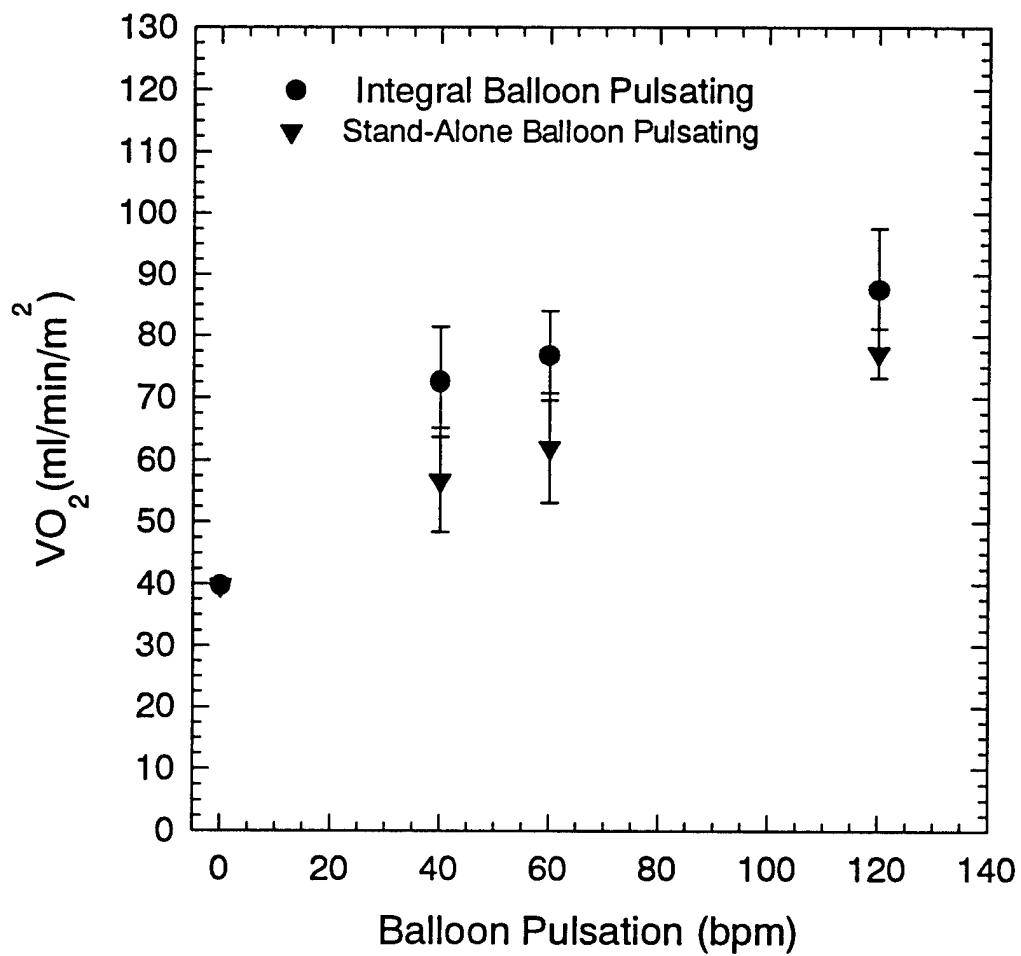


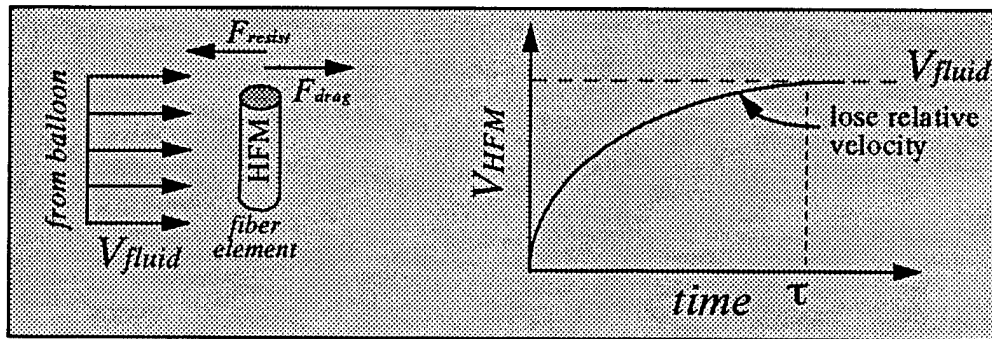
Figure 5.10 Gas exchange with integral balloon versus a separate stand-alone balloon placed behind the prototype.

was that balloon pulsation in the IMO device was not generating effective cross-flow to the fiber bundle because of fiber motion engendered by balloon pulsation. The idea underlying this principal hypothesis is illustrated in Figure 5.11. The convective flow generated by the balloon exerts a drag force on each fiber element, which acts to accelerate the fiber element. The acceleration rate will depend on the forces restraining or constraining the fiber element from moving. In the limit of a relatively unconstrained fiber, the sole restraining force is the inertia of the fiber element. If the viscous drag force exceeds the fiber element inertia, the fiber will accelerate and reach the convective fluid flow velocity in a time of τ , wherein all relative velocity between fluid and fiber is lost. Figure 5.11 indicates that this time, normalized to the period of balloon pulsation, is given by a dimensionless group of variables representing the ratio of fiber inertia to viscous drag exerted on the fiber elements. As indicated in Figure 5.11, for values of these variables relevant to IMO conditions, the normalized time is very small, viscous drag swamps fiber inertia, and a substantial loss of relative velocity between fluid and fiber might be expected. Thus, the results in Figure 5.10 and the hypothesis illustrated in Figure 5.11 suggested that IMO development should explore prototypes with improved fiber constraint to maintain effective relative velocity between fibers and the convective flow generated by the balloon.

5.6 IMO Devices with Constrained Fiber Bundles

The first IMO device with improved fiber constraint (Prototype D10) incorporated a mesh sheath immediately inside the fiber bundle (between integral balloon and fibers) and a mesh sheath immediately outside the fiber bundle. Thus a “hard” annular space was created (between these two mesh sheaths) within which the fibers reside, even with balloon pulsation. Within this annular space, however, the fibers were not constrained. The gas exchange performance of this IMO device (not shown here) was poor, and flow visualization indicated that the convective flow being generated by the balloon was shunting through natural gaps in the fiber bundle within the annular space created by the two sheaths. Thus, one problem was traded for another. While the fibers were constrained from moving with balloon activation, the effect of natural gaps within the fiber bundle was exacerbated and most of the convective flow generated by the balloon was preferentially diverted through these gaps (a channeling phenomena), having little effect on gas

illustration



limit of unconstrained fiber element:

dynamics

$$\frac{\tau}{\tau_{period}} \sim \frac{\rho_{HFM} f d^2}{\mu} \sim \frac{\text{fiber inertia}}{\text{viscous drag}}$$

~ 0.01
little relative motion

Figure 5.11 Schematic illustrating loss of relative fiber-fluid motion.

exchange at the individual fiber level. Thus, constraining fibers means that special attention must be given to eliminating opportunities for shunting of the convective flow generated by the balloon through “gaps” within the fiber bundle.

One natural way of constraining hollow fibers while maintaining relatively uniform spacing within the fiber bundle (i.e. eliminating gaps) is to use hollow fiber mats or fabrics in place of free fibers. Fiber mats or fabrics are matrices of parallel, uniformly spaced hollow fibers with regularly spaced “support” fibers or yarns running perpendicular to the hollow fibers. An IMO D prototype (D14) was fabricated using a KPF 280 fiber mat rather than individual, independent fibers. The KPF 280 fiber mat contains support threads about every 1 cm along each fibers length connecting the fiber to its neighbor. Thus, the fiber bundle constructed using the KPF 280 mat has fibers which are spaced relatively uniformly to help eliminate the potential for channeling of the convective flow generated by the balloon through the fiber bundle. As a result, the shunting of balloon generated flow is reduced in the IMO D14 prototype. The support threads are also sufficient to reduce fiber motion resulting from balloon pulsation.

The gas exchange performance of the first constrained fiber prototype (IMO D14) is shown in Figure 5.12 and compared to several of the key IMO prototypes studied during prototype development history. In comparison to the previously discussed IMO prototype with the modified helium pathway and free fibers (D08), the tendency toward a plateauing of gas exchange with balloon pulsation frequency has been markedly reduced with the constrained fiber prototype (D14). Unlike the unconstrained (free) fiber bundle, gas exchange continues to increase with increasing balloon pulsation above 60 bpm. The level of gas exchange appears to be increasing (not plateauing) up to 170 bpm, at which point balloon filling and emptying begins to be compromised (not able to fill and empty completely). This prototype achieved a gas exchange rate of 125 ml/min/m^2 , which is nearly 40% greater than the gas exchange plateau characteristic of IMO prototypes (D08) with the same helium pathway but with unconstrained (free) fiber bundles. Figure 5.12 also shows the gas exchange performance of the constrained fiber prototype in the context of the development history for the implantable-sized IMO prototypes. Not all prototypes

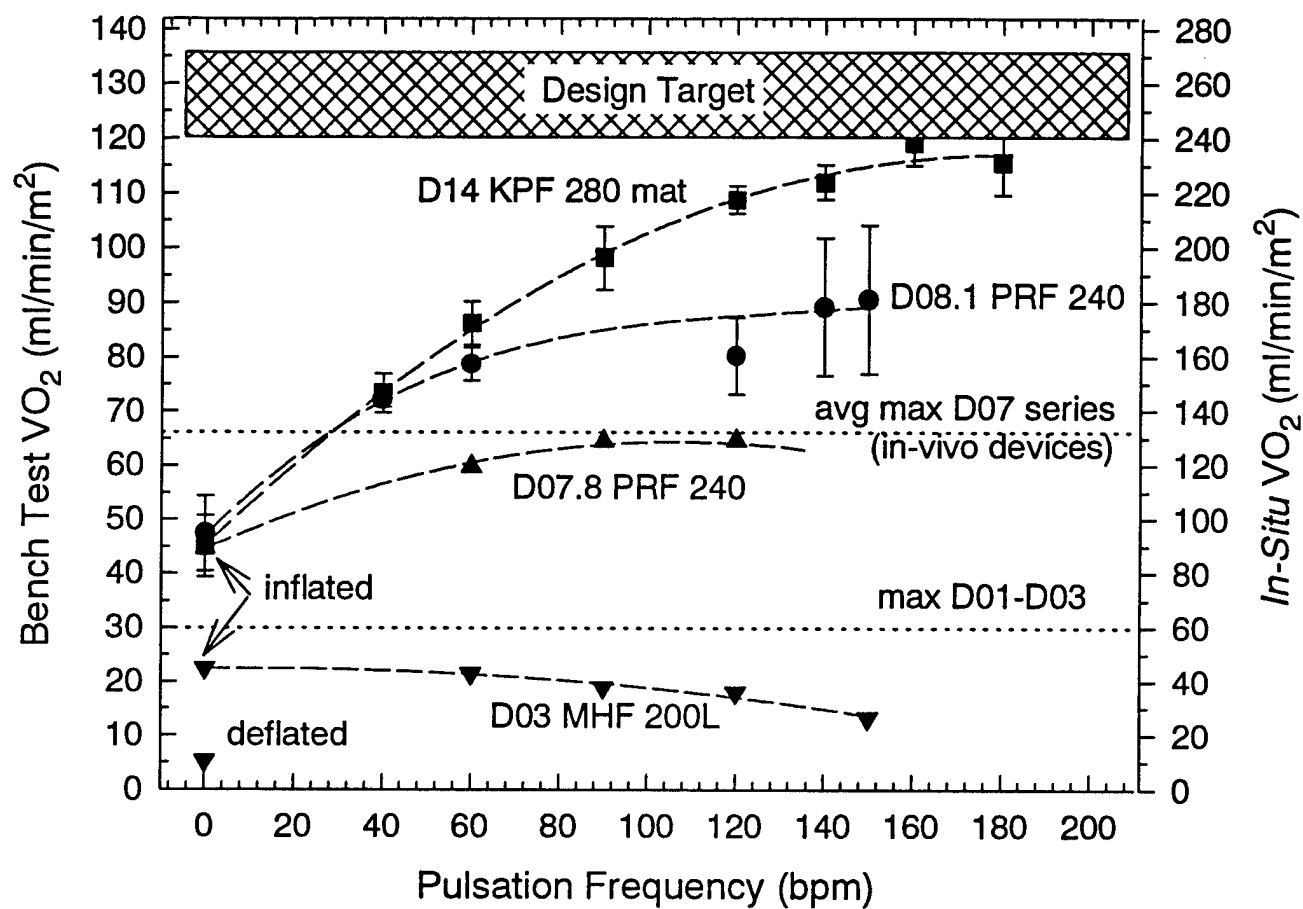


Figure 5.12 Improvements in gas exchange during prototype development. Actual bench test measurements and projected *in-situ* exchange rates.

are shown, only key ones during the development process. The first series of implantable-sized IMO prototypes (D03 representative) had significant problems with balloon pulsation and gas exchange levels which actually decreased with increasing balloon pulsation above 60 bpm. Even without balloon pulsation (0 bpm) the gas exchange level of this first series was relatively low due to the hollow fibers used, which were MHF 200 composite fibers made by Mitsubishi Rayon. These fibers were subsequently found in independent fiber testing to have an unacceptably low gas transfer permeability due to the polyurethane true membrane used in this composite fiber (see Chapter 3). Subsequently, some modifications were made to improve the pneumatics of the helium pathway and noncomposite, microporous fibers were used in prototypes. This series of IMO prototypes (D07.8 representative) could pulsate effectively up to about 120 bpm and the gas exchange levels did increase with balloon pulsation (as compared to no increase for previous series). Without balloon pulsation, gas exchange was also increased as a result of using a microporous rather than composite fiber. The D07 series of IMO prototypes was also the series that we began animal testing on, and these results will be described in Chapter 6.

The next series of IMO prototypes (D08 and above) made use of the redesigned helium pathway and could pulsate effectively up to about 160 bpm. As previously described, the use of constrained fiber bundles (D14) for these IMO prototypes was key in eliminating the plateauing of gas exchange with increasing pulsation frequency (D08), and in maximizing the gas exchange benefit of the improved pulsatility of these more recent prototypes. In the context of the IMO prototype development history, the overall improvement in the gas exchange performance of IMO prototypes shown in Figure 5.12 is significant. The maximum level of gas exchange with the D14 constrained fiber prototype is nearly 4 fold greater than the first of our implantable-sized IMO prototypes. These results are encouraging and have shifted our current IMO development efforts to fabricating prototypes with better constrained fiber bundles and with special attention given to relatively uniformly spaced fibers with little potential for shunting of the balloon generated flow through preferential pathways.

The levels of gas exchange accomplished with the constrained fiber bundle device (D14) are within or close to our design target for gas exchange, indicated within the hatched region of Figure 5.12. The design target range is determined as follows. We previously described use of a data analysis technique whereby gas exchange levels in blood can be estimated from testing results

in water (Section 5.2) and that typically a 2-2.5 fold greater rate of gas exchange occurs with an IMO device in blood under otherwise comparable conditions. Assuming a conservative factor of 2, the right-hand ordinate of Figure 5.12 displays estimated *in-situ* blood exchange values for the devices tested. Our gas exchange design target of 50% of baseline metabolic rates (or about 120 - 135 ml/min) translates to a normalized target rate of 240-270 ml/min/m², assuming an ultimate device with up to 0.5 m² of membrane area.

The constrained fiber bundle device tested above (IMO D14) used the Mitsubishi KPF 280 fiber mat, which is composed of relatively large hollow fibers, with an outer diameter of 380 microns. The large size of these fibers limits the number of fibers that can be incorporated into an IMO prototype (because of manifold size) and hence limits the surface area of the IMO fiber bundle. Ultimately constrained fiber bundles will need to be fabricated using the smallest hollow fiber membranes available. Working towards this direction, we fabricated an IMO constrained fiber bundle device (D17 series) using a hollow fiber fabric available from Hoechst-Celanese (Celgard 240 fiber fabric). The Celgard 240 fabric uses hollow fibers with an outer diameter of about 300 microns, which is significantly less than the 380 micron outer diameter of the KPF 280 mat fibers.

Figure 5.13 shows the gas exchange performance of the IMO D17 constrained fiber device as a function of balloon pulsation frequency. The results are compared to the gas exchange performance of an otherwise identical IMO prototype (D08), which even uses the same fiber as D17, but in free fiber rather than fiber fabric form. The results for the D17 constrained fiber device are similar to those for the previous D14 constrained fiber device (Figure 5.12). Gas exchange levels continually increase with balloon pulsation frequency, and the level of gas exchange essentially reaches the design target for IMO device development. Comparison to the gas exchange levels of D08 indicates the direct gas exchange benefits of improved fiber distribution around the pulsating balloon. That the level of gas exchange for the D17 constrained fiber prototype is comparable to that for the previous D14 constrained device is significant. The smaller fibers of the Celgard 240 fabric allowed for 665 fibers within the bundle as compared to 385 fibers for the D14 prototype, with the surface area of D17 being about twice that of D14. The comparable levels of gas exchange per unit surface area of the two devices (D17 versus D14) means that the overall (absolute) gas exchange of constrained fiber devices may scale directly with

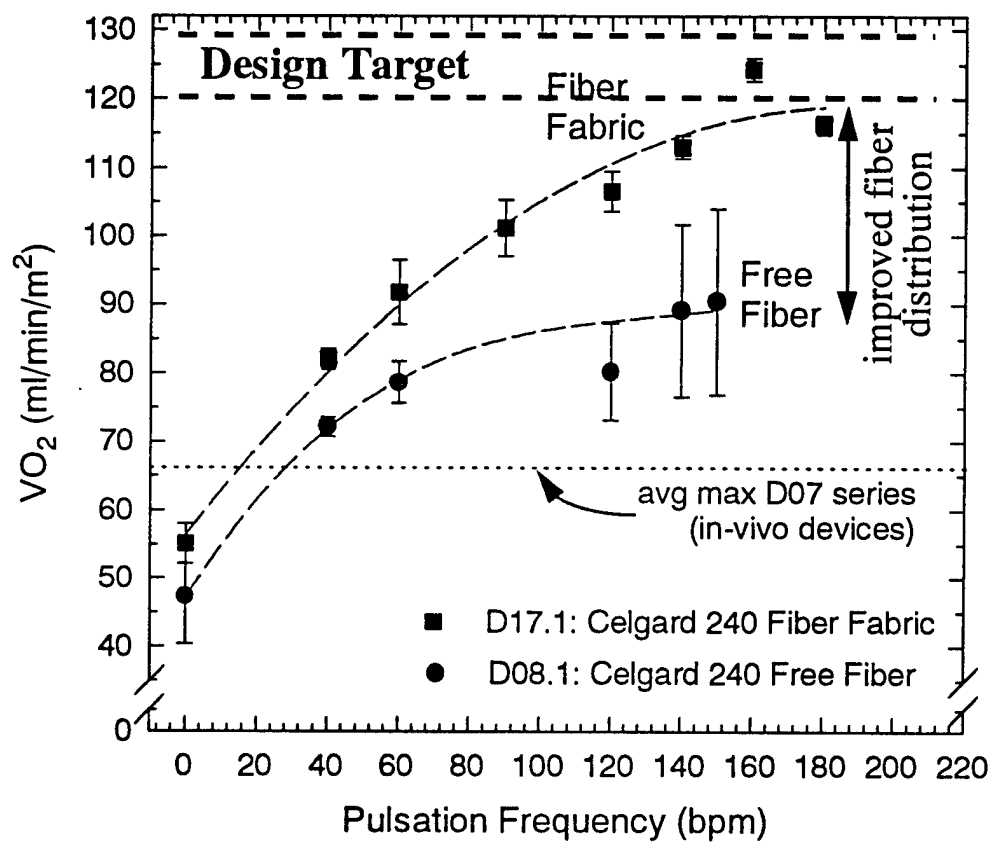


Figure 5.13 Gas exchange performance of the most recent IMO prototype shown in the context of the IMO prototype development history.

fiber bundle surface area. Thus, IMO constrained fiber bundle devices need to be fabricated with the smallest hollow fiber membranes commercially available, which would allow for the greatest fiber surface area per fiber bundle. In Chapter 8 we will describe new development efforts undertaken to fabricate hollow fiber fabrics using the KPF 190 hollow fiber membrane, which has a significantly smaller outer diameter than either the KPF 280 or Celgard 240 hollow fibers.

5.7 Summary of IMO Development History

Figure 5.14 summarizes the development history just described of the implantable sized IMO device in terms of the maximum levels of gas exchange accomplished in select IMO prototypes along the development pathway. Gas exchange levels are shown as those directly measured during bench testing (normalized to device surface area), as well as estimated *in-situ* values based on estimated gas exchange in blood flow from tests in water under otherwise comparable conditions. Improvements were made, and are indicated, in the a) pulsability of the IMO prototypes (the pulsation frequency leading to maximum gas exchange levels), b) the type of fiber used in the bundle, and c) the constrained versus free fiber nature of the fiber bundle. These improvements have systematically led to IMO prototypes with increasing gas exchange levels, greater gas exchange capacities, and exchange performance reaching the design target of the IMO device.

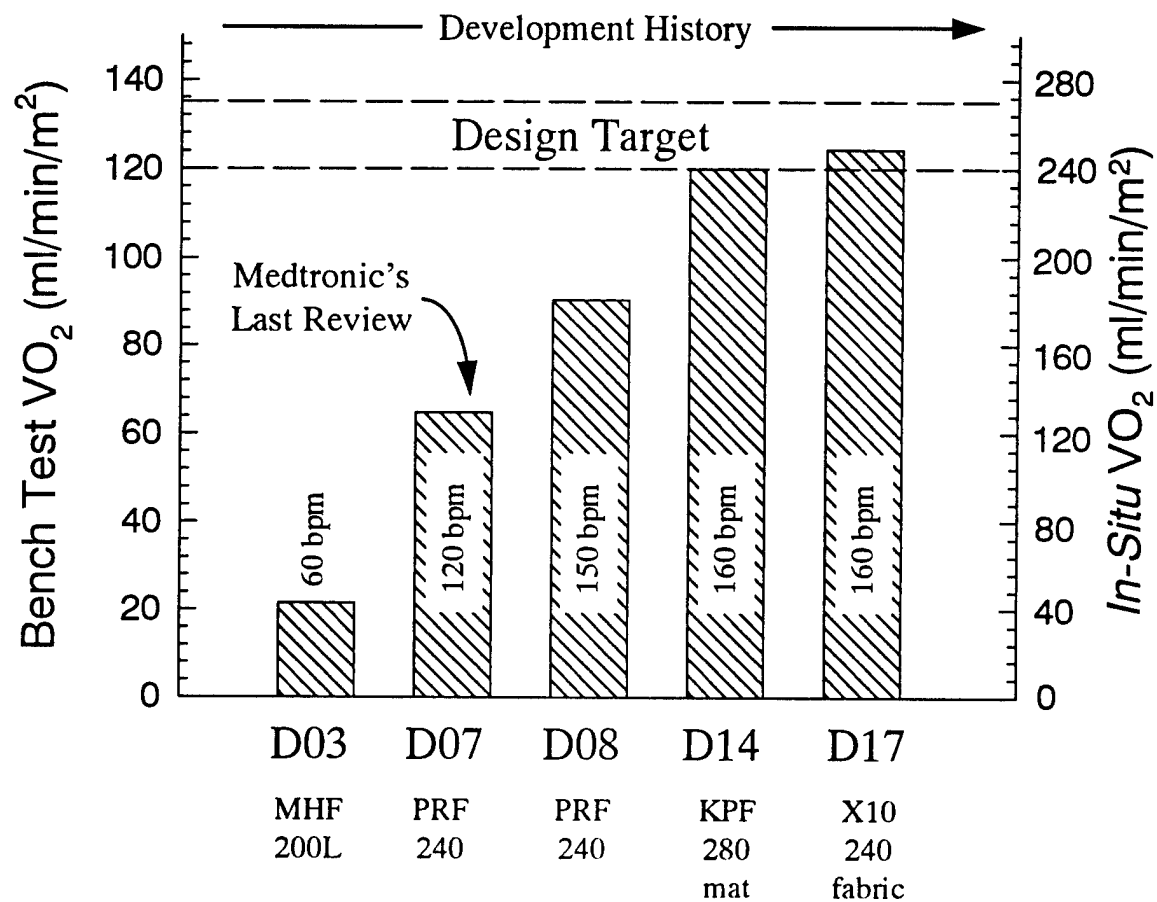


Figure 5.14 Summary of the developmental history of IMO prototypes in terms of their maximum levels of gas exchange accomplished.

6. IN-VIVO IMO STUDIES

During the contract period, a series of animal studies were conducted to evaluate IMO performance and biocompatibility *in-situ*. The goals of these studies were to establish the level of gas exchange accomplishable with the current IMO design *in-vivo*, to explore consistency of gas exchange over extended IMO contact with blood *in-situ*, to examine the effect of the device on hemodynamics during the implantation period, and to evaluate the general response of the host to the device (biocompatibility issues). A total of nine IMO devices were implanted in 60-70 kg calves. Six experiments were acute studies lasting up to 6 hours in duration and focusing on the gas exchange level of the IMO *in-situ*. The remaining three experiments were chronic studies, invoking planned 2 to 3 day implants and examining issues of gas exchange consistency and device biocompatibility. The protocols of acute and chronic experiments vary slightly and each is described completely in this section.

6.1 Experimental Methods

Surgical Methods and Animal Instrumentation. Prior to implantation, the calves (68.9 ± 2.3 kg) were premedicated with 0.5 mg/kg atropine, induced with 11 mg/kg brevitall, and endotracheally intubated. Isoflurane (1-2.5%) was mixed with low-flow oxygen and room air (1:1), and the animal was placed on a volume-controlled ventilator (Penlon AM1000, Abingdon, UK). The animal was then placed in left lateral decubitus position, the neck was shaved, prepped with betadine and alcohol, and draped. The left cervical region was incised to expose the jugular and carotid vessels. An 18G arterial catheter in the right carotid artery was connected to a fluid-filled pressure transducer (Baxter Healthcare Corp., Edwards Division, Irvine, CA). A 7 Fr Swan-Ganz thermodilution catheter, connected to a cardiac output monitor (Model SAT-2, Baxter Healthcare Corp.) was placed in the right external jugular and advanced approximately 50 cm into the pulmonary artery. A 4 Fr pediatric pulmonary artery catheter (Arrow Intl., Reading, PA) was placed in the left femoral vein and advanced into the inferior vena cava (30 cm). A pressure and electrocardiograph monitor (Hewlett Packard, Andover, MA) was used to monitor arterial, pulmonary, central venous and inferior vena caval pressures. Blood gas tensions were measured with a blood gas machine (Model 505, ABL Radiometer, Denmark) and co-oximeter (Model 482,

Instrumentation Laboratory, Lexington, MA). Anticoagulation was monitored by measurement of activated clotting times (ACT) using an ACT measuring device (Hemachron Jr., Intl. Teledyne Corp., Edison, NJ). Continuous mass spectroscopy with a medical gas analyzer (Model 1100, Marquette Electronics, Milwaukee, WI) was used for measurement of oxygen and carbon dioxide gas exchange rates. A Gould recorder (Gould, Inc., Cleveland, OH) was used for data collection. Body temperature was maintained at 37°C by the use of a heating pad.

Baseline hemodynamic data and arterial and venous gas tensions were obtained. The animal was then heparinized with 400 units/kg and a Satinsky clamp was placed on the external jugular vein. The IMO device intended for insertion was soaked in 25% human albumin immediately prior to insertion. Polypropylene purse-string sutures were placed, a 2 cm venotomy was performed and the IMO device was inserted as the Satinsky clamp was removed. The device was advanced caudally, with the tip of the device extending to the inferior vena cava. By furling the free fiber devices fully, we were able to tighten the fibers around the balloon to allow smoother passage of the device. Constrained fiber devices did not require furling for insertion due to their compact nature. In some experiments the proximal vein was ligated to improve hemostasis at the entry site.

Oxygenator sweep gas (100% O₂) was delivered through the IMO at 3 L/min under vacuum pressure (see next section). Since the IMO devices were scaled-down prototypes, mechanical ventilation was continued at normal rates (0.3 L/kg minute ventilation and 50% FIO₂) to provide adequate respiratory support of the animal, although in several experiments a ventilator challenge was performed by decreasing minute ventilation 50%. The balloon was pulsed at various beat rates ranging from 40 to 180 bpm for variable time periods, with static inflation of the balloon serving as control in several experiments. Hemodynamic values and blood gas tensions were obtained at each 15-30 minute interval, and after each change in balloon pump setting. Plasma free hemoglobin was measured at one, two, four, and six hours. Heparin was administered continuously as an IV drip (initially 0.5-1.0 mg/kg/hr; in the first two experiments only bolus doses were given). ACT was determined hourly and maintained at 400-450 seconds with repeat heparin bolus and adjustment in the IV drip as needed. Crystalloid solution was administered at 100 ml/hour. At the completion of the study, while still fully anesthetized, the animal was euthanized with an injection of potassium chloride. Thoracic and abdominal organs as

well as the vascular structures were examined at necropsy and the explanted device was carefully examined.

Chronic studies, such as the latter two discussed in this section, (D07 and D08) ran for two days and therefore necessitated slightly modified protocols. To minimize the chance of infection, a full sterile field was maintained throughout the implantation surgery. The IMO device and any materials or instruments that came into direct contact with the animal were sterilized, and any persons involved in the surgery scrubbed and followed standard sterile practice until the incision was closed. Kefzol (1 gm IV tid), an antibiotic, was administered intraoperatively and continued each day thereafter to avoid infection throughout the experiment. Immediately after implantation and animal stabilization, anesthesia was eliminated and the animal was awakened so that any changes in IMO function during the awake state could be monitored. The animal was then transferred from the operating room to a pen in a monitoring room where its condition was continuously observed by staff technicians and the veterinarian. The animal was tethered to the front of the pen allowing it to reach food and water, and sit or stand ad lib. Restraint was necessary since excessive movement could dislodge the oxygenator creating a potential bleeding problem for the animal. Pain was assessed by studying the animals posture, attitude, blood pressure and functionality, especially, sitting, standing, eating, drinking and breathing. Banamine (1mg/kg), a pain medication, was administered via IV drip for 48 hours post-operatively and as needed thereafter. The IMO pulsed continuously at 60 bpm. All animal procedures were conducted in accordance with NIH and University guidelines for the care and use of experimental animals.

Pneumatic Circuitry and Gas Exchange Rates The gas exchange rate of the IMO cannot be determined reliably from vena caval blood gas measurements upstream and downstream of the device due to the multiple sources of venous blood flow into the vena cava (i.e., iliac, portal, hepatic, brachiocephalic, azygos). Determination of all the requisite blood flow rates and gas tensions is not feasible. Accordingly, gas exchange rates were determined from gas-side measurements. The implanted IMO, associated equipment, and pneumatic circuitry are schematically demonstrated in Figure 6.1. The sweep gas flow through the IMO device was driven by a vacuum attached to the gas pathway from the distal manifold. The sweep gas exiting the IMO flows through a moisture trap, gas flow meter, and flow-regulating valve before reaching the

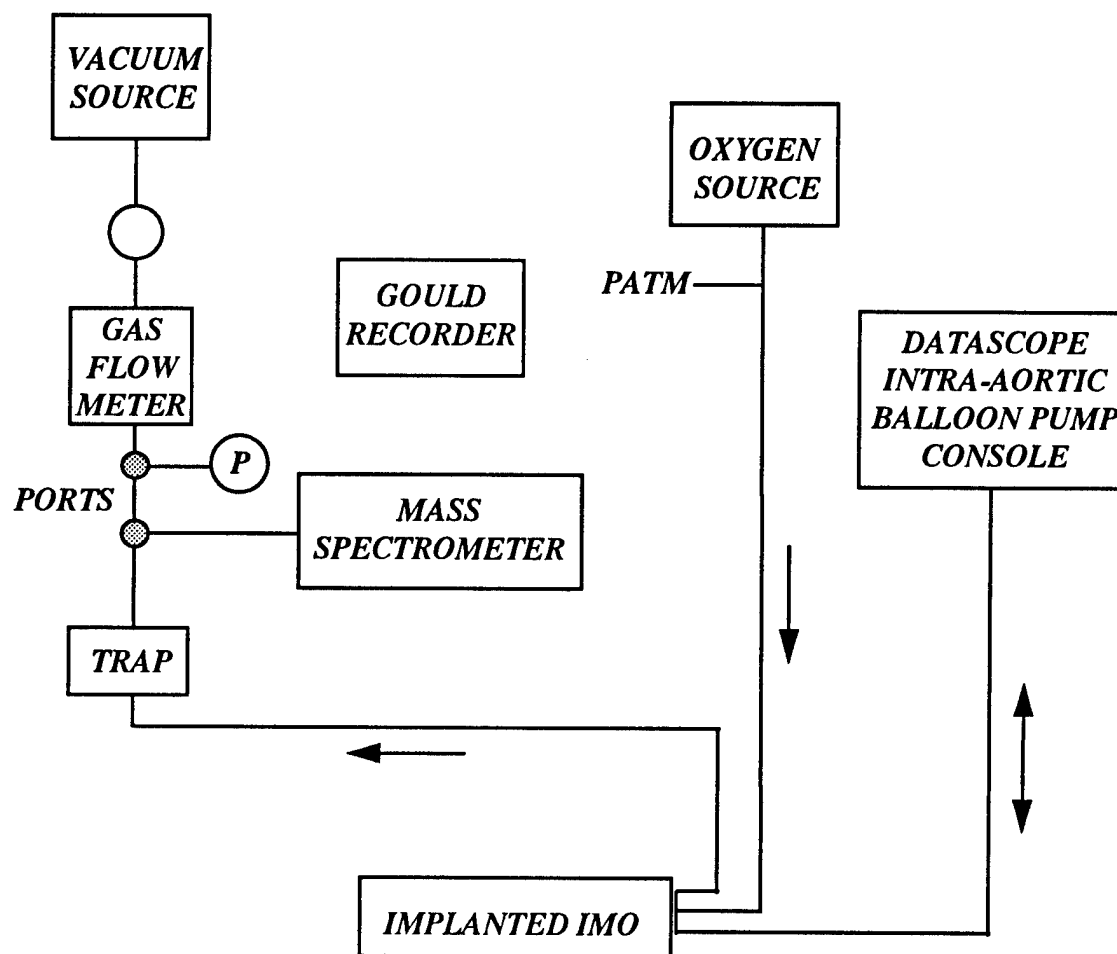


Figure 6.1 Schematic of *In-vivo* experimental setup.

vacuum source. Sample ports after the moisture trap are used for pressure measurement and measurement of effluent gas concentrations by a mass spectrometer (Marquette Electronics, Jupiter, FL) . The sweep gas flowing into the IMO device comes from a 100% oxygen source downregulated to near atmospheric pressure. A third pathway in the IMO device is used to deliver He gas to pulsate the central balloon by means of an intra-aortic balloon pump console (Datascope Corp., Oakland, NJ).

Mass balances for CO₂ and O₂ in the IMO sweep gas pathway (assuming 100% oxygen at the inlet) indicate that their respective exchange rates are given by $V_{CO_2} = Q_{out}F_{CO_2}$ and $V_{O_2} = Q_{in} - Q_{out}F_{O_2}$, where Q represents sweep gas flow rate leaving (Q_{out}) or entering (Q_{in}) the IMO device, and F represents the fractional gas concentration of CO₂ and O₂ measured in the exiting pathway. The sweep gas flow rate is typically much greater than O₂ and CO₂ exchange rates, and hence the difference in Q_{in} and Q_{out} is small. Thus, for simplicity, the O₂ exchange rate is often estimated as $V^*_{O_2} = Q_{out}(1-F_{O_2})$, where the asterisk indicates an estimated value. Combining these O₂ exchange rate expressions, and using the overall mass balance, $Q_{in} - Q_{out} = V_{O_2} - V_{CO_2}$, leads to

$$V_{O_2} = V^*_{O_2} + (V_{O_2} - V_{CO_2}).$$

Accordingly, unless the O₂ and CO₂ exchange rates are exactly balanced, the actual O₂ exchange rate, V_{O_2} , will differ from the estimated one, $V^*_{O_2}$, and the relative difference can be appreciable (the size of CO₂ and O₂ exchange imbalance). The additional measurement of Q_{in} offers no realizable improvement, because both flow meters (Q_{in} and Q_{out}) would need to be accurate and matched down to a flow rate of order $V_{O_2} - V_{CO_2}$, a small flow rate relative to the range of sweep gas flow rates involved. In our study we reduce the sweep gas flow rate (from 3 L/min to < 1 L/min) *during the O₂ exchange measurement only*. Since CO₂ exchange is flow-dependent while that for O₂ is essentially flow-independent, reducing the sweep gas flow rate reduces V_{CO_2} (which at normal sweep gas flow rates usually exceeds V_{O_2}) and helps ensure that the estimated O₂ exchange rate does not represent an *overestimate*. Furthermore, reducing the sweep gas flow rate increases the O₂ concentration difference in the gas stream (in-out) and hence reduces any analysis error associated with computing the difference, $(1-F_{O_2})$.

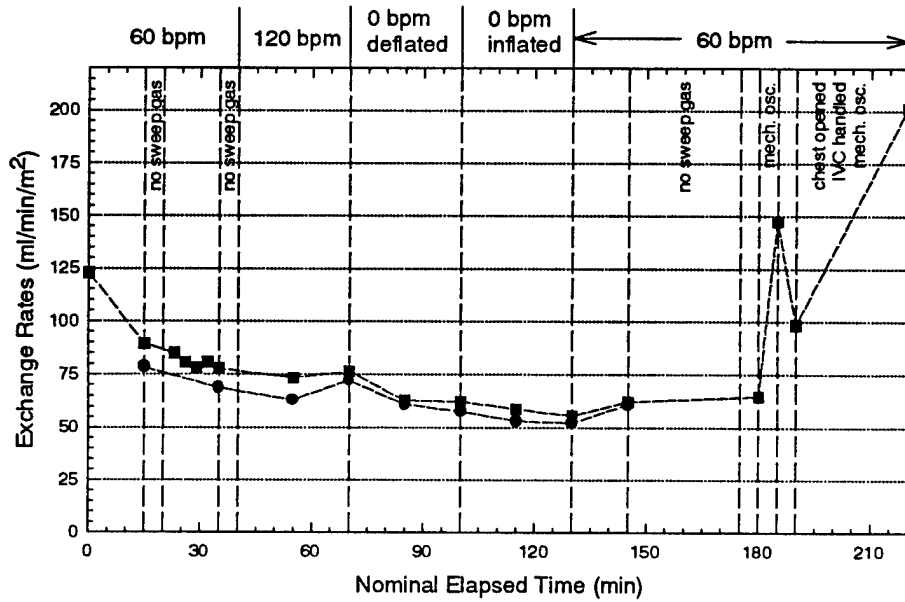
6.2 Acute Animal Experiments

The IMO devices used during animal experiments were all tested *in-vitro* prior to the acute animal studies to ensure proper function and gas exchange performance. The *in-vitro* flow loop and methods were described in Chapter 5. Both free fiber and constrained fiber devices were utilized in these experiments to determine whether the fiber mat configuration significantly improved IMO performance *in-vivo*, as observed during *in-vitro* tests. Oxygen exchange rates of free fiber devices *in-vitro* averaged between 60-80 ml/min/m² in water, with *estimated* exchange rates in blood under similar conditions being about 2.5 fold greater (150-200 ml/min/m²). The recently tested constrained fiber bundle device (D14) exchanged 125 ml/min/m² of oxygen in water which translates to approximately 240-270 ml/min/m² in blood. Maximal gas exchange rates typically occurred at balloon pulsation rates between 60 and 90 bpm in free fiber prototypes and between 150-170 bpm in constrained fiber devices. The differences in the pulsability of these prototypes were described in section 5.6.

Free Fiber Devices In October of 1995 we began acute animal testing of our IMO free fiber prototypes at the D07 level of design (prototype previous to that with the redesigned helium pathway). Five acute animal experiments were performed. The goal of these experiments was to establish the level of gas exchange achievable with our current prototype design and to demonstrate a consistent level of gas exchange with our devices over a period of several hours, as well as determining an effective protocol for animal implants. Some details of the animal tests are summarized in Table 6.1. In all experiments the devices were inserted by surgical cutdown through the external jugular vein into the inferior vena cava of anesthetized calves (as described in the previous section). One of the devices had covalently bound heparin attached to its surfaces using the Carmeda coating process performed by Medtronics Inc. through agreement.

The first two acute animal tests were of relatively short duration and the gas exchange performance realized during the experiments is shown in Figure 6.2. In both cases the gas exchange performance of the IMO prototypes declined markedly such that gas exchange was only about one-half the starting exchange level after just two hours. Some transient return of gas exchange was achieved at the end of these experiments by mechanically oscillating the fibers of the device *in-situ*. Removal of the device at the end of the experiment showed problems with

D07-1 Animal Experiment 10/17/95



D07-2 Animal Experiment 11/02/95

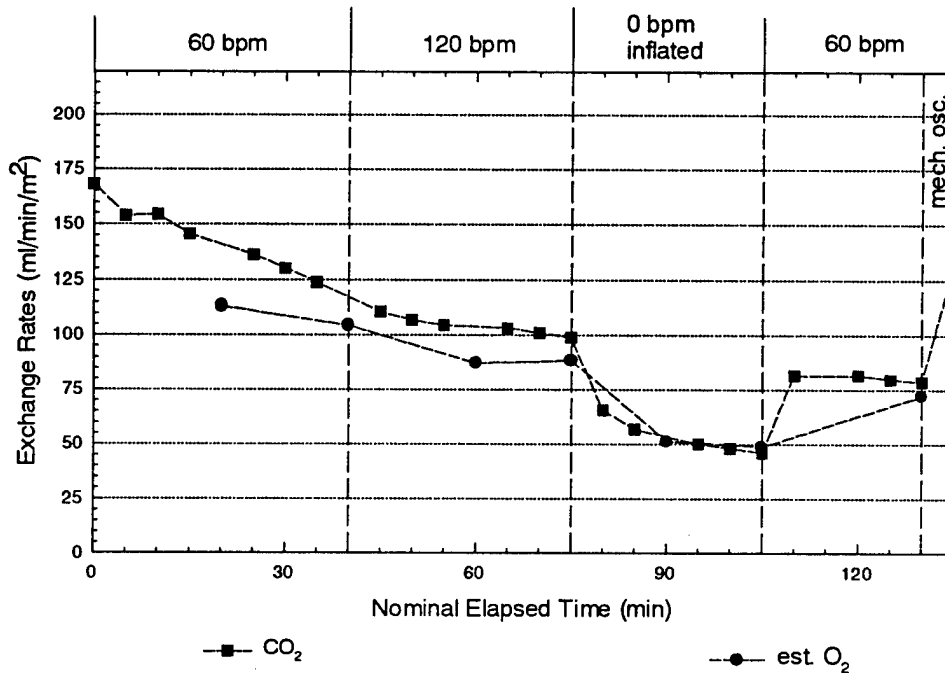


Figure 6.2 Gas exchange performance of IMO prototypes in first two acute animal experiments.

thrombus mediated clumping of the fibers. The clumping was extensive enough that loss of functional surface area for exchange occurred, which led presumably to the reduction in gas

Table 6.1: Summary of First Series of Acute In-Vivo IMO Tests				
Test Date	Prototype Used	Membrane Area (cm ²)	Animal	Duration
10-17-95	D07.1	1334	68 kg female calf	3.7 hours
11-02-95	D07.2	1356	72 kg female calf	2.3 hours
11-17-95	D07.4	1379	65 kg female calf	6 hours
11-30-95	D07.6	1356	80 kg female calf	5.8 hours
12-07-95	D07.3 (Carmeda)	1311	61 kg female calf	6.6 hours

exchange measured. The decision for subsequent animal experiments was to shift to a more aggressive anti-coagulation regimen consisting of an initial heparin dose of 400 units/kg followed by intravenous infusion of heparin at a rate of 50-100 units/kg/hour so as to maintain activated clotting times in excess of 400 sec. The measured gas exchange performance in the next two acute experiments, following the more aggressive anti-coagulation regimen, is displayed in Figure 6.3. Here, gas exchange rates are relatively constant over several hours except for a decreased rate during the static (no balloon pulsation) control period. Respiratory challenges were implemented at the end of the experiments by decreasing the mechanical ventilation rate of the animal. In both cases the IMO devices responded appropriately, compensating for the ventilatory challenge by increasing gas exchange rates.

The final acute animal experiment using a free fiber device involved the more aggressive anti-coagulation regimen and an IMO device which was heparin coated using the covalent attachment Carmeda coating process (Medtronic Inc.). The static control period (no balloon pulsation) was eliminated from the protocol because our previous results consistently indicated some permanent loss of gas exchange capacity during this period without pulsation, which was not recovered when balloon pulsation re-commenced (see Figures 6.2 and 6.3). We attributed this

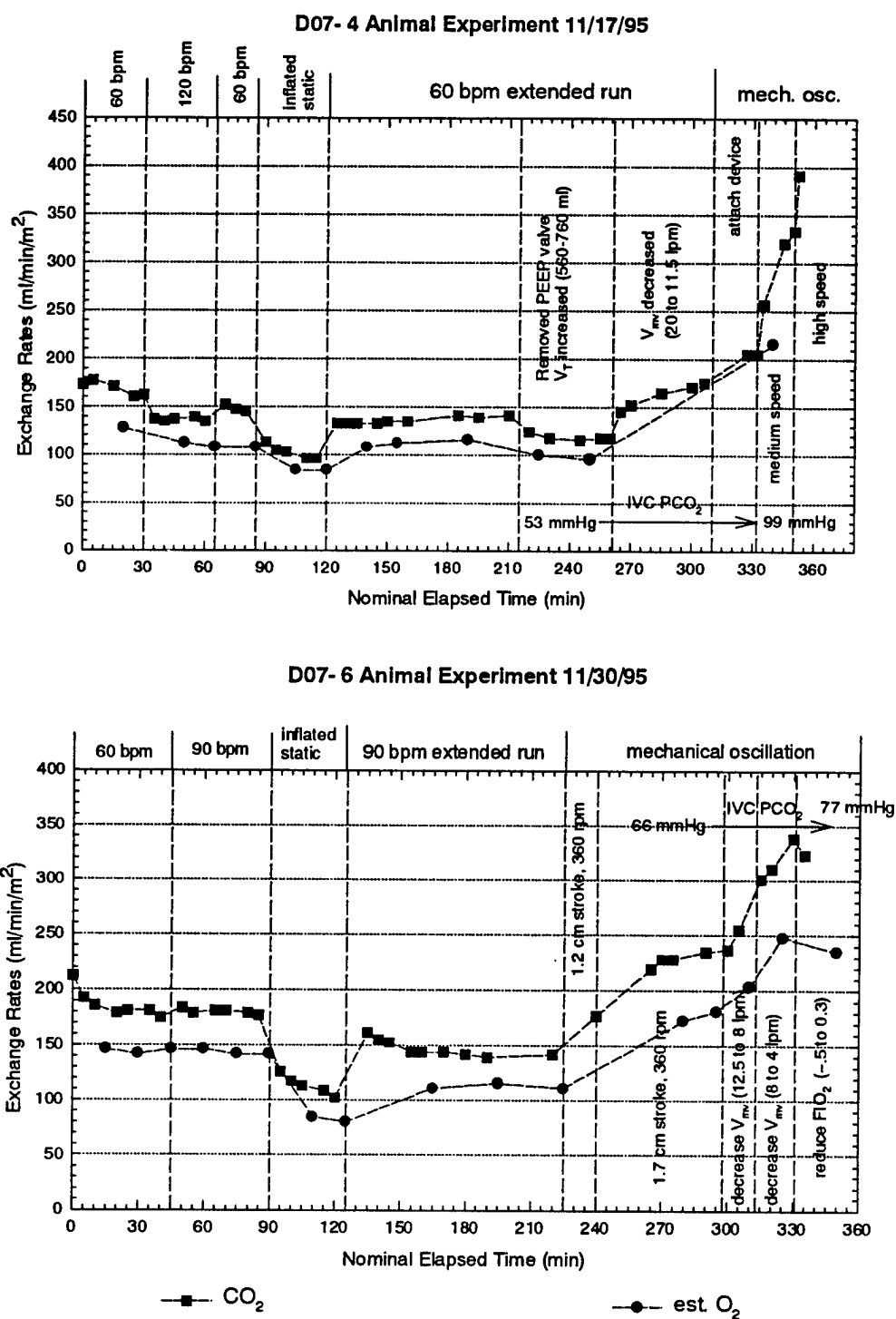


Figure 6.3 Gas exchange performance in acute animal experiments with continuous heparin infusion.

to the initiation of some thrombus formation within the fiber bundle during the stasis period, which aggregated fibers sufficiently to reduce effective gas exchange surface area. The gas exchange performance of the free fiber IMO device in this last acute experiment is shown in Figure 6.4. Although the rates of gas exchange with the device began somewhat lower than our previous two experiments, there was no decline in gas exchange over the extended pulsation period. Thus, in the last three animal experiments the rates of gas exchange during extended balloon pulsation were comparable, being between 100 and 150 ml/min/m² for both O₂ and CO₂. At the end of the experiment but before implementing the ventilatory challenge, we also examined the effect of mechanical oscillation of the fibers as a supplement to balloon pulsation. Mechanical oscillation resulted in improvements to gas exchange of 30-40%, but required oscillation rates of 4 to 6 Hz, substantially above the rates associated with balloon pulsation, and led to significant red blood cell hemolysis.

Figure 6.5 summarizes representative sustained exchange rates found in the last three acute experiments as well as the acute phases of two chronic implants (D07 and D08, details in the next section). Only results from the last five D07 animal tests are included, as the first two acute experiments involved establishing the anti-coagulation regimen and balloon pulsation protocols, and the gas exchange rates were not representative of their *in-vitro* performance. As described previously, the *estimated gas exchange in blood under otherwise comparable conditions is about twice that measured in water*. The D07 *in-vitro* characterization tests performed prior to implantation suggest that O₂ exchange rates in blood for these prototypes should range from approximately 120 to 160 ml/min/m², assuming all else the same (i.e. flowrate range, size of vessel relative to IMO device size). Oxygen exchange rates achieved during the first two acute experiments began at 125 ml/min/m² but quickly dropped and remained between 50-75 ml/min/m² due to the insubstantial anti-coagulation regimen. During the last five D07 tests, however, the maximal sustained CO₂ exchange rate was 185 ml/min/m² and maximal sustained O₂ exchange rate was 140 ml/min/m². Figure 6.6 explains that exchange rates increased 30-35% upon awakening the animal. There was, however, approximately a 10-15% decline in both CO₂ and O₂ exchange rates with the IMO devices which were heparin-coated (D07-3, D07-7, D07-8).

Manipulation of experimental parameters such as increasing balloon pulsation and decreasing

D07- 3 Animal Experiment 12/07/95

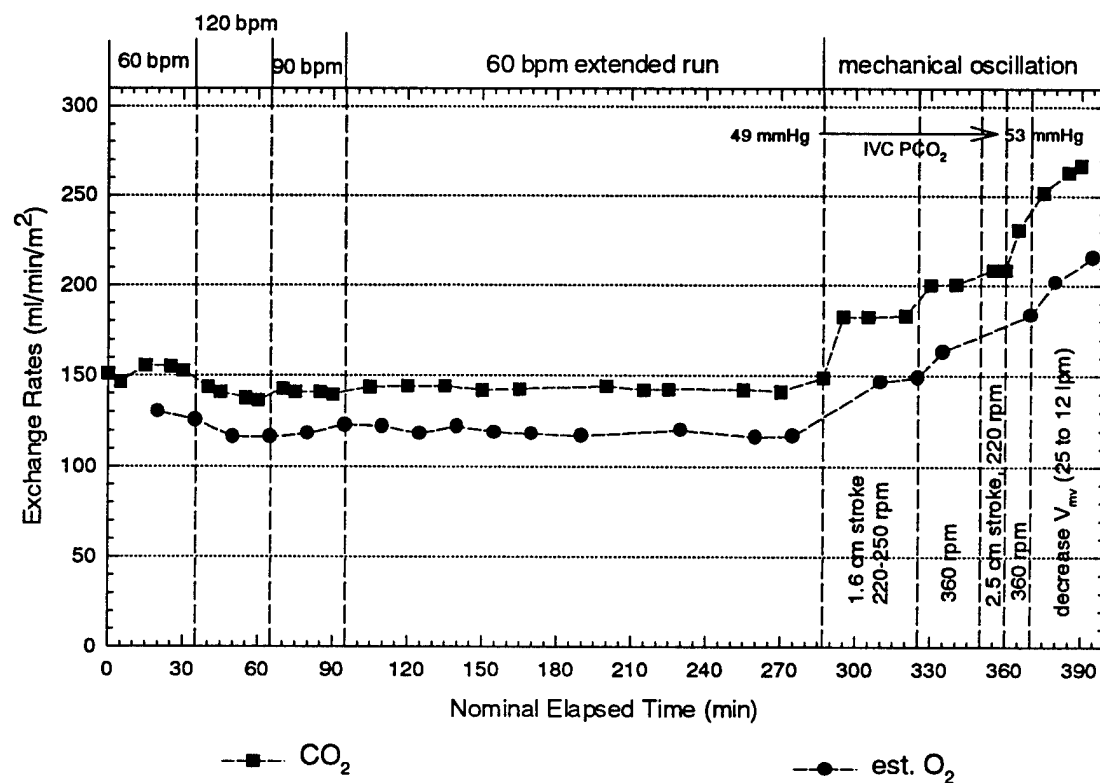


Figure 6.4 Gas exchange performance in acute animal experiment using Carmeda coated IMO device.

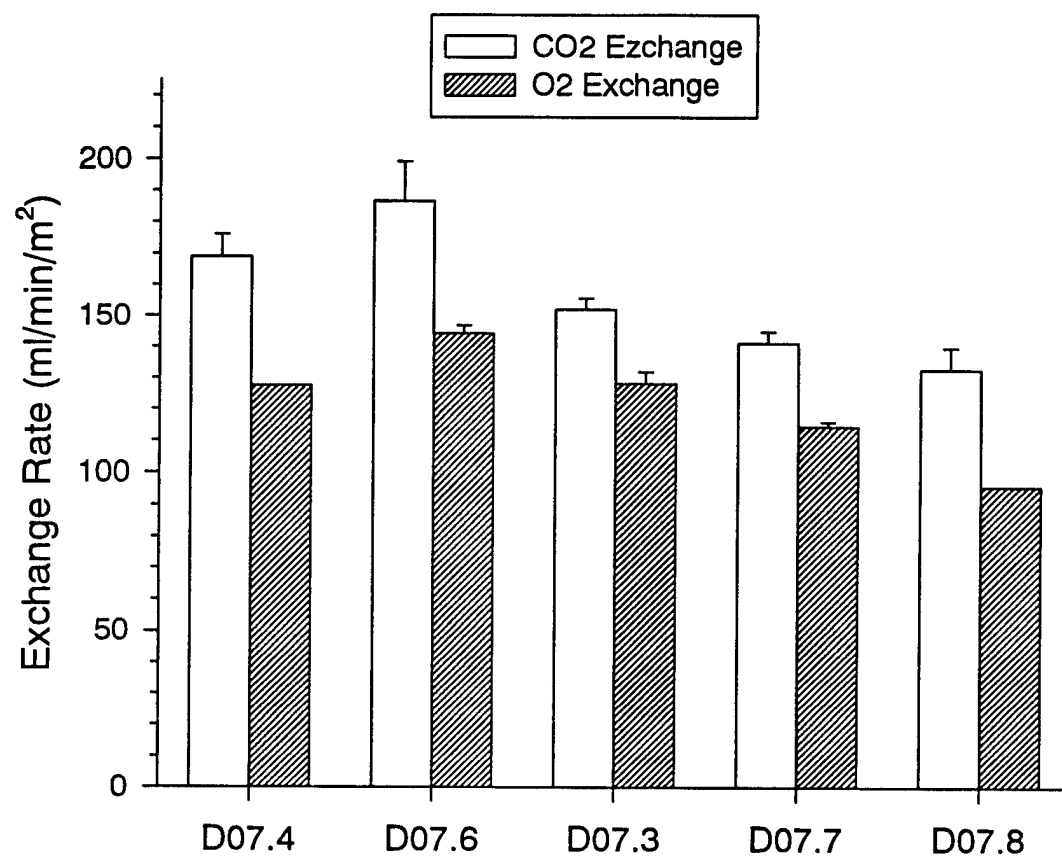


Figure 6.5 Summary of initial gas exchange rate in acute animal implants.

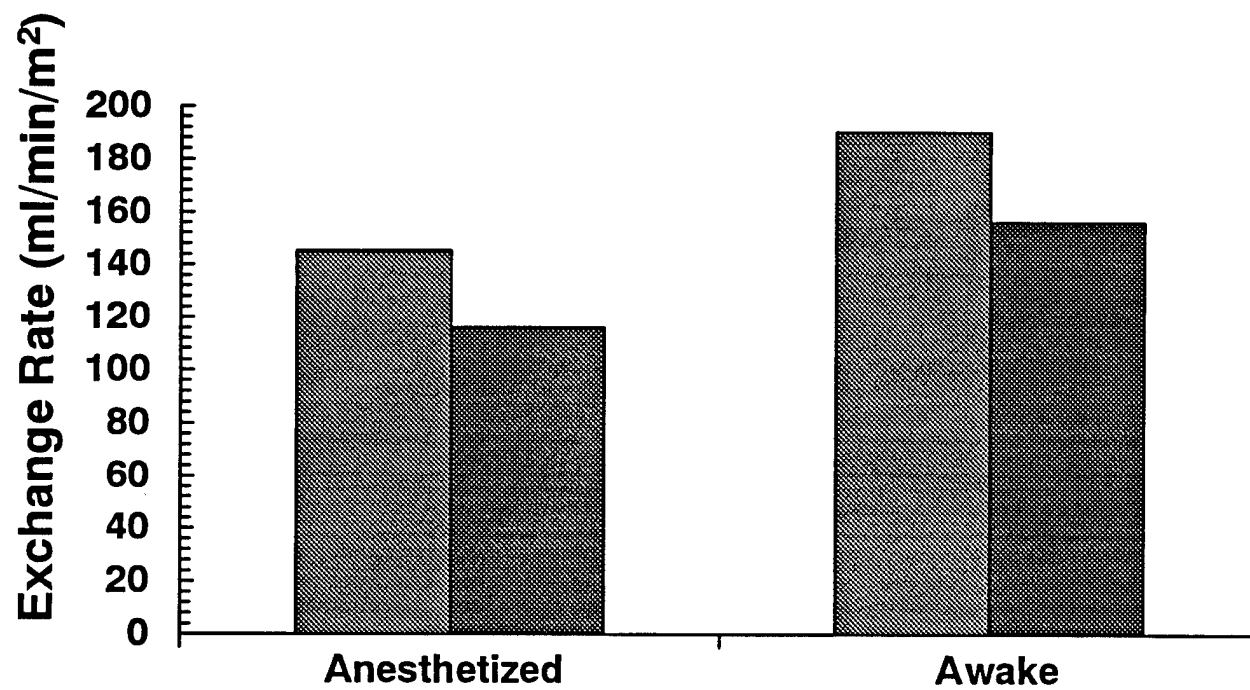


Figure 6.6 Gas exchange comparison of anesthetized versus awake animals during series D07 *in-vivo* animal experiments.

minute ventilation, enhanced gas exchange as predicted following extensive *in-vitro* tests. Balloon pulsation had a significant effect upon exchange rates, which increased by 50% with balloon pulsation, consistent with *in-vitro* testing (Figure 6.7). When ventilatory challenge (50% reduction in minute ventilation) was introduced, the IMO devices responded appropriately. Figure 6.8 depicts the typical change in exchange rates observed with ventilator challenge during 60 bpm balloon pulsation. IVC and CVP $p\text{CO}_2$ increased from 53 to 82 mmHg, and 51 to 75 mmHg, respectively. As a result, the CO_2 exchange rate increased markedly from 120 to 180 ml/min/m² (50%).

The IMO devices tested were scaled down prototypes with surface areas of approximately 0.14 m², or three fold to four-fold less than we estimate is ultimately compatible with human vena caval placement. Accordingly, the IMO devices were not expected to impact significantly on the blood gas levels of the animals (but would respond appropriately to them, as in the ventilatory challenge described above.) Arterial O_2 and CO_2 tensions were altered moderately during the course of the studies. Mean arterial $p\text{O}_2$ and $p\text{CO}_2$ during the D07-3 experiment, for example, were 280 ± 14 mmHg (base 212 mmHg) and 40 ± 0.3 mmHg (base 38 mmHg), respectively. During balloon pulsation, venous $p\text{CO}_2$ was diminished, particularly at the central venous location. For example, IVC and CVP $p\text{CO}_2$ were 42 ± 2 mmHg (base 42 mmHg) and 39 ± 1 mmHg (base 43 mmHg), respectively. Conversely, the IVC and CVP $p\text{O}_2$ rose slightly above their baseline values, 57 ± 4 (base 44 mmHg) and 80 ± 3 mmHg (base 59 mmHg), respectively. The hemodynamic response to the IMO device within the vena cava was found to be minimal despite prolonged periods of balloon pulsation. Figure 6.9 demonstrates the changes in mean arterial pressure, pulmonary artery pressure, CVP, and IVC pressure during the course of a representative five hour study (D07-3). Heart rate was stable at 103 ± 2 bpm (base 105 bpm), the mean arterial pressure was 97 ± 2 mmHg (base 96 mmHg), the pulmonary artery pressure remained at 31 ± 1 mmHg (base 22 mmHg), the CVP was 9 ± 1 mmHg (base 10 mmHg), and the intravena cava pressure measured 21 ± 1 mmHg (base 12 mmHg). The cardiac output remained quite stable at 7.1 ± 0.2 L/min (base 7.2 L/min), however in several experiments, a significant decrease to 5.8 L/min. occurred after increasing the balloon pulsation rate to 90 bpm due to the increased pressure in the system. The pressure drop across the IMO was measured to be

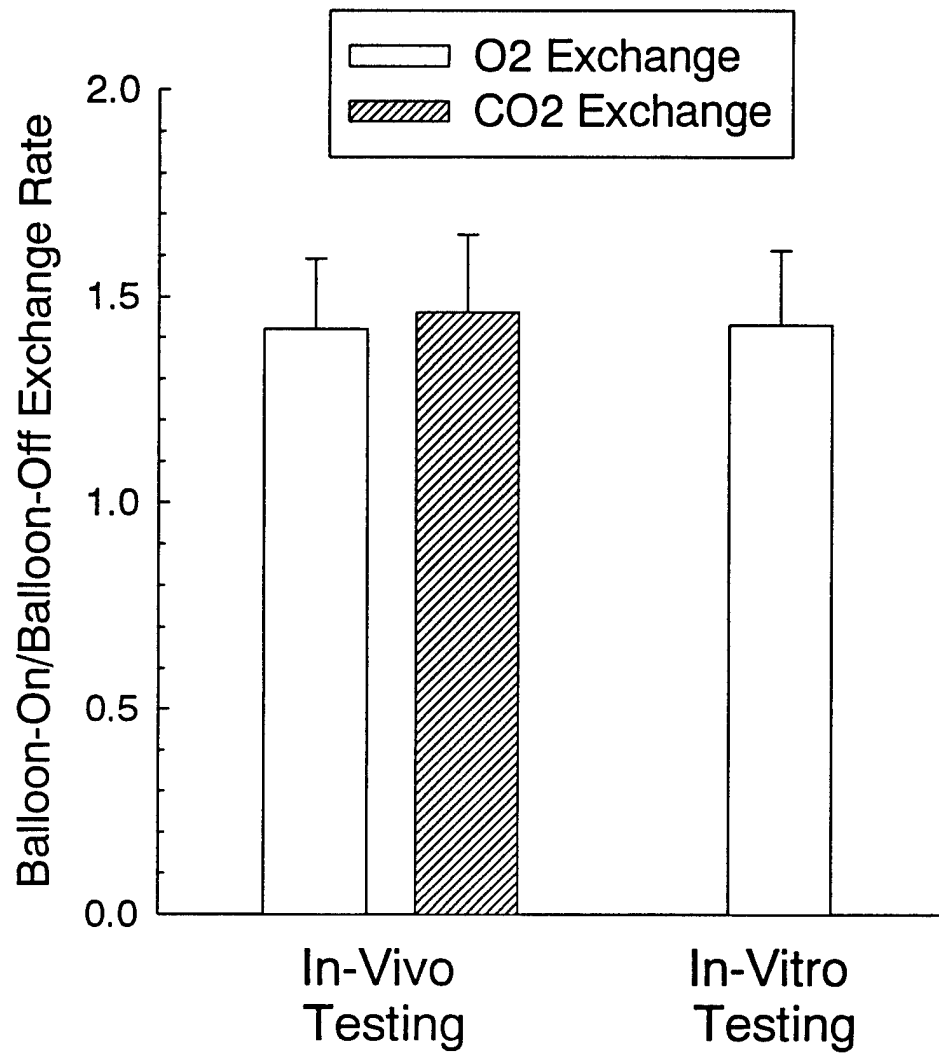
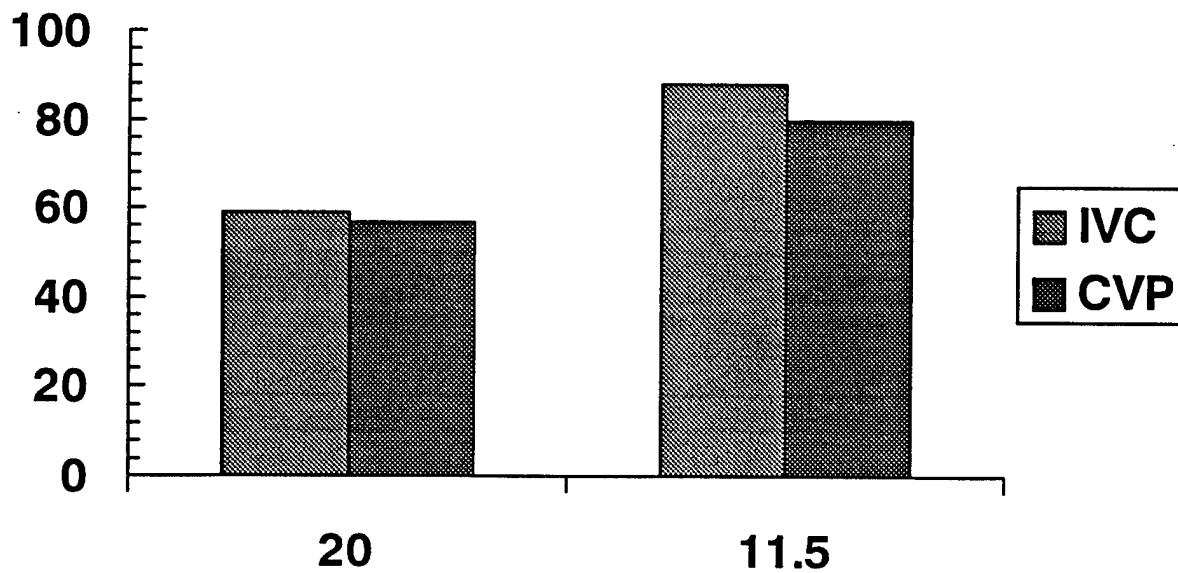


Figure 6.7 Effects of balloon pulsation *in-vivo* vs. *in-vitro*.

A IVC, CVP venous $p\text{CO}_2$ (60 bpm)



B. IMO VCO_2 (60 bpm)

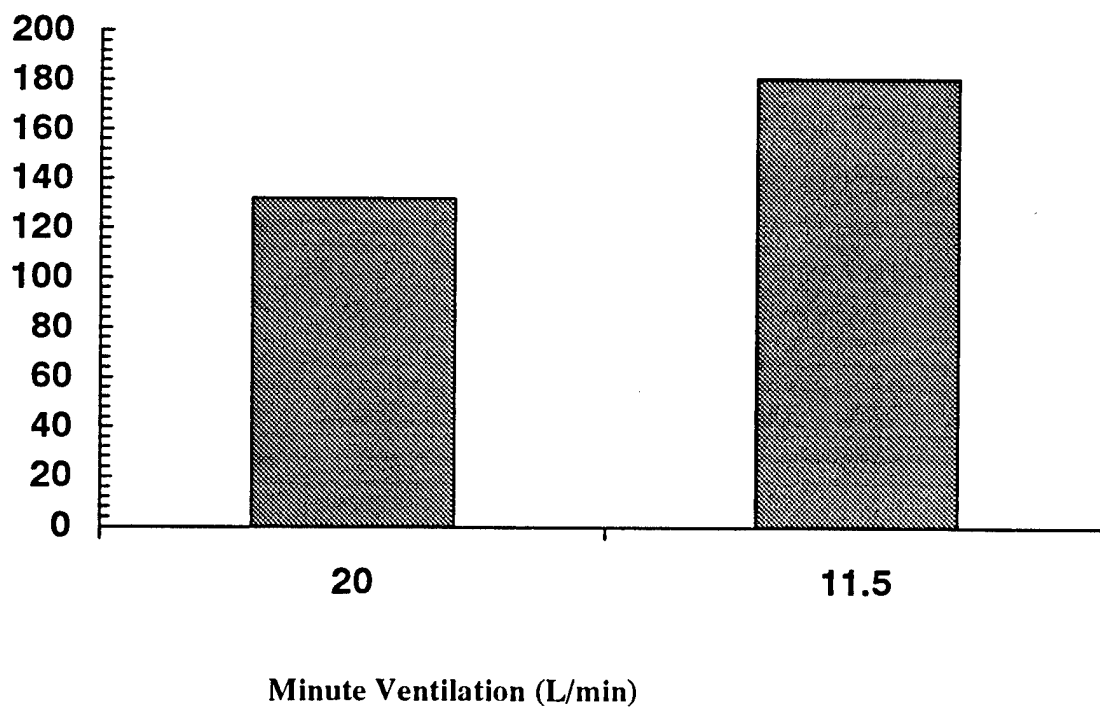


Figure 6.8 Effects of ventilatory challenge on gas exchange *in-vivo*.

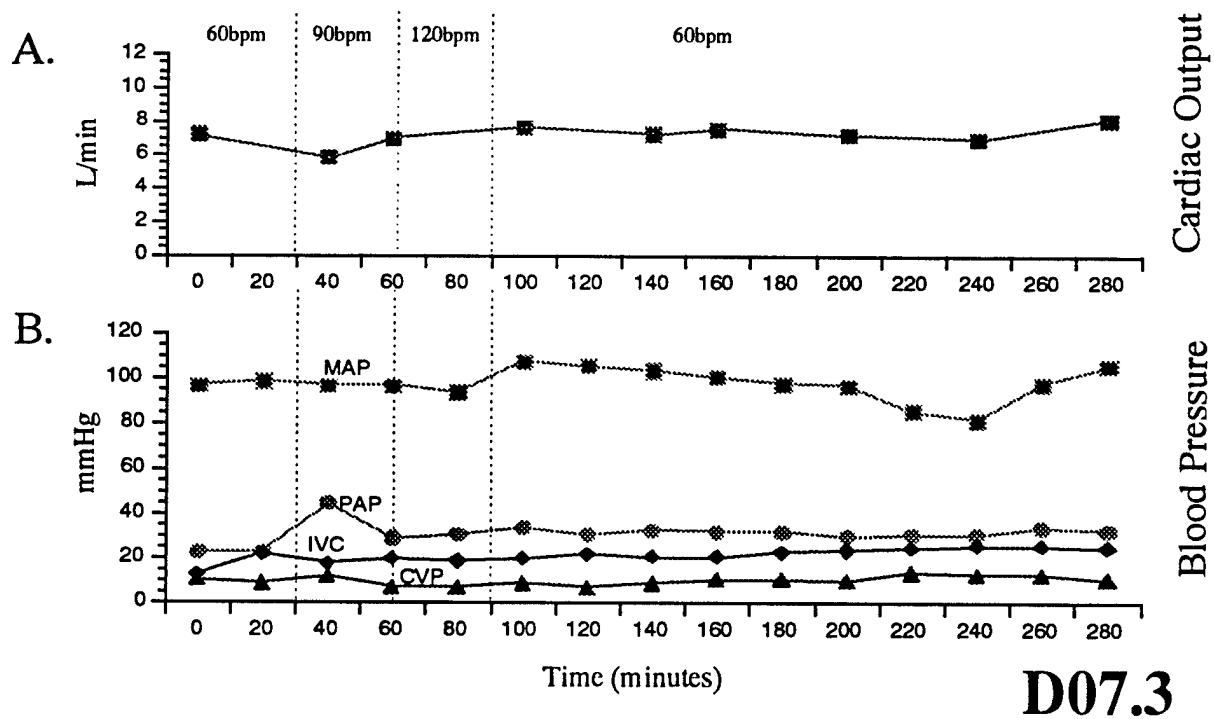


Figure 6.9 Animal hemodynamics during acute implantation of IMO device.

approximately 12.1 ± 0.6 mmHg *in-vivo*, as compared to 2.0 mmHg, the average *in-vitro* pressure drop across the device.

The plasma free hemoglobin levels reached a maximum of 41.5 mg% at four hours in one experiment. Average at baseline, 1, 4, and 6 hour levels are shown in Figure 6.10. After euthanization, necropsy revealed no organ pathology, nor was there evidence of thrombo-embolus in the lungs or other organs. Upon removal of the IMO, in two instances, the fibers of the IMO device were partially kinked, suggesting that the device may have been too large or that it fit awkwardly into the vena cava, however no vena caval injuries were identified. No significant thrombosis was observed on the devices upon inspection, eliminating the results of the first two experiments which lacked substantial anti-coagulation.

Constrained Fiber Devices Previously (section 5.6), we described the superior gas exchange achieved *in-vitro* with the constrained fiber prototypes. Figure 5.13 shows oxygen exchange rates of constrained fiber prototypes and one free fiber device (D08), for comparison purposes, in the mock vena cava test section. Whereas the free fiber device exhibited a plateau of gas exchange rate with increasing balloon pulsation rate, the rate of exchange in the constrained fiber prototypes continually increased with pulsation rate. Figure 6.11 displays the gas exchange rates acquired *in-vivo* by the D14 prototype as compared to the best of D07 acute implants (D07.6). The constrained fiber prototype doubled the gas exchange rates achieved in the D07 free fiber devices previously tested. The device achieved a maximum O₂ delivery rate of 336 ml/min/m² and a CO₂ removal rate of 402 ml/min/m² at 150 bpm. These results confirmed what the *in-vitro* experiments initially determined, that the constrained fiber prototypes gas exchange levels are well within our target range. The superior exchange rates can be attributed to the constrained fiber bundles because the prototypes are otherwise identical and have comparable balloon pulsation dynamics as determined in independent tests. The key to the success of these prototypes is their uniformly spaced fibers, which eliminate preferential pathways for flow. Free fiber devices exhibit a plateau effect because their fiber orientation and disposition relative to the bulk flow and to the central balloon creates these preferential channels that allow blood to bypass the bundle without being oxygenated. Constrained fiber bundles eliminate these pathways and

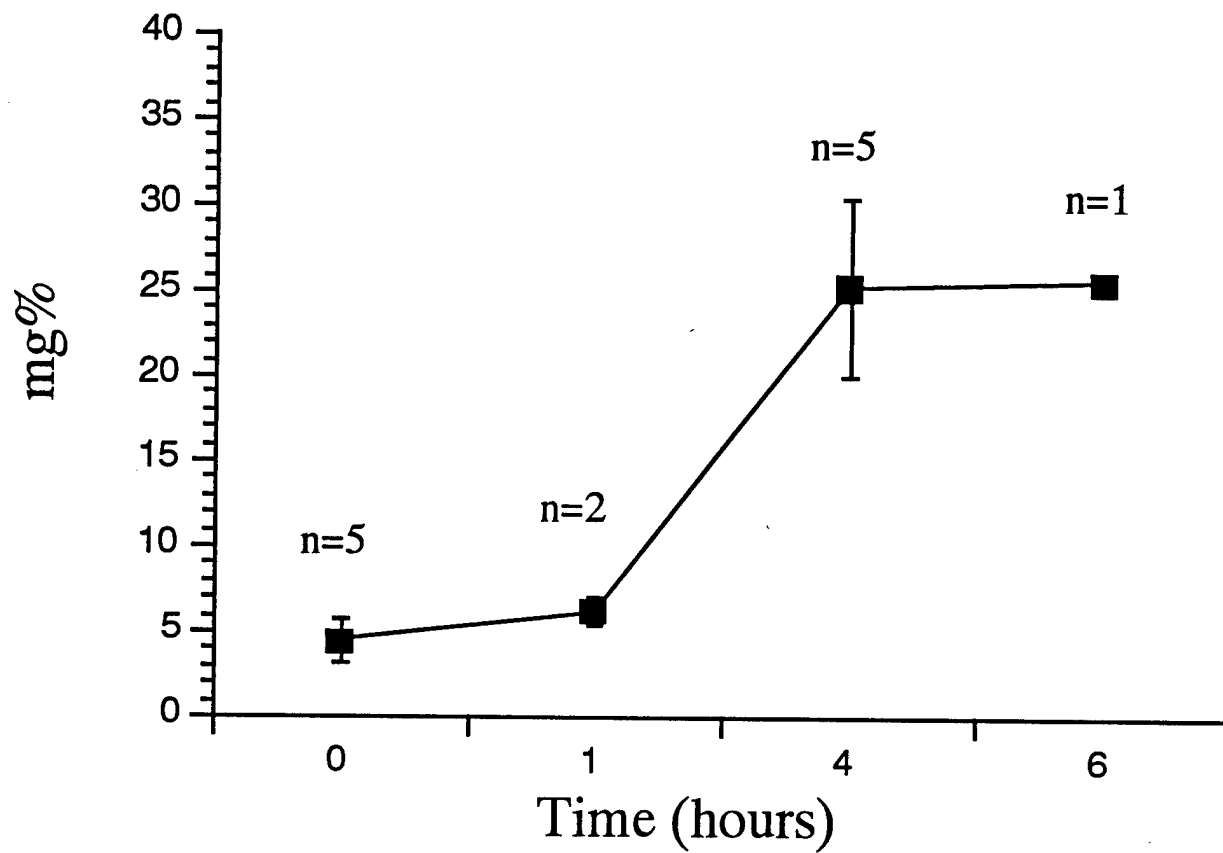


Figure 6.10. Plasma free hemoglobin during acute animal implant.

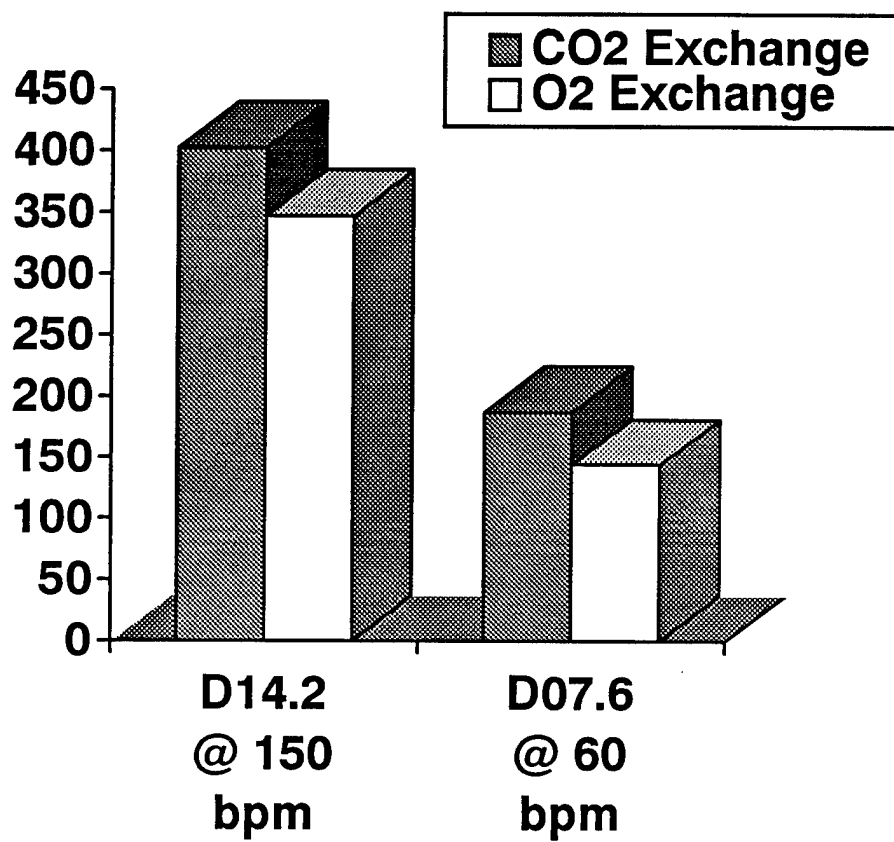


Figure 6.11 Acute In-Vivo Exchange Rates of Constrained Fiber Device D14.2 vs. Free Fiber Device D07.6.

therefore gas exchange continues to increase with balloon pulsation to much higher levels (160 bpm). *In-vitro* tests of the constrained fiber prototypes showed levels of gas exchange within or close to our design target range (128 ml/min/m² @ 169 bpm), indicated within the pair of upper dashed lines in figure 5.13, thus prototype D14 underwent *in-vivo* testing.

6.3 Chronic Animal Implantation Studies

Following the success of the acute experiments, attention was directed to longer term animal tests for examining biocompatibility issues and consistency of gas exchange levels over a 48 to 72 hour time frame. The prototypes tested in this group of experiments were heparin coated in anticipation of the blood-surface interactions reducing gas exchange capabilities. The D07 devices were heparin coated (Carmeda process) at Medtronic after the fibers were already potted and the device was assembled, whereas the D09 prototype incorporated KPF 190 fibers which underwent thrombo resistant coating prior to potting the fibers and assembling the device.

Free Fiber Devices Three free fiber chronic experiments were performed during the contract period, two devices from the D07 series and one from the D09 series. A summary of gas exchange results for the D07 series experiments is shown in Figure 6.12. In both experiments the gas exchange performance of the IMO prototypes began at levels consistent with those accomplished in the acute experiments. O₂ gas exchange began at 130 and 140 ml/min/m², while CO₂ exchange began at 160 to 180 ml/min/m². The levels of gas exchange were reasonably consistent in the first four to eight hours of the chronic time course, but subsequently began to gradually diminish during the rest of the chronic experiment. Ultimately gas exchange diminished in both experiments to levels between 2/3 and 1/2 of initial gas exchange rates. We believe that this behavior can be attributed to some fibrin clot formation which began at the fiber manifold ends where the fibers are closely packed together for potting. The fiber bundles used for the chronic experiments underwent the Carmeda (anticoagulant) heparin coating process, but the Carmeda coating was done on the fiber bundles after they were potted into IMO prototypes. Accordingly, we suspect that the heparin coating may not have been applied uniformly or completely to the fiber surfaces at these manifold sites, and that fibrin clotting which started at these sites spread further down the fiber bundle and began aggregating hollow fibers together,

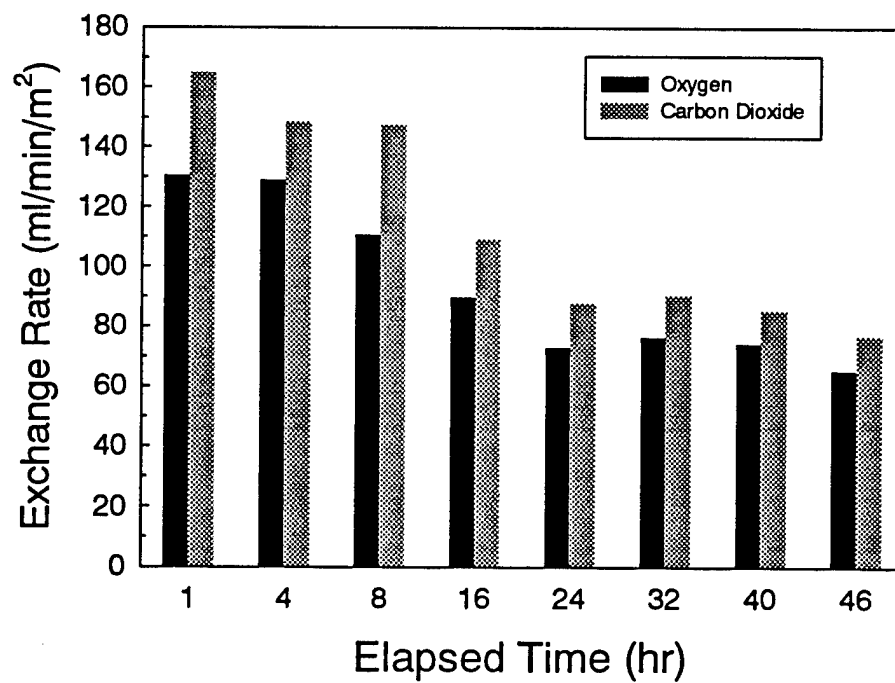
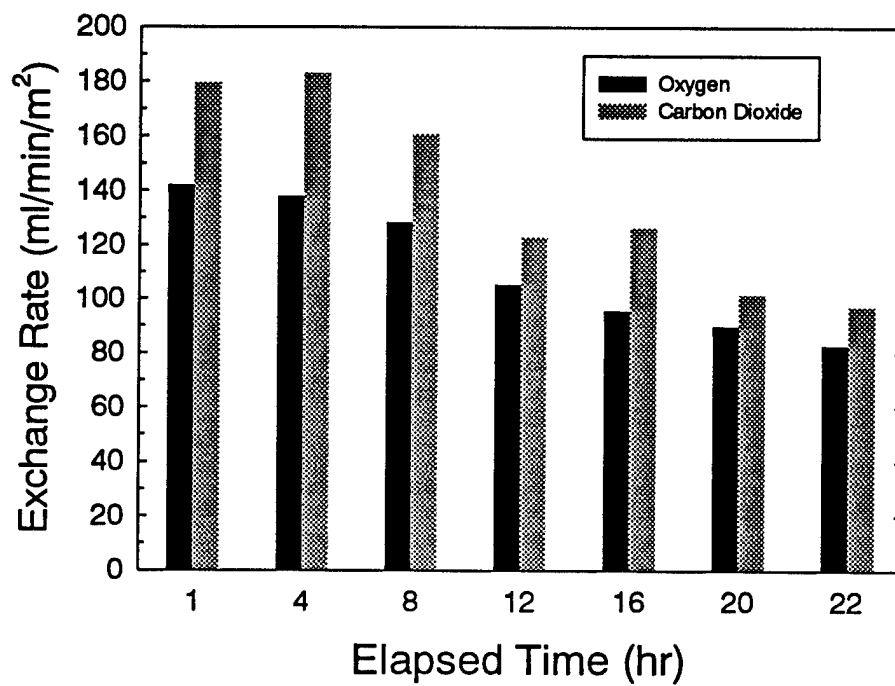


Figure 6.12 Gas exchange during chronic implantation of IMO devices in D07 series.

leading to fiber clumping. This essentially reduced the effective area for gas exchange, resulting in the gradual diminishment of gas exchange during the chronic time course. The appearance of the IMO prototypes at explant was consistent with this hypothesis as thrombus formation was clearly evident at the manifolds and had also spread to the central portion of the fiber bundle.

Subsequently, we repeated a chronic IMO implantation with a D series device fabricated from silicone-coated hollow fiber membranes (D09 series). These hollow fibers were KPF190 porous fibers which underwent the TRC 4.0 (Thrombo Resistant Coating, Surface Engineering Technologies, Salt Lake City, UT) process of a siloxane coating (approximately 1 micron contiguous coating) for nonwetting attributes and covalently-bound heparin coating for antithrombogenicity (using a proprietary, non-Carmeda process). The coating process is done at the fiber level thus ensuring that the heparin coating exists on fiber elements even at the manifold sites. The gas exchange performance of the D09 device during the chronic implantation is shown in Figure 6.13. The initial levels of gas exchange for both O₂ and CO₂ began below the initial levels in the previous chronic implants. This can most likely be attributed to differences in the size and number of hollow fibers fabricated into the fiber bundles of these devices. The D07 devices used in the previous chronic implants had 720 fibers of 240 microns inner diameter. The D09 device used in the current chronic implant had 1008 fibers of 190 microns inner diameter. The gas exchange rates reported for these chronic experiments are normalized to the surface areas of the fiber bundles. Our experience is that gas exchange per unit area in a fiber bundle decreases with increasing number of fibers in the bundle (decreasing fiber size), most likely due to interaction in diffusional fields around fibers. That the initial exchange rates per unit surface area in the D09 experiment are 20-30% smaller than in the D07 experiments was consistent with their respective exchange performance during *in-vitro* characterization testing.

The most significant finding in the chronic implantation of the D09 device (Figure 6.13) was that the continual degradation in gas exchange over the chronic time course was appreciably attenuated compared to the D07 devices (Figure 6.14). The time course of the D09 implantation was a full three days compared to 1 day (D07.7) and 2 days (D07.8) in the D07 implantations. Nevertheless, the ratio of final to initial gas exchange rate is markedly greater in the D09 implantation than in either of the D07 implantations. On necropsy, the D09 device showed similar thrombus formation at manifold sites and similar thrombus mediated fiber clumping as the D07

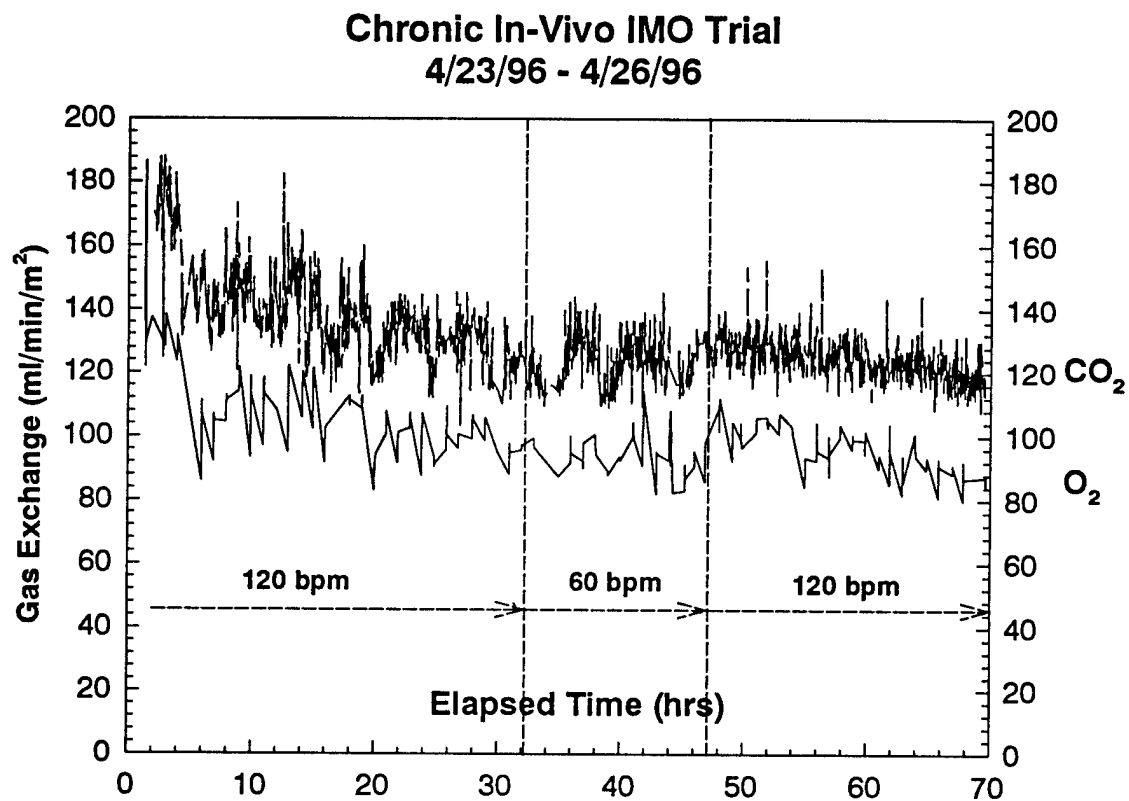


Figure 6.13 Gas exchange during chronic implantation of IMO device with silicone coated fibers.

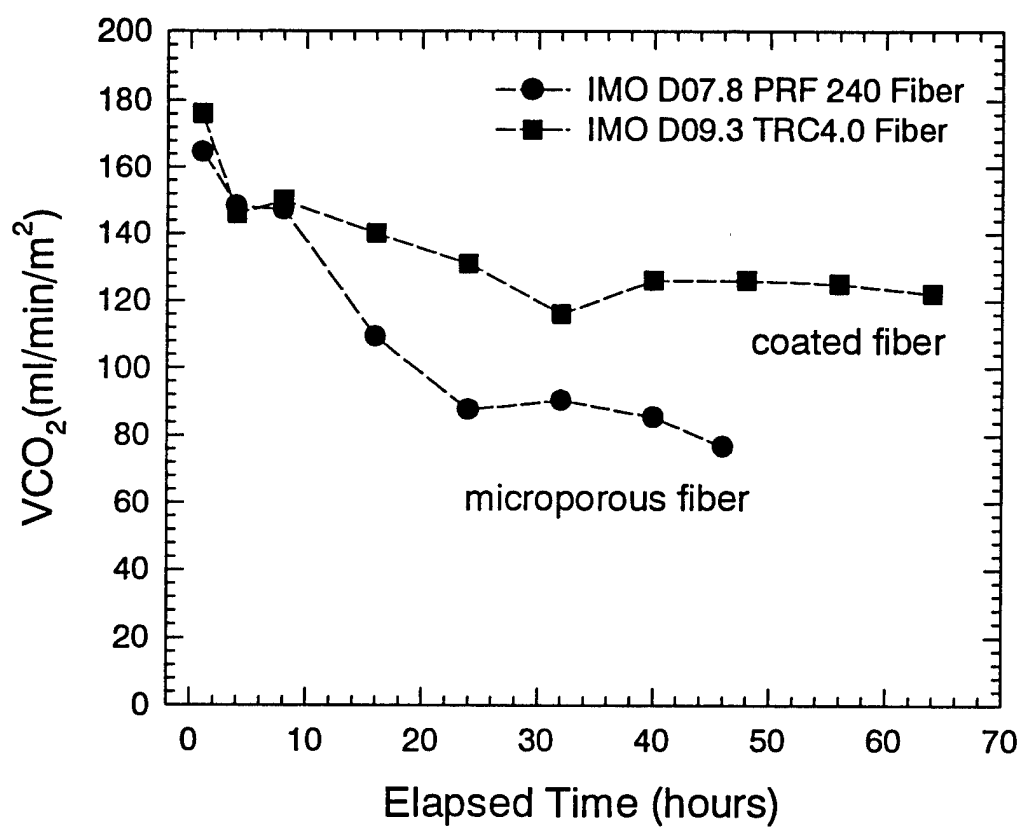


Figure 6.14 Comparison of gas exchange over time of the silicone coated fiber D09.3 vs. a regular microporous fiber prototype D07.8.

devices at necropsy. Thus, the continual reduction in gas exchange in the D07 implantation may be due to fluid infiltration (wetting) into the pores of the hollow fibers, rather than thrombus related degradation as was originally hypothesized. The fibers in the D09 device are siloxane coated and hence much less susceptible to degradation associated with fluid infiltration into fiber pores. Further work has begun examining the issue of gas exchange degradation due to extended fiber exposure to blood. We have begun work with Bend Research (Bend, Oregon) on developing the optimal coating for IMO hollow fibers to be used in our device. The goal of Bend Research is to develop a new coating process specifically for the needs of the IMO. Selecting and/or synthesizing coating materials and processes for the IMO has begun both at Bend and Pittsburgh. Materials investigated will be screened for biocompatibility and oxygen permeability, and their coating properties (solution properties, support wetting, and support adhesion) must also be examined. Also planned is the construction of a lab scale coating machine once the best coating process is identified.

6.4 Implications of *In-Vivo* vs. *In-Vitro* Testing

The acute *in-vivo* tests of D14 suggested key differences between the performance of the IMO *in-vitro* as compared to its behavior *in-vivo*. Primarily, the gas exchange rate was independent of balloon pulsation *in-vivo* (Figure 6.15) compared to the large effect of balloon pulsation demonstrated *in-vitro*. (refer to figure 5.12). *In-vitro*, balloon pulsation increased oxygen delivery by 250% whereas gas exchange rates were independent of balloon pulsation during implants. Gas exchange rates achieved during the *in-vivo* trial, however, were actually beyond our target gas exchange rate of 280 ml/min/m² and reached levels of approximately 330-340 ml/min/m² regardless of the balloon pulsation rate. Another interesting aspect of the *in-vivo* testing was that the pressure drop across the length of the device was found to be 9-16 mm Hg *in-vivo*, while *in-vitro* measurements showed less than 1 mm Hg pressure drop in a 1" test section.

The behavior exhibited *in-vivo* as compared to that expected based on standard *in-vitro* characterization tests suggested that the mean flow velocity *in-vivo*, i.e. the flow rate divided by the cross sectional area, was much higher than that encountered *in-vitro*. During *in-vitro* testing,

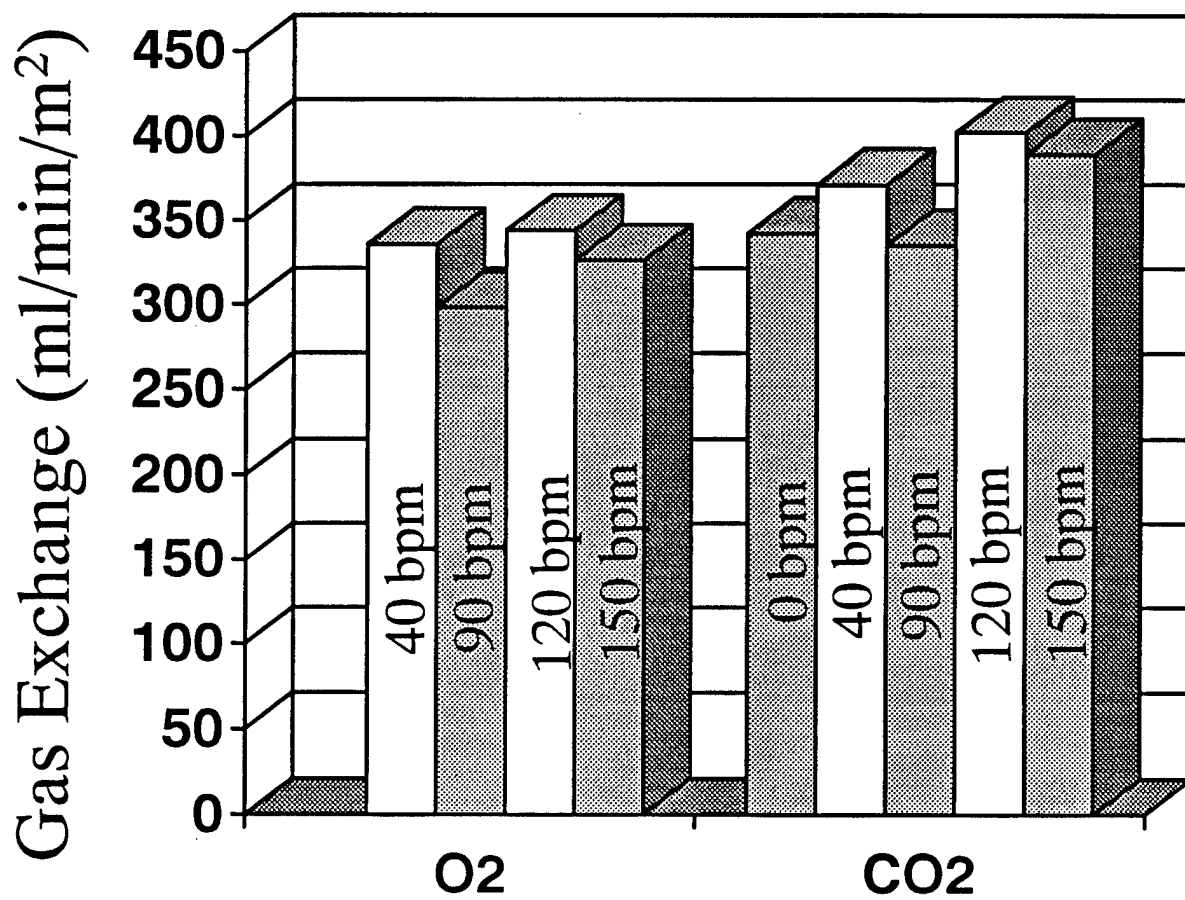


Figure 6.15 *In-Vivo* gas exchange performance of the D14 prototype. The exchange rates appear independent of the balloon pulsation frequency.

water was pumped through a test section of 1" inner diameter at a flow rate of 3 L/min to approximate projected conditions in a human IMO recipient. In a calf, typical cardiac outputs are 7-10 L/min, suggesting that the flow rate in the inferior vena cava, where the device is positioned for the *in-vivo* testing protocol, was approximately 4.5- 6.5 L/min. The decreased flow rate in the IVC is due to the fact that approximately 2/3 of the calf's blood volume returns to the heart via the inferior vena cava and the other portion through the superior vena cava thereby decreasing the liters of blood flowing through the IVC per minute. Also contributing to the high mean blood velocity is the small diameter of the vena cava. By opening the chest cavity of the calf with the device implanted, the diameter of the vena cava appeared to be approximately 3/4", by visual inspection. The pressure drop differences across the device *in-vivo* (9-16 mm Hg) compared to *in-vitro* measurements (1 mm Hg) supports evidence that the inner diameter of the vena cava was less than 1".

The high blood flow rate and small vessel diameter in the calf implantations may contribute to a much higher mean flow velocity past the IMO device than that achieved *in-vitro*. This would result in an increased baseline gas exchange rate, even in the absence of balloon pulsations. Accordingly, the transverse velocity component, imparted by the balloon may contribute very little to the total gas exchange when compared to the contribution of the significant longitudinal component and gas exchange would appear to be independent of the rate of balloon pulsation. This hypothesis derives further support from considerations of gas exchange levels. As noted before, under comparable test conditions, the O₂ exchange rate in blood should be equal to 2.5 to 3 times that in water. The rate of O₂ exchange achieved by the D14 prototype *in-vivo* was over 5 times the rate of O₂ exchange achieved *in-vitro* without balloon pulsation, most likely due to the much higher mean flow velocity *in-vivo* compared to that *in-vitro*.

To confirm our previous hypothesis that *in-vivo* test conditions create a higher mean flow velocity, an *in-vitro* experiment was conducted to determine what effect flow rate and vessel diameter have on gas exchange. Figure 6.16 displays the normalized gas exchange values for the constrained fiber prototype D17.1 at varying beat rates, flow rates and test section diameters. The results indicate that gas exchange becomes independent of beat rate at higher flow rates and decreased vessel diameter. The vena cava of the calf was determined to be approximately 3/4" in diameter while typical cardiac output is around 4.5-6.5 L/min in the inferior vena cava. *In-vitro*

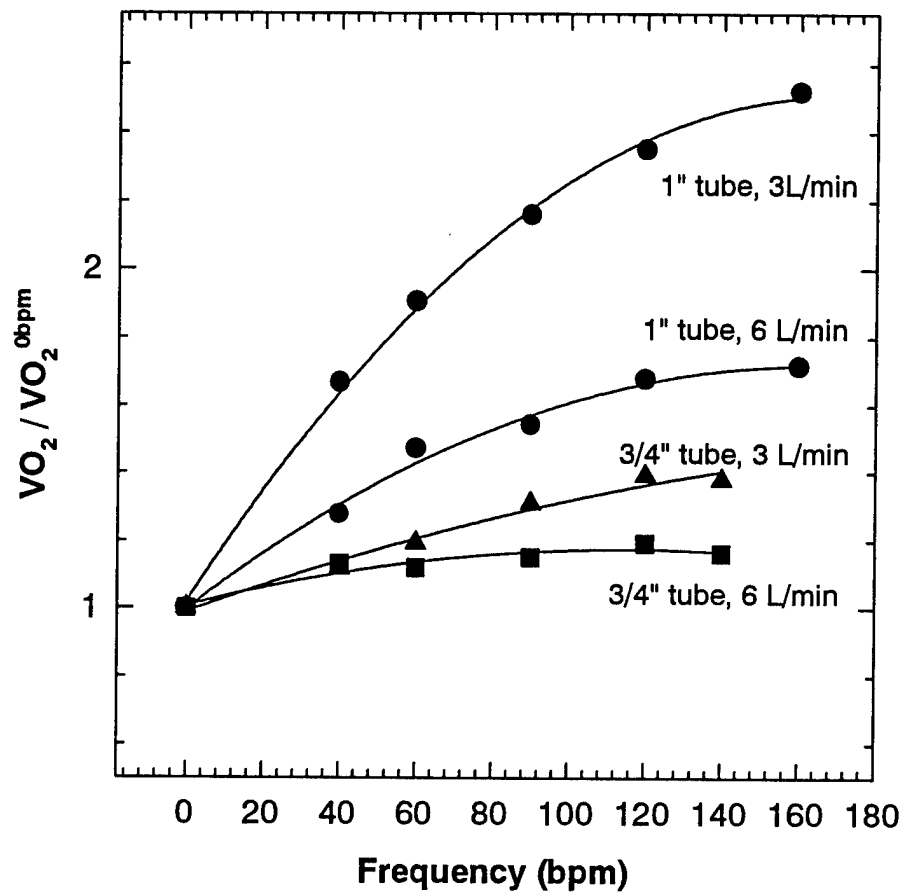


Figure 6.16 Normalized gas exchange rates of D17-1 at varying beat rates, flow rates, and test section diameters.

data in a 3/4" test section flowing at 6 L/min was almost entirely independent of the balloon pulsation rate as were the *in-vivo* results. This data supports our previous theory that a higher mean flow velocity, imparted by a decreased vessel diameter and higher cardiac output, increased the baseline gas exchange rate in the absence of balloon pulsation. Thus, the *in-vivo* results cannot be compared in parallel to normal characterization tests taking place in a 1" test section with a flow rate of 3 L/min. Unfortunately, it is not easy to control the cardiac output within the vena cava of an animal so as to model the typical human values, nor can the vena caval diameter be determined prior to the implant since the animal surgical suite is not equipped with any type of ultra sound or other technology that would allow us to predetermine the vessel anatomy. Our calf model, therefore, may not be the best way to determine the functionality of the IMO *in-vivo*.

In the future, IMO animal experiments need to address the problems of the current animal model. *Ex-vivo* shunt experiments, for example, would enable greater control of test conditions, creating a better human model. These experiments entail running blood through a perfusion loop outside of the body. The IMO device is placed into an appropriately sized mock vena cava section in the loop, as opposed to being implanted into the vena cava, and blood is pumped through the circuit with an extracorporeal blood pump (Model 520 D, Biomedicus, Minneapolis, MN) at the human physiological rate of 3 L/min. This set-up successfully models a typical human vena cava anatomically and allows important physiological factors to be controlled, namely the blood flow rate, temperature, and pressure fluctuations engendered within the system. Blood flow is controlled by the steady flow pump, temperature is held constant at 37 degrees Celsius by means of a heat exchanger, and a venous reservoir post test section dampens pressure fluctuations due to the pulsating balloon. Better control of these experimental factors should render the test results more pertinent to our studies. Animal implantations remain an important part of *in-vivo* studies, allowing researchers to view the direct effect of the device on the involved anatomy, therefore a second possibility may be to explore using animals more relevant anatomically to humans, such as sheep.

7. THE NEXT GENERATION IMO

The scaled-down prototypes of the IMO have attained the targeted oxygen delivery efficiency of 125 ml/min/m² in water, or 250 ml/min/m² in blood. To utilize the entire length of the human vena cava and increase the surface area available for gas exchange, the length of the fiber bundle and central balloon of a full size (clinically relevant) IMO should be 40 cm, compared to the 20 cm long fiber bundle and balloon used in current prototypes. Increasing the length of the fiber bundle and the volume of the balloon will decrease the efficiency of the IMO by reducing the average PO₂ (oxygen partial pressure gradient) in the fiber bundle. Greater drive pressures, ΔP_{drive} , are required from the external drive system since higher flow rates of helium are necessary to fully fill and empty the balloon. Combined, these two factors dictate a redesign of the pneumatic delivery system. Therefore, a design review of the current pneumatic delivery system was conducted to predict its functionality in a full size prototype.

7.1 Design Review of the Current Pneumatic Delivery System

The current pneumatic delivery system is mainly composed of three concentric tubes (see Figure 7.1). Pure oxygen enters the O₂ inlet pathway at atmospheric pressure. It then flows through the O₂ inlet pathway, is released into the distal manifold, and enters the fiber bundle. A certain amount of oxygen diffuses through the fiber walls into the blood flow, and a comparable amount of carbon dioxide diffuses from the blood into the lumens of the fibers. The resulting O₂ and CO₂ exhaust gas is released into the proximal manifold and enters the annular exhaust pathway. The exhaust pathway is connected to a vacuum pump, and the exhaust gases enter the pump and are released to the atmosphere.

The annular space between the O₂ inlet pathway and the exhaust pathway forms the helium pathway. An oscillating flow of helium provided by an external drive system fills and empties the balloon through this pathway. As seen in Figure 7.1, the fibers are potted around the O₂ inlet pathway at the distal end of the device, and around the combined O₂/He pathway at the proximal end of the device. The circular nature of these

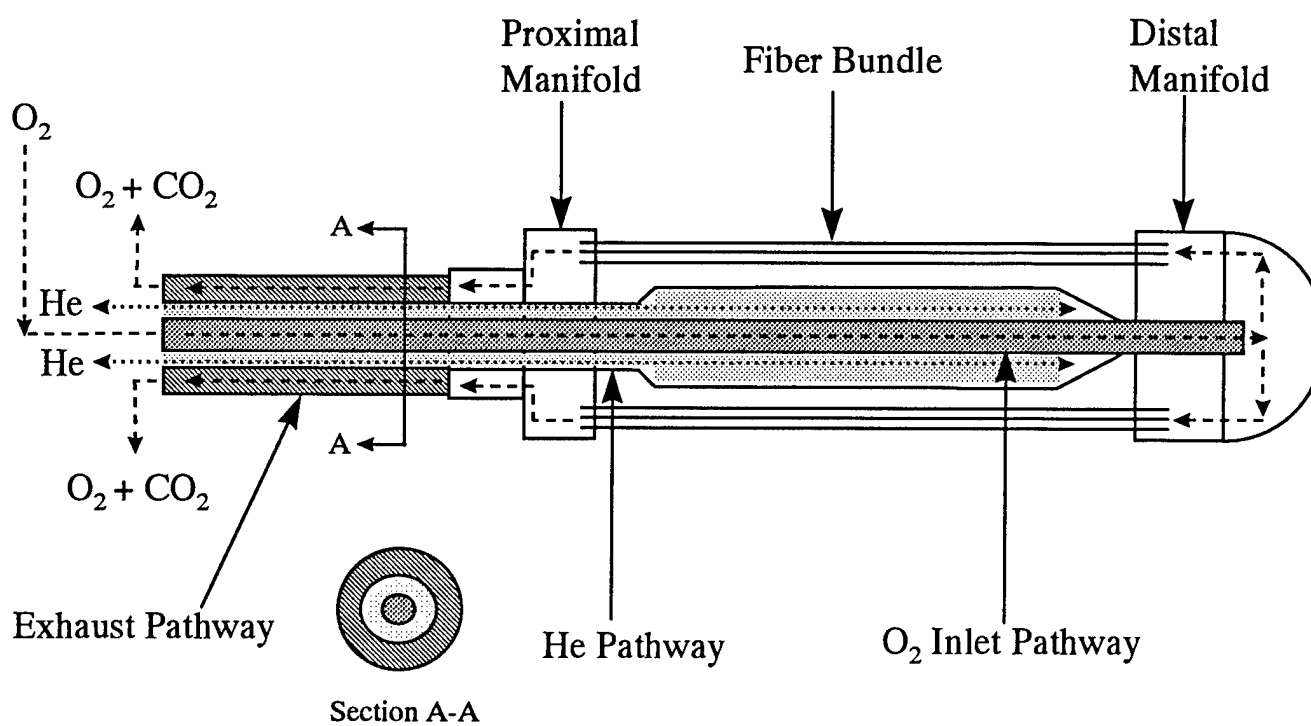


Figure 7.1 Schematic of the current pneumatic delivery system.

pathways allows the potted fiber bundle to be axisymmetric, which is important to prevent preferential shunting of the blood flow generated by the balloon.

The necessity for a redesign of the pneumatic delivery system was based on two factors: the predicted average PO_2 in the fiber bundle of a full size prototype at a sweep gas flow rate of 5 lpm, and the predicted drive pressure required to fully inflate and deflate a full size balloon at 200 bpm. The information needed to make these predictions was obtained using a scaled-down prototype, by experimentally determining $\overline{\text{PO}_2}$ and ΔP_{drive} as functions of the geometry of the pneumatic delivery system, gas flow rate, and fluid properties.

Design Review of the Sweep Gas Pathway. At a given sweep gas flow rate, the average PO_2 in the fiber bundle is given by:

$$\overline{\text{PO}_2} = P_{\text{atm}} - \Delta P_{\text{inlet}} - \Delta P_{\text{fibers}}/2 \quad (7.1)$$

where ΔP_{inlet} is the pressure drop across the O_2 inlet tube and ΔP_{fibers} is the pressure drop across the fiber bundle. The dependence of both ΔP_{inlet} and ΔP_{fibers} on gas flow rate, dimensions of the pathways, and fluid properties has been determined previously, as discussed in section 4.3. As shown in Figures 4.6 a and b, both ΔP_{inlet} and ΔP_{fibers} can be accurately predicted. Using this information, the average PO_2 in the fiber bundle of a full size IMO was predicted as a function of sweep gas flow rate, and is shown in Figure 7.2. At a sweep gas flow rate of 5 lpm the PO_2 is only 590 mmHg, or 78% of its maximum value. This represents a significant decrease in the driving gradient for oxygen exchange, and may indicate a need to redesign the O_2 inlet pathway.

Design Review of the Helium Pathway Balloon pulsation was modeled as steady flow through the helium pathway to predict the drive pressure necessary to fill and empty a balloon of a given volume at a given frequency. The helium flow rate required to fill the balloon at a certain frequency is given by:

$$Q_{\text{balloon}} = 2V_{\text{max}}f \quad (7.2)$$

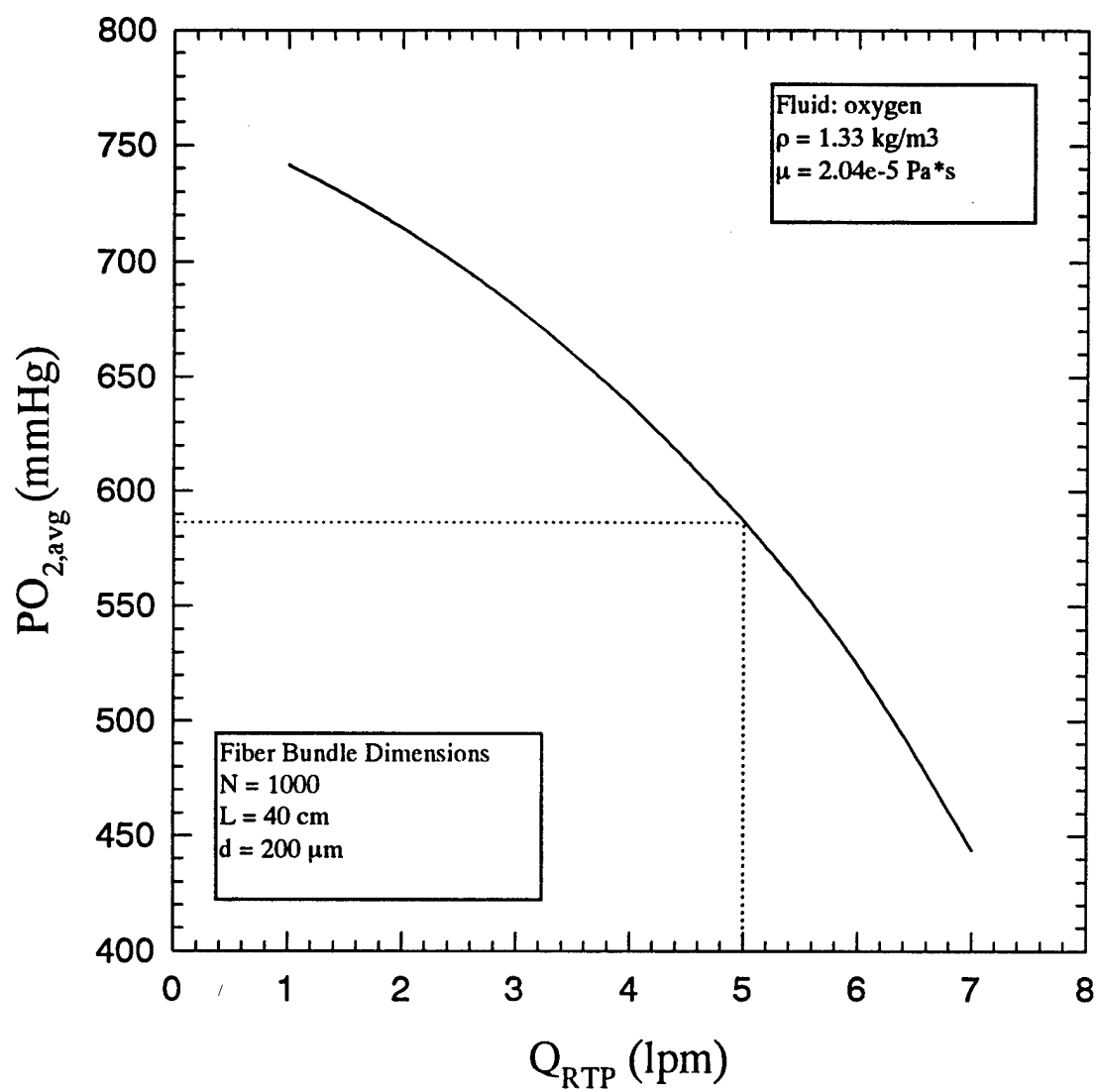


Figure 7.2 Predicted average PO_2 in the fiber bundle of a current design full size IMO prototype.

where V_{\max} is the maximum volume of the balloon and f is the frequency of balloon pulsation. To experimentally determine the dependence of ΔP_{drive} on Q_{balloon} and fluid properties, the balloon was cut away from a prototype, D09-2. Helium was driven through the helium pathway under positive pressure, and the flow was varied. At each flow rate, the pressure at the inlet to the helium pathway was measured as was the gas flow rate.

The pressure drop across the helium pathway as a function of flow rate is shown in Figure 7.3. The pressure drop for laminar flow at a given flow rate, Q , through a concentric annulus is given by⁽¹⁾:

$$\Delta P = \frac{8\mu LQ}{\pi\{r_o^4 - r_i^4 - (r_o^2 - r_i^2)^2 / \ln(r_o/r_i)\}} \quad (7.3)$$

where μ is the dynamic viscosity of the fluid; L is the length of the annulus; r_o is the outer radius of the annulus; and r_i is the inner radius of the annulus. Figure 7.3 shows that this equation predicts the pressure drop across the helium pathway quite accurately. The maximum volume of a full size balloon is 70 ml. Thus, the calculated flow rate of helium (using equation 7.2) required to fill such a balloon is 28 lpm. Manipulation of equation (7.3) indicates that the drive pressure required to pulse a 70 ml balloon at 200 bpm is 265 mmHg.

Outcome of the Design Review If the current pneumatic delivery system is implemented in a full size IMO, the average PO_2 in the fiber bundle will be only 590 mmHg, or 78% of its maximum value, at the operating sweep gas flow rate of 5 lpm. The drive pressure required to pulse a 70 ml balloon at 200 bpm will be at least 265 mmHg. Combined, these factors warrant a redesign of the pneumatic delivery system before a scaled-up IMO prototype is built. The next section will focus on this effort.

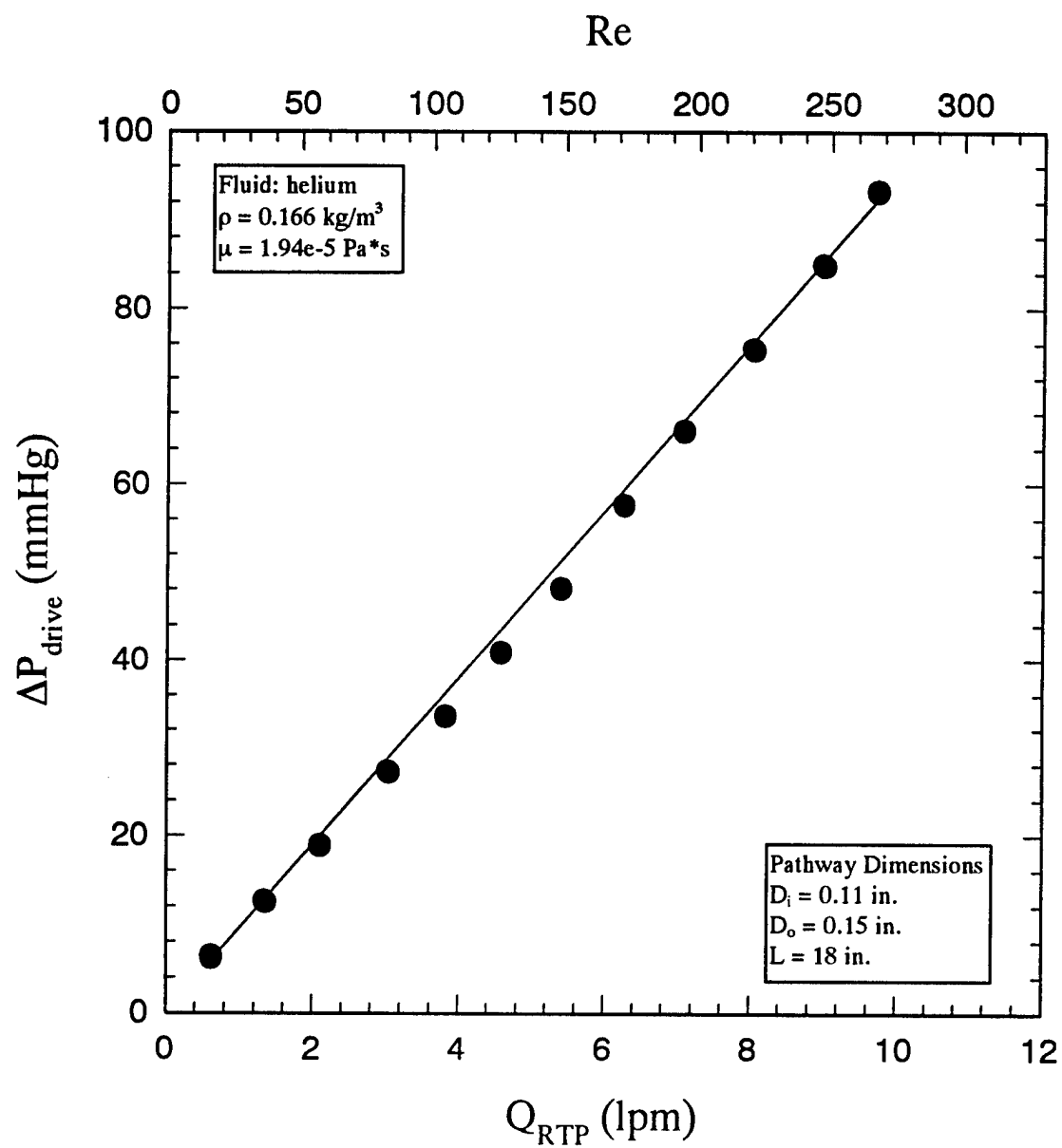


Figure 7.3 Measured and predicted pressure drop across the current design helium pathway.

7.2 Performance of the Improved Pneumatic Delivery System

Building an efficient full size IMO prototype necessitates a reduction in the pneumatic resistances of the O_2 inlet pathway and the helium pathway. The simplest way to reduce the resistances of the pathways, while preserving the circular profile of the combined O_2/He pathway, is to replace the two concentric tubes with one tube in which the lumen is split into two semicircular lumens of equal area.

A length of split lumen tubing with an outer diameter of 0.16 in, wall thickness of 0.14 in, and septum thickness of 0.008 in was obtained from Precision Extrusion, Inc. (South Glens Falls, New York). Each lumen had a hydraulic diameter of 0.08 in and a cross-sectional area of 0.007 in^2 . Dow Pellethane 2363-65D (The Dow Chemical Company, Midland, MI) was chosen as the extrusion material due to its excellent fatigue properties.

A schematic of the improved pneumatic delivery system is shown in Figure 7.4. Oxygen enters the O_2 inlet pathway through the female luer fitting mounted in the exit manifold. It then enters the fiber bundle after being released into the distal manifold. A small amount of O_2 (compared to the overall sweep gas flow rate) diffuses through the walls of the fibers into the bloodstream, and a small amount of CO_2 diffuses from the bloodstream into the fiber lumens. The resulting O_2 and CO_2 exhaust gas is released into the distal manifold and enters the annular exhaust pathway. After traveling the length of the exhaust pathway, the exhaust gas exits the IMO through a female luer fitting mounted in the wall of the exit manifold. The helium pathway spans the entire length of the device. It is plugged with 5-minute epoxy (Devcon, Danvers MA) at the distal manifold, and helium is released to the balloon through three closely spaced holes of 0.0938 in diameter.

Testing of the O_2 Inlet Pathway. Scaled-down ($L = 28.5 \text{ in}$) and full size ($L = 34 \text{ in}$) O_2 inlet pathways were assembled, with the distal ends left open to the atmosphere. The pressure required to drive oxygen through the pathways was measured at gas flow rates from 1 to 10 lpm. The results are shown in Figure 7.5. At a Q_{RTP} equal to 5 lpm, the pressure drop across a full size O_2 inlet pathway was only 32 mmHg. The average partial pressure of oxygen in the fiber bundle of a full size prototype, calculated using equation (7.1) and the information shown in Figure 7.5, is approximately 690 mmHg or 91% of its

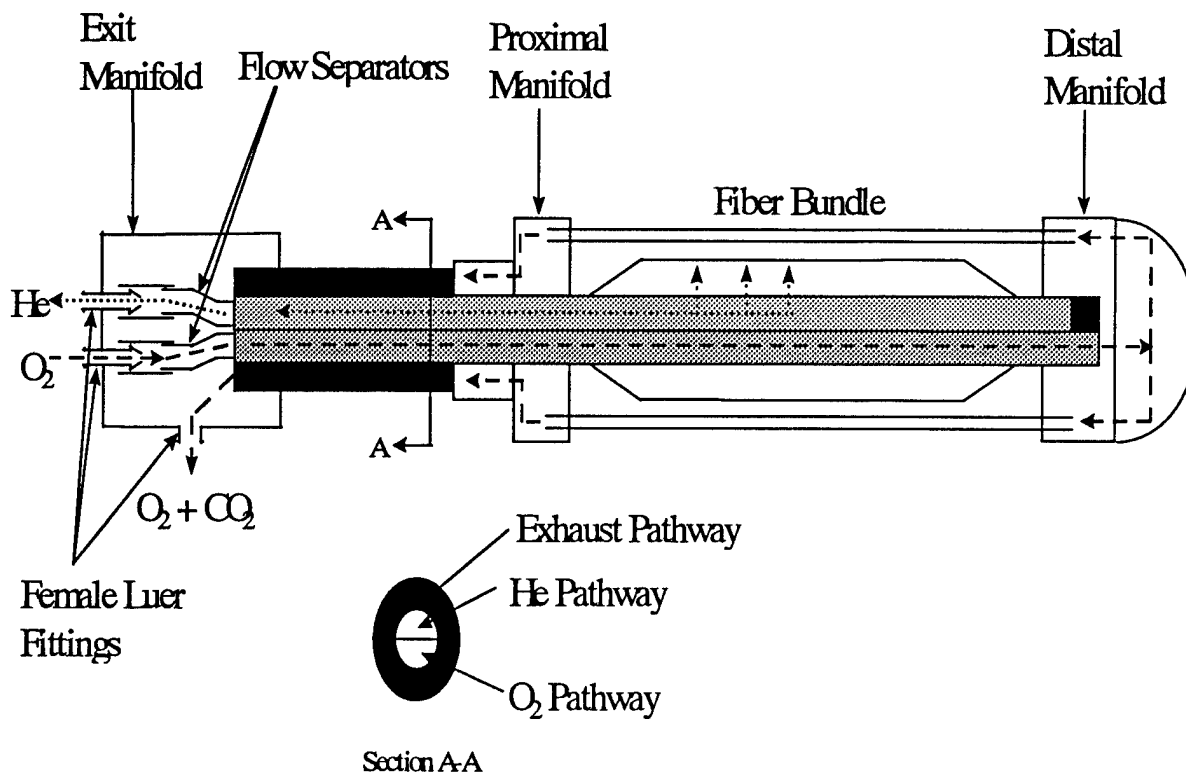


Figure 7.4 Schematic of the improved pneumatic delivery system.

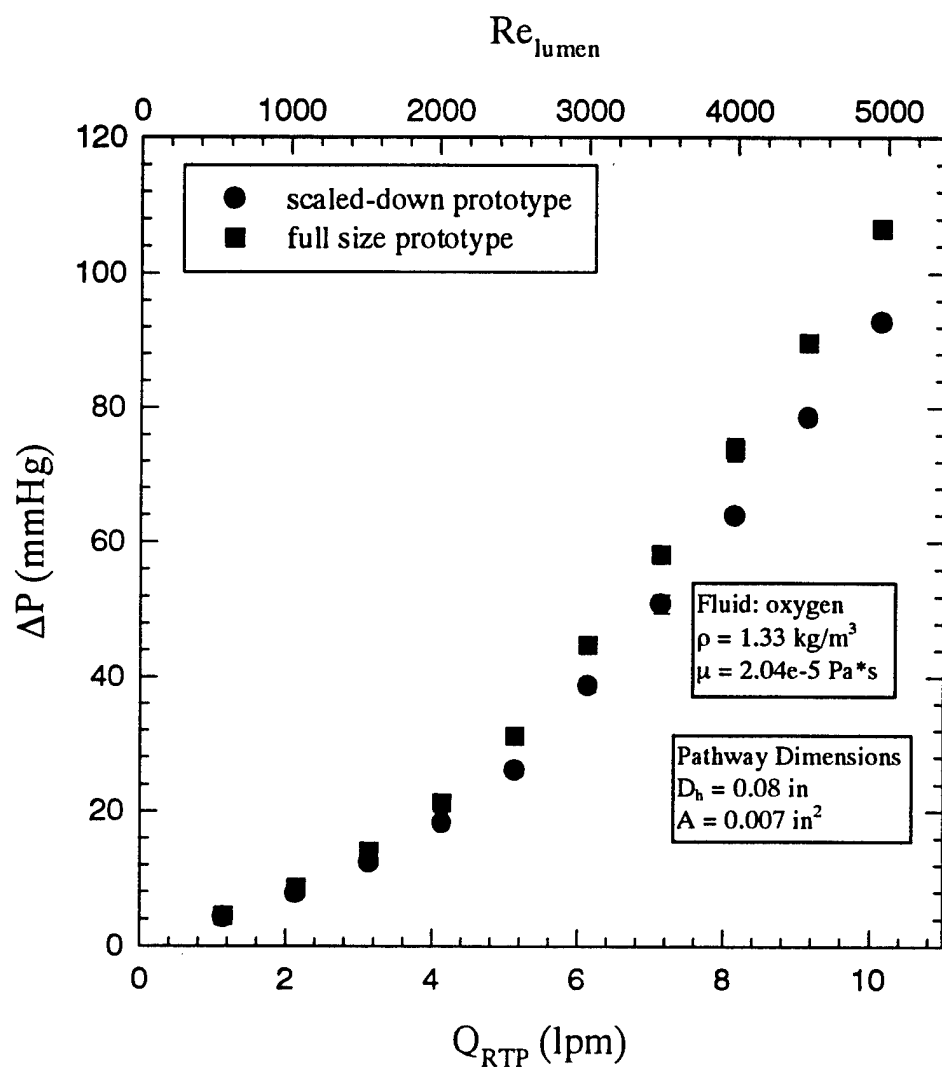


Figure 7.5 Measured pressure drop of oxygen under positive pressure across the improved O_2 inlet pathway.

maximum value. Recall that if the current design for the O₂ inlet pathway were used, the average PO₂ in the fiber bundle would be only 590 mmHg.

Testing of the Helium Pathway. The helium pathway was assembled without a balloon, so that the helium release holes were open to the atmosphere. The pressure required to drive helium, oxygen, and nitrogen through the pathway was measured at gas flow rates from 1 to 17 lpm. The results are shown in Figure 7.6, normalized to fluid properties and gas flow rate. The normalized data for all three gases fall nicely onto one curve.

As discussed earlier, the flow rate required to pulse a 70 ml balloon at 200 bpm is 28 lpm, or $\rho_{RTP} Q_{RTP} / \mu$ equal to approximately 4 m for helium. The flow monitor used can only measure helium flow rates up to 18 lpm, or $\rho_{RTP} Q_{RTP} / \mu$ equal to 2.6 m. The denser oxygen and nitrogen gases were used to obtain data at high values of $\rho_{RTP} Q_{RTP} / \mu$. Since three different gases were used, the data was fit as shown in Figure 7.5.

To calculate the drive pressure required to pulse the balloon, Q_{RTP} was calculated using equation (7.2) at each beat rate. Then $\Delta P / (\rho_{RTP} Q_{RTP} Q_{avg})$ was calculated from the curve fit. The required drive pressure as a function of balloon frequency and helium flow rate is shown for a 70 ml balloon in Figure 7.7. The required drive pressure to empty the balloon is slightly higher than that to fill the balloon since the average helium flow rate required to empty the balloon is higher than Q_{RTP} . For a 70 ml balloon, the external drive system will be need to provide a fill pressure of approximately 80 mmHg and a vacuum pressure of approximately 92 mmHg. Recall that if a full size prototype were constructed using the current design for the helium pathway, the drive pressure required would be at least 265 mmHg.

In summary, the split-lumen design for the combined O₂/He pathway was very successful. Figure 7.8 compares the performance of the improved pneumatic delivery system (PDS) to that of the current pneumatic delivery system. The average PO₂ in the fiber bundle has increased from 590 to 690 mmHg, thus raising the average driving gradient for oxygen exchange by approximately 18%. The drive pressure required to pulse a 70 ml balloon at 200 bpm has been reduced from 290 mmHg to 90 mmHg, indicating

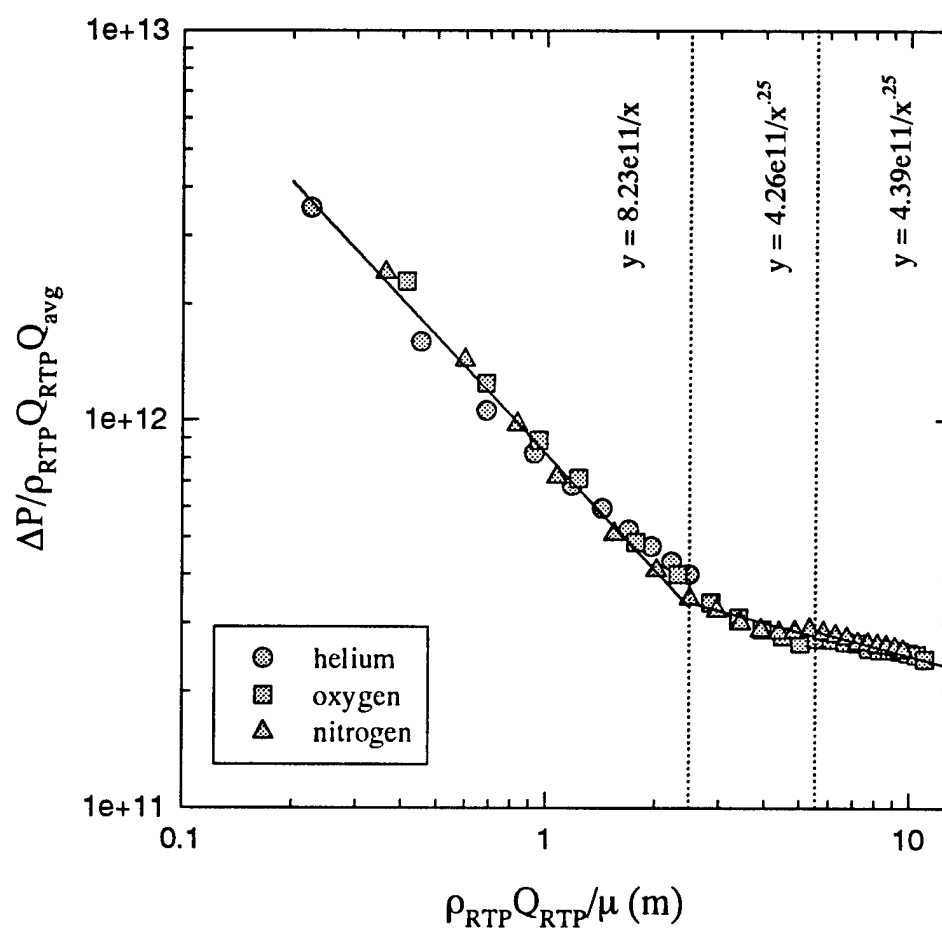


Figure 7.6 Measured pressure drop across the helium pathway normalized to fluid properties and gas flow rate.

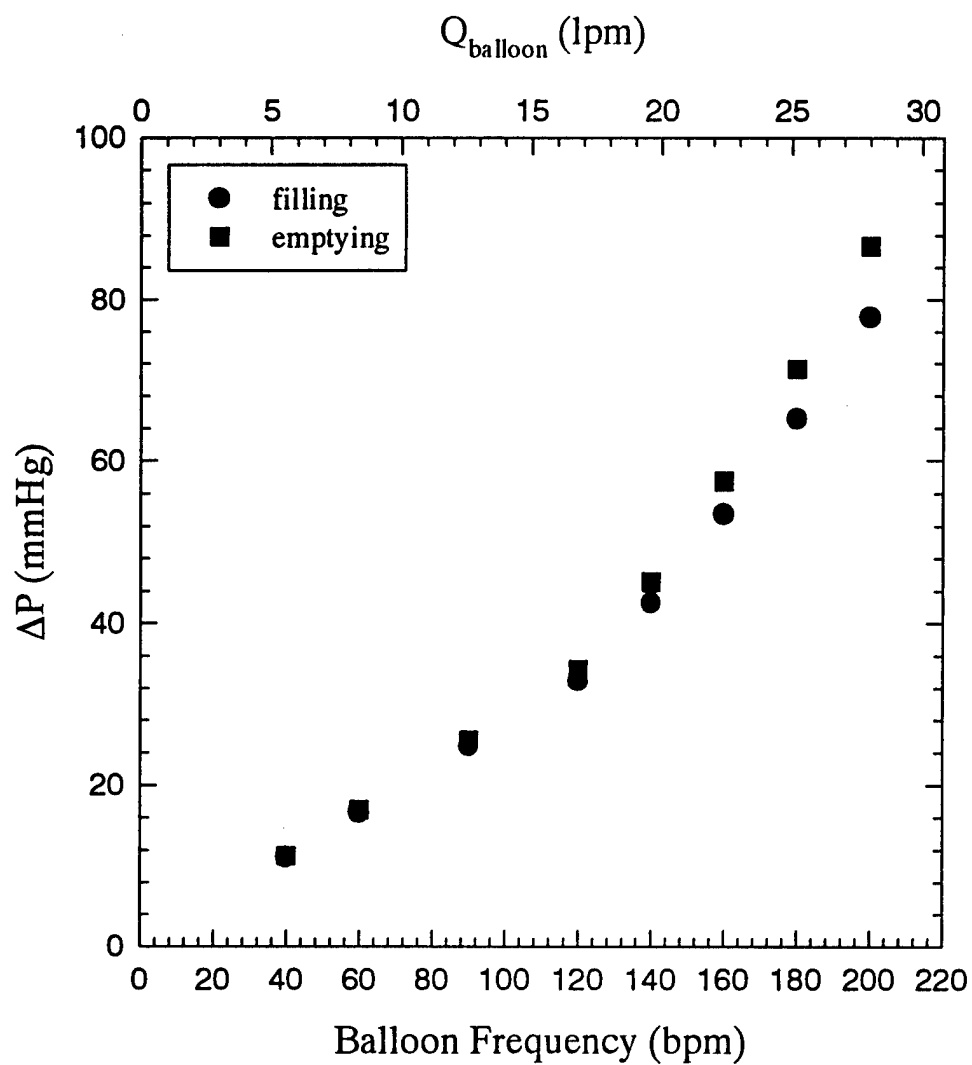


Figure 7.7 Drive pressure required to operate a 70 ml balloon.

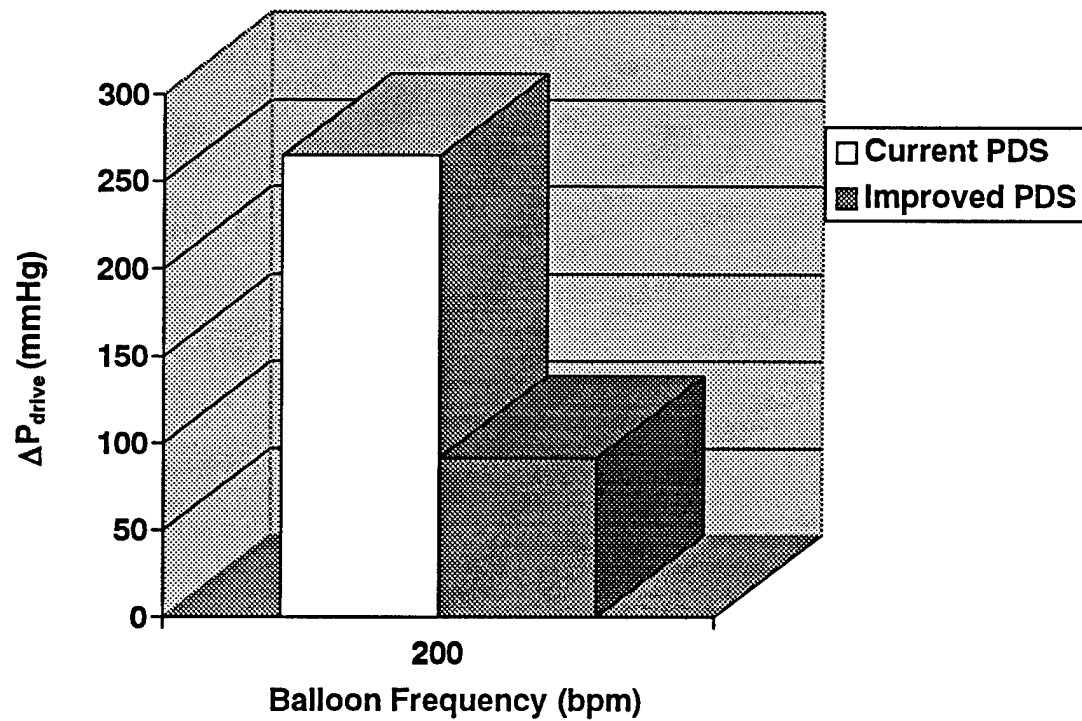
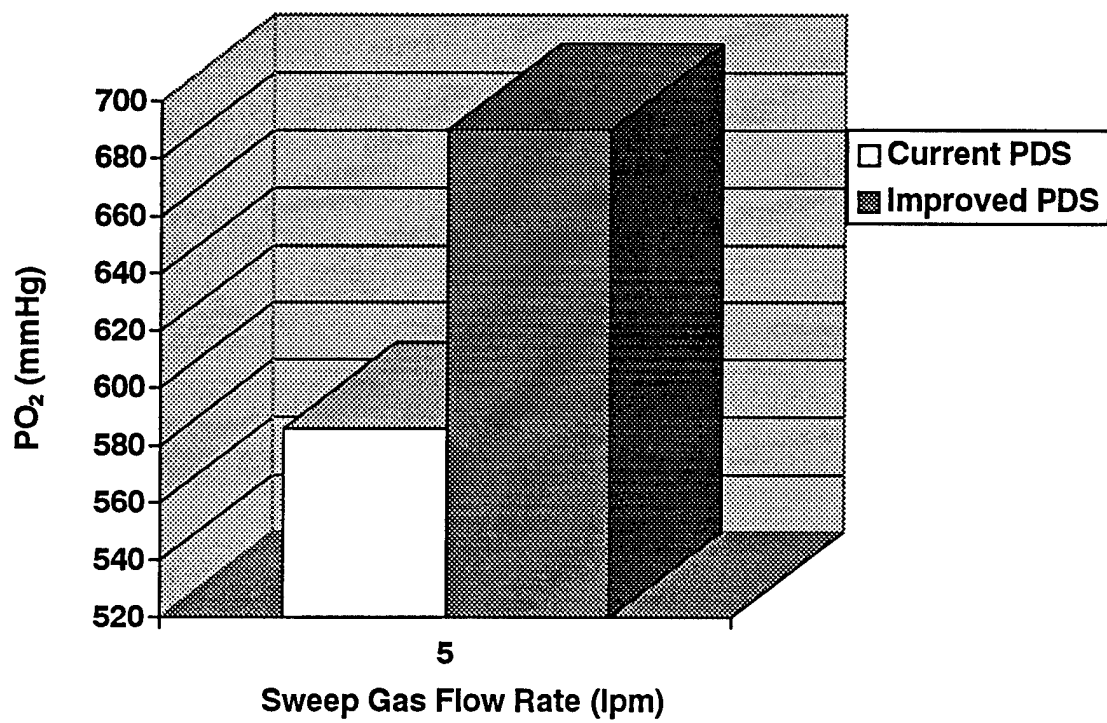


Figure 7.8 Performance of the improved pneumatic delivery system.

that a reasonably powerful external drive system will be able to operate the IMO at frequencies exceeding 200 bpm. Combined, these factors will allow a full size IMO incorporating the improved pneumatic delivery system to perform as efficiently as the scaled-down prototypes which are presently being tested.

7.3 Fiber Fabric Development

The IMO development efforts towards the end of this contract focused on improving fiber bundle design by exploiting hollow fiber mats and novel hollow fiber fabrics to improve fiber distribution, spacing and constraint around the pulsating balloon. As described in Section 5.6, we suspected through our testing of IMO prototypes that the plateau in gas exchange rate with increasing frequency of balloon pulsation (in IMO D08 series) may be due to fiber motion and nonuniform distribution of fibers around the central balloon. Figure 7.9 illustrates the key role which uniformity of fiber spacing plays in the efficiency of gas exchange by eliminating the potential for channeling of convective balloon generated flow in hollow fiber modules. Shown are published engineering mass transfer correlations for cross-flow in different hollow fiber modules. The Sherwood number (ordinate) represents a dimensionless gas exchange per fiber surface area from the module (i.e. an index of gas exchange efficiency), and the Reynolds number (abscissa) represents a dimensionless flowrate velocity through the fiber module. The gas exchange efficiencies of several different fiber modules are compared: a hand-made fiber bundle (●) of carefully aligned and spaced hollow fibers (an "idealized" fiber bundle), the Celgard 240 fiber fabric (▼) under development by Hoechst Celanese Corporation, and several fiber modules from commercially available extracorporeal oxygenators). The latter includes a correlation (■) from measurements on the Medtronic Maxima, Sarns SMO1, and Bard oxygenators, and a correlation from an independent laboratory (◆) for the Sarns oxygenator (Vaslef, 1994). Importantly, the gas transfer correlations are determined for all the modules under equivalent testing conditions.

Figure 7.9 indicates that the best gas transfer performance in hollow fiber modules occurs with carefully spaced and aligned fibers, as in the hand-made module. At a Reynolds number of 10 (a value relevant to flow conditions created by balloon pulsation in

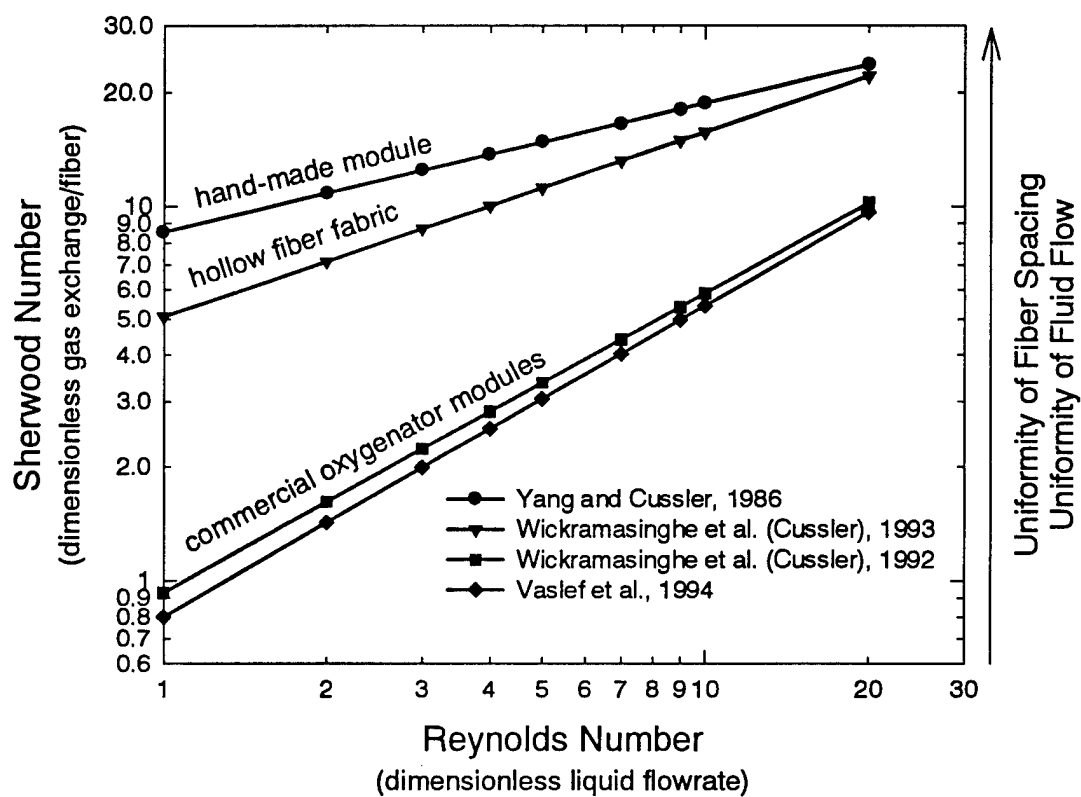


Figure 7.9 Engineering mass transfer correlations for cross flow in different hollow fiber modules.

the IMO), the gas exchange efficiency of this "idealized" fiber module was several fold greater than that for the commercial oxygenator modules. Perhaps more important is that the gas exchange performance of the hollow fiber fabric was within 20% of that for the ideal hand-made module under these same conditions. Thus, the gas exchange efficiency of a hollow fiber fabric can be nearly equal that of a carefully constructed bundle of uniformly spaced fibers, even though fabricating a module with a fiber fabric involves substantially less effort than crafting a hand-made fiber bundle with uniform fiber spacing.

The later IMO devices, the D14 and D17 IMO devices, used the KPF 280 fiber mat (Mitsubishi Rayon, Japan) and the Celgard 240 fiber fabric, respectively. The use of fiber mats and fabrics for the IMO fiber bundle not only helps maintain a more uniform fiber distribution around the pulsating balloon, but constrains the fibers to reduce their motion and increase the relative fluid velocity of pulsation flow past the fibers. The *in-vitro* and *in-vivo* improvement in gas transfer performance realized for these "constrained fiber" devices directly reflect increased gas transfer efficiency due to more uniform fiber spacing and constraint around the central pulsating balloon. The hollow fiber mat used in the D14 IMO device, however, employs fibers with an OD of 380 microns. The large size of these fibers would preclude scale-up to an implantable device with 0.5 m². The Celgard 240 fabric used in the IMO D17 device is under development by Hoechst-Celanese Corporation (Charlotte, NC) and incorporates their X10-240 microporous hollow fiber, which has an outer diameter of 300 microns. Although this fiber fabric uses the smallest hollow fibers made by Hoechst-Celanese, the X10-240 fiber is relatively large compared to other commercially available hollow fibers. Furthermore, the Celgard fiber fabric may not be available for use in intracorporeal (implantable) artificial lungs because of corporate policy at Hoechst-Celanese against supplying material for implantable medical devices...

Scaling-up to an IMO device with 0.5 m² membrane area will require using the smallest hollow fiber membranes currently available. Mitsubishi Rayon currently makes a hollow fiber (the KPF 190) which has an outer diameter of 240 microns and hence has nearly 40% less volume than that of the Hoechst-Celanese X10-240 fiber. Although the KPF 190 fiber is the smallest membrane on the market, it is not currently available in a mat

or fabric configuration. Thus, we have recently begun a collaboration with a textile research and development firm, Prodesco Inc., of Perkasi, PA, to develop a fiber fabric using the KPF 190 hollow fiber membrane. An IMO device with an exchange performance equal to or better than our D14 and D17 devices, but fabricated with smaller diameter hollow fibers, will be a key step in the development of the scaled-up IMO for ultimate clinical use.

Development efforts on a hollow fiber fabric incorporating the KPF 190 fibers are currently underway. Several weaving processes have been explored at Prodesco in pilot studies and the resultant fabrics tested at the University of Pittsburgh for fiber patency (open fiber lumens). The "gold standard" for our fabric development work is the Celgard 240 fiber fabric, shown using scanning electron microscopy (SEM) in Figure 7.10. The Celgard fabric is composed of hollow fibers (running horizontally in the SEM), and interwoven polyester yarn support filaments (running vertically in the SEM). The Celgard 240 fabric maintains an impressive uniformity of fiber spacing using a weaving process which locks loop stitches around the fibers without compressing or damaging them. Our goal is to achieve a weave similar to the Celgard fabric, but with the smaller KPF fibers and using a weaving process which minimizes damage to these smaller fibers. Figure 7.11 shows an SEM picture of one of the first prototype fabric samples (Flat Weave B) made by our textile collaborators at Prodesco. The hollow fibers run vertically and the support threads run horizontally. Clearly evident is the compression of fiber lumens where the fibers weave above and below the support yarn filaments. Because fiber lumens were significantly compressed, we were unable to get measurable gas flow through the fabric at normal sweep gas flow driving pressures.

Figure 7.12 shows an SEM of a more recent fabric prototype (Flat Weave D) from Prodesco made using a different weaving process than that used for the fabric in Figure 7.11. The fibers in Flat Weave D appear less damaged and compressed by support yarns, but some crimping of the fibers is still apparent. We quantitatively assessed fiber lumen patency by measuring the gas flow resistance through the fabric. The pressure drop flowrate relationship for gas flow through Flat Weave D is shown in Figure 7.13, and compared to the expected theoretical value for the fabric had all fibers remained at normal

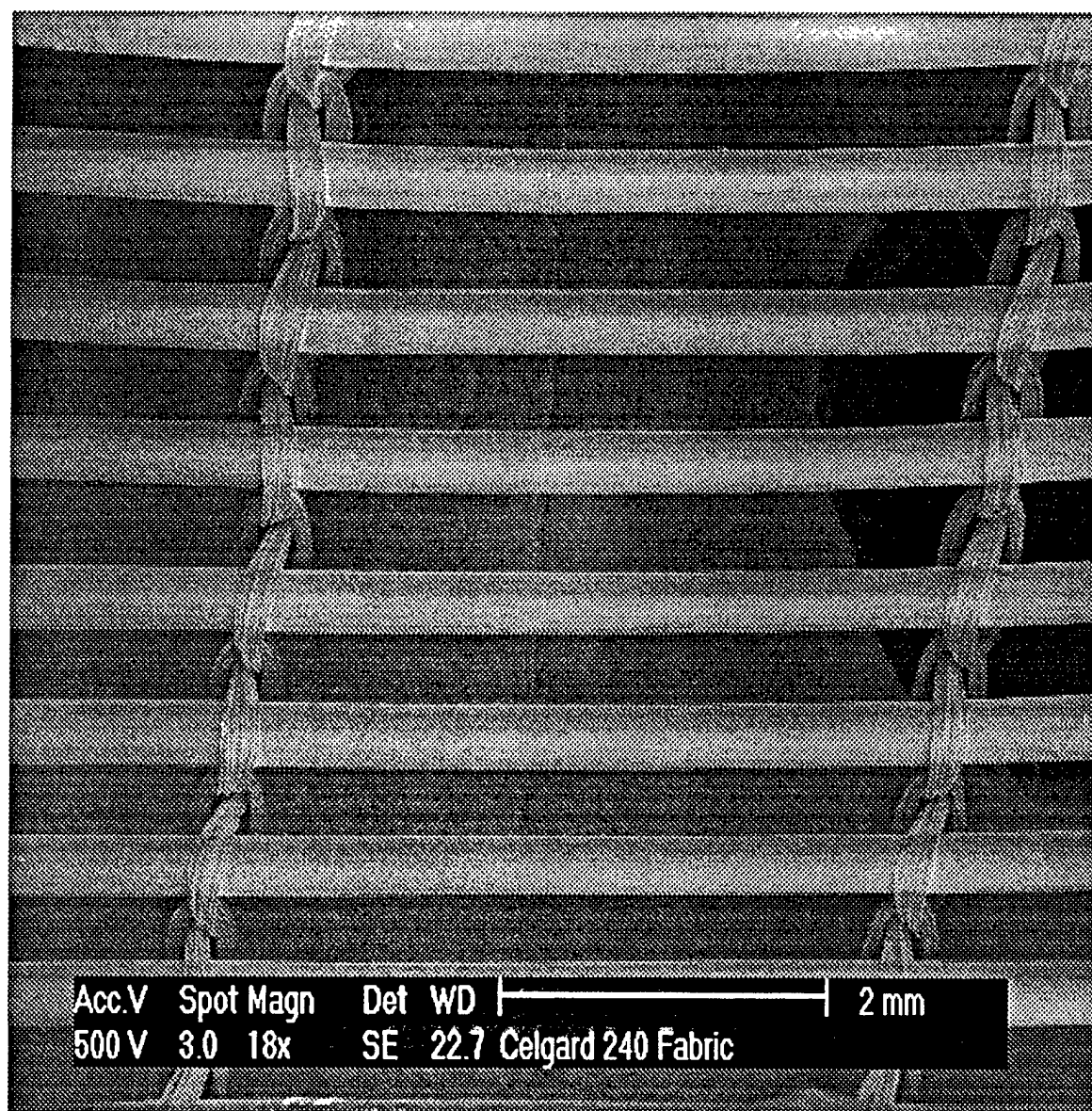


Figure 7.10 Scanning electron microscopy picture of the Hoechst Celanese Celgard 240 fiber fabric, our “golden standard” for fiber fabric.

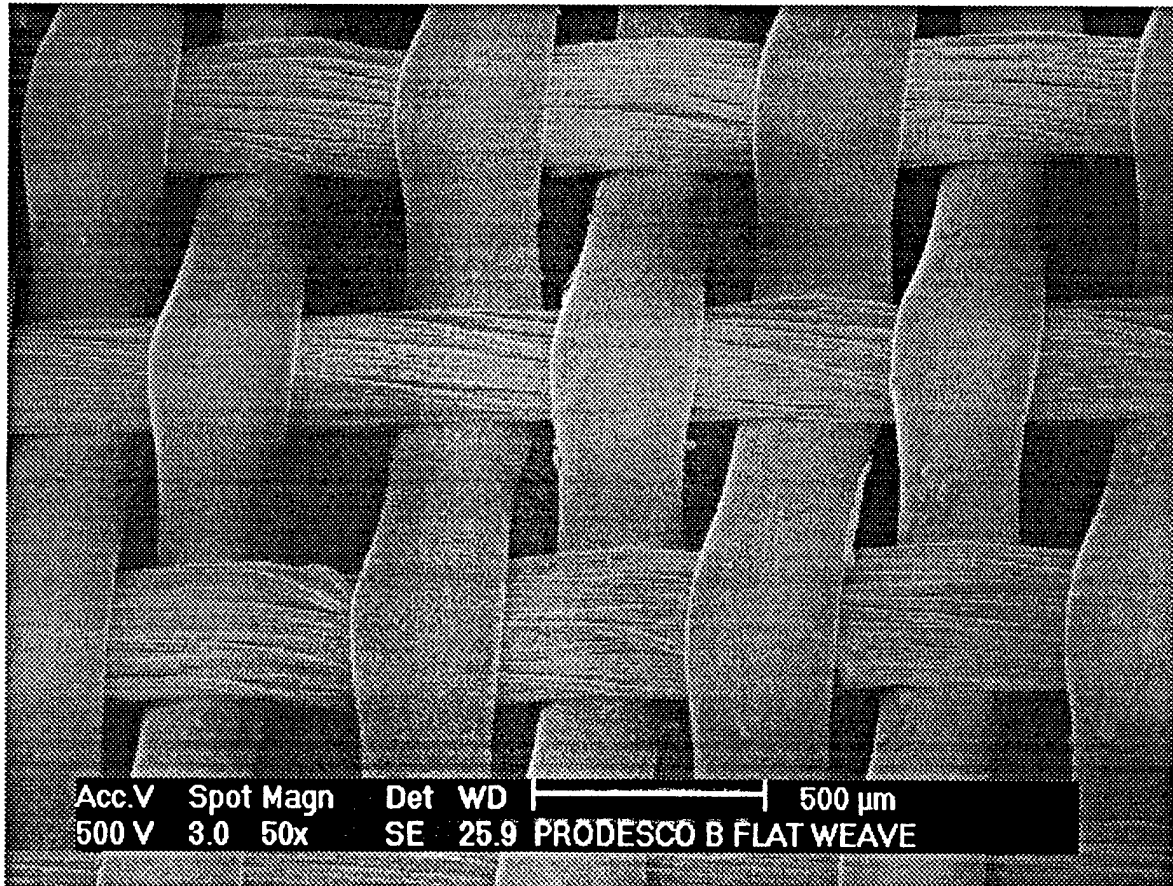


Figure 7.11 The first Prodesco made fiber fabric, Flat Weave B. Crimping of the fibers is apparent.

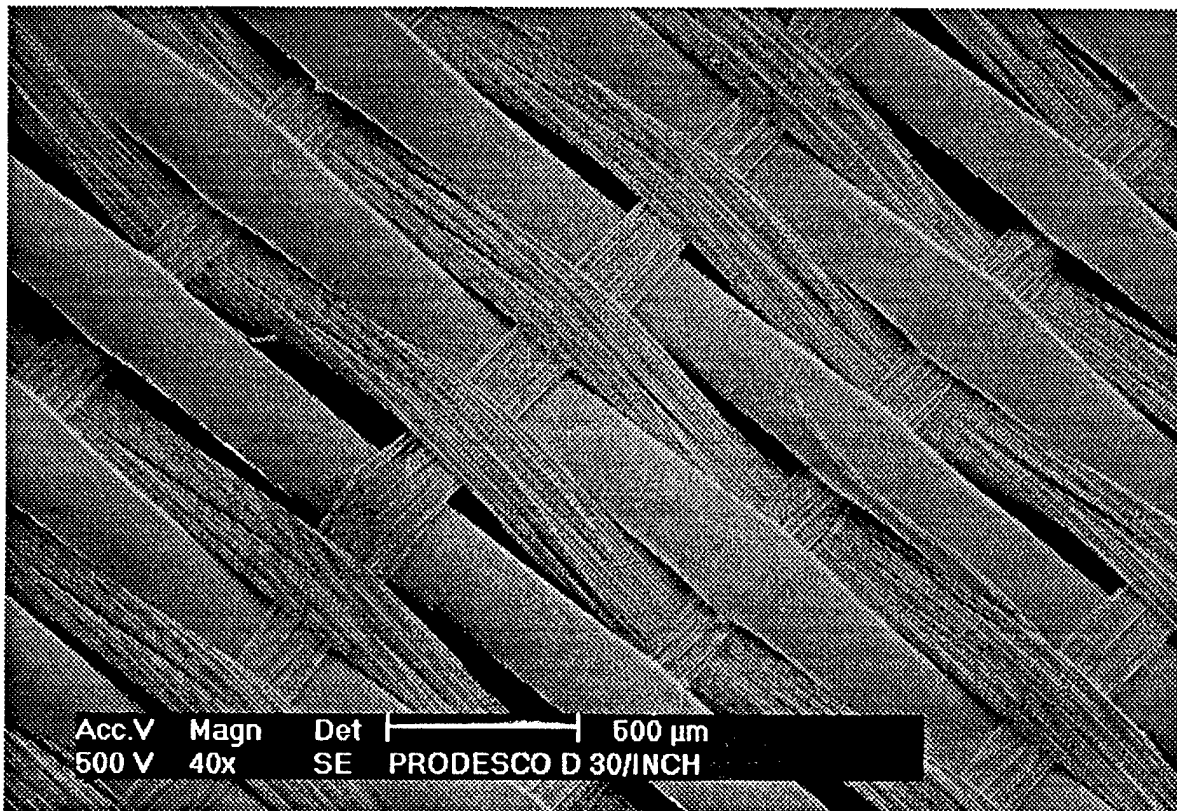


Figure 7.12 Prodesco made flat weave D fiber mat. The fibers appear less crimped than those of the flat weave B.

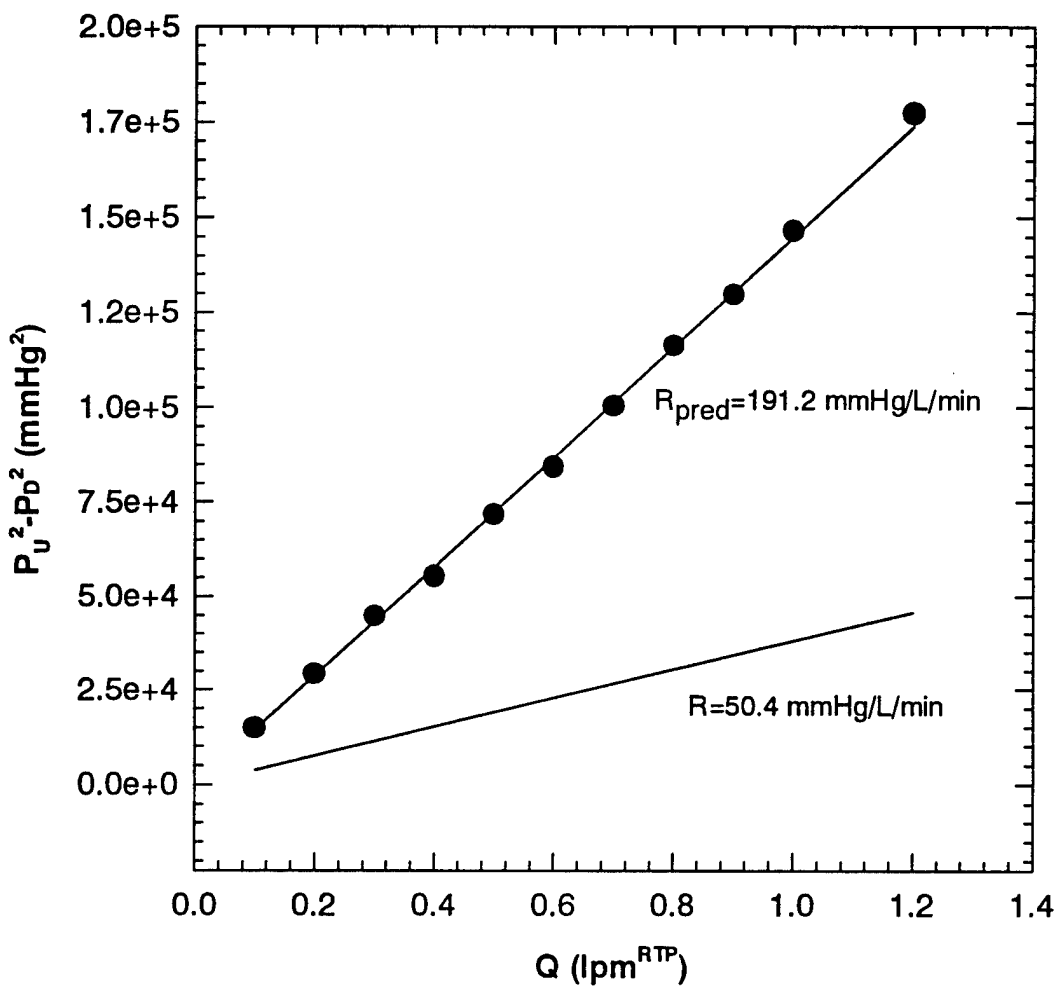


Figure 7.13 The pressure drop flowrate relationship for gas flow through Prodesco's Flat Weave D.

patency. The gas flow resistance of the fabric was 191.2 mmHg per liter/minute gas flow, which is about 3.8 times the resistance of the fabric if the hollow fibers were not compressed. Another problem is that this fabric weaving process required support yarns running parallel as well as perpendicular to fibers, which may unacceptably increase the fabric density and hence the resistance to blood flow through the fabric. Clearly, further development work is needed on hollow fiber fabrics for the IMO device, and future work will explore alternative weaving processes, as well as nonwoven fabric methodologies.

8. CONCLUSIONS

This contract funded development work on an effective, implantable-sized Intravenous Membrane Oxygenator (or IMO) for soldiers and civilians experiencing acute failure of their lungs. The failure may arise from trauma to the chest, inhalation of smoke and toxic gases, infection and sepsis, or shock. The lungs ability to oxygenate blood and remove carbon dioxide is significantly diminished, and immediate supplemental respiratory support is needed to rest the lungs and allow them to heal. The IMO device developed here consists of a bundle of hollow fiber membranes manifolded to gas supply and removal lines, which can be inserted through a peripheral vein and placed within the vena cava system, the major veins returning blood flow to the heart. Oxygen (O_2) flowing through the IMO diffuses from the hollow fibers into venous blood, while carbon dioxide (CO_2) diffuses from blood into the gas flow stream and is removed. A pulsating balloon integrally located within the fiber bundle provides additional fluid convection which facilitates O_2 supply and CO_2 removal. In this manner, the affected soldier or civilian is "breathing" even though his lungs are severely compromised, and this artificial breathing is allowing the lungs to rest and heal.

The contract work firmly established proof-of-principle for the IMO concept. The most recent IMO prototypes developed under this contract exchanged O_2 and CO_2 at rates equal to or exceeding our design target for gas transfer per unit fiber surface area, set at 240-270 ml gas/min/m² in blood (or a comparable rate of about 120-135 ml/min/m² in water.) This design target provides roughly 50% of the normal baseline metabolic requirements for O_2 supply and CO_2 removal with an IMO device of 0.4 to 0.5 m² fiber surface area, and is a significant improvement over the gas transfer rates accomplished by intravenous oxygenators previously developed. This design target was reached through extensive and systematic *in-vitro* and *in-vivo* characterization testing and analysis of IMO prototypes, which guided subsequent modification and improvements to the IMO design. The principal improvements were 1) an increase in the attainable balloon pulsation rates from 60 to 160 bpm, with a concomitant increase in gas transfer, and 2) use of "constrained" fiber bundles which helped maintain uniform and optimal fiber spacing around the central balloon, while minimizing fiber motion and maximizing relative fluid motion

past the fibers. A recent IMO prototype exploiting these improvements exchanged 403 ml/min/m² of CO₂ and 340 ml/min/m² of O₂ *in-situ* during acute implantation in a calf.

The current status of IMO development is summarized in Figure 8.1 with respect to a planned four-phase development effort required to bring the IMO to clinical trials. The design target for gas transfer was achieved, as described above, using IMO prototype devices with scaled-down fiber bundle *lengths* (of 20 cm). These lengths were chosen based on the length of available standard intra-aortic balloons, which are used as the pulsating balloons within the fiber bundle. Attainment of our gas transfer target with the scaled down IMO devices was the milestone for completion of Phase 1, and provided proof-of-principle that the IMO had the gas exchange efficiency required to meet our ultimate gas exchange design goal. The second phase of IMO development has already begun and involves scaling-up the IMO device to full-size fiber bundle lengths of 35-40 cm, with the requisite 0.4-0.5 m² of fiber surface area. The principal *development* tasks associated with the Phase 2 scale-up are 1) the design review and modification of the pneumatic pathways of the IMO to accommodate longer fiber bundles and larger pulsating balloons in the scaled-up IMO, without degradation in device performance; 2) the development of pulsating balloons with lengths matched to fiber bundle length; and 3) the development of fiber fabrics and/or other constrained fiber bundles using the smallest hollow fiber membranes available (KPF 190). The first and third of these Phase 2 tasks have already begun near the end of the contract period and are described in Chapter 7.

<u>Phase</u>	<u>Milestone</u>	<u>Status</u>
1: Feasibility	Gas exchange target in scaled-down devices	Completed
2: Scale-Up	Gas exchange target in full-size devices	Starting
3: System	IMO System Design Freeze	Pending
4: Readiness	IDE	Pending

Figure 8.1 Summary of the current status of IMO development with respect to a planned four-phase development effort required to bring the IMO to clinical trials.

9. REFERENCES

Bird, B.R., Stewart, W.E., and Lightfoot, E.N. *Transport Phenomena*. New York: John Wiley & Sons, 1960.

Conrad, S.A. et al. Major findings from the clinical trials of the intravascular oxygenator. *Artif. Org.* 18(11): 846-863, 1994.

Fazzalari, F.L., Bartlett, R.H., Bonnell, M.R., and Montoya, J.P. An intrapleural lung prosthesis: rationale, design, and testing. *Artif. Org.* 18 (11): 801-805, 1994.

Federspiel, W.J. et al. Recent Progress In Engineering The Pittsburgh Intravenous Membrane Oxygenator. *ASAIO J.* 42: M435-M442, 1996.

Federspiel, W.J. et al. Development Of A Low Flow Resistance Oxygenator. *ASAIO J.* *in press*.

Grodins, F.S. and Yamashiro, S.M. *Respiratory Function of the Lung*. New York: Macmillan Publishing Company, 1978.

Hattler, B.G. et al. Respiratory dialysis: a new concept in pulmonary support. *ASAIO J.* 38: M322-M325, 1992.

Hattler, B.G. et al. Development of an Intravenous Membrane Oxygenator: enhanced intravenous gas exchange through convective mixing of blood around hollow fiber membranes. *Artif. Org.* 18: 806-812, 1994.

Kamo, J. et al. A new multilayered composite hollow fiber membrane for the artificial lung. *Art. Org.* 14(5): 369-372, 1990.

Lund, L.W. et al. Gas permeability of hollow fiber membranes in a gas-liquid system. *J. Membrane Sci.* 117: 207-219, 1996.

Munson, B.R. *Fundamentals of Fluid Mechanics*. New York: John Wiley & Sons, Inc., 1994.

Qi, Z. and Cussler, E.L. Microporous hollow fibers for gas absorption. II. Mass transfer across the membrane. *J. Membrane Sci.* 23: 333-345, 1985.

Reeder, G.D. *The Biochemistry and Physiology of Hemoglobin*. Reston, Virginia: American Society of Extra-Corporeal Technology, 1986.

Vaslef, S.N., Mockros, L.F., Anderson, R.W., and Leonard, R.J. Use of a mathematical model to predict oxygen transfer rates in hollow fiber membrane oxygenators. *ASAIO J.* 40: 990-996, 1994.

Vaslef, S.N. et al. Computer-assisted design of an implantable, intrathoracic artificial lung. *Artif. Org.* 18 (11): 813-817, 1994.

Weinberger, S.E. *Principles of Pulmonary Medicine*. Philadelphia: W.B. Saunders Company, 1992.

10. PROJECT BIBLIOGRAPHY

Full Articles:

Federspiel, W.J., Williams, J.L., and Hattler, B.G. Gas flow dynamics in hollow fiber membranes. *AIChE J.* 42(7): 2094-2099, 1996.

Lund, L., Federspiel, W.J., and Hattler, B.G. Gas permeability of hollow fiber membranes in a gas-liquid system. *J. Membr. Sci.* 117: 207-219, 1996.

Federspiel, W.J., and Hattler, B.G. Sweep gas flowrate and CO₂ exchange in artificial lungs. *Artif. Org.* 20(9): 1050-1056, 1996.

Konishi, R., Shimizu, R., Firestone, L., Wagner, W., Federspiel, W.J., Konishi, H., and Hattler, B.G. Nitric oxide presents human platelet adhesion on fiber membrane in whole blood. *ASAIO J.* M850-M853, 1996.

Macha, M., Federspiel, W.J., Lund, L., Sawzik, P., Litwak, P., Walters, F., Reeder, G., Borovetz, H., and Hattler, B.G. Acute in-vivo studies of the Pittsburgh intravenous membrane oxygenator. *ASAIO J.* 42: M609-M615, 1996.

Lund, L., Federspiel, W.J., Taitel, F., and Hattler, B.G. A novel method for measuring hollow fiber membrane permeability in a gas-liquid system. *ASAIO J.* 42: M446-M451, 1996.

Federspiel, W.J., Hewitt, T., Hout, M., Walters, F., Lund, L., Sawzik, P., Reeder, G., Borovetz, H., and Hattler, B.G. Recent progress in engineering the Pittsburgh intravenous membrane oxygenator. *ASAIO J.*: 42: M435-M442, 1996.

Federspiel, W.J., Sawzik, P., Borovetz, H., Reeder, G.D., and Hattler, B.G. Temporary Support of the Lungs - the Artificial Lung. D.K.C. Cooper, L.W. Miller, G.A. Patterson (eds), *The Transplantation and Replacement of Thoracic Organs*, Boston, Kluwer Academic Publishers, 1996

Federspiel, W.J., Hout, M.S., Hewitt, T., Lund, L.W., Heinrich, S.A., Litwak, P., Walters, F., Reeder, G., Borovetz, H., and Hattler, B.G. Development of a low flow resistance intravenous oxygenator. *ASAIO J.*: in press, 1997.

Hewitt, T.J., Hattler, B.G., and Federspiel, W.J. A mathematical model of gas exchange in an intravenous membrane oxygenator. *Ann. Biomed. Eng.*, in press 1997.

Lund, L.W. and Federspiel, W.J. Is condensation the cause of plasma leakage in microporous hollow fiber membrane oxygenators. *ASAIO J.*: submitted, 1997.

Meeting Abstracts:

Lund, L., Federspiel, W.J., Wallace, M., Walters, F., Borovetz, H., and Hattler, B.G. Evaluation of a composite hollow fiber membrane for an intravenous membrane oxygenator. Fall Meeting of the Biomedical Engineering Society, Boston, 1995.

Konishi, R., Firestone, W., Wagner, W., Federspiel, W.J., Konishi, H., Shimizu, R., and Hattler, B.G. Nitric oxide presents human platelet adhesion on fiber membrane in whole blood. *ASAIO J.* 42(2): 72, 1996.

Macha, M., Federspiel, W.J., Lund, L., Sawzik, P., Litwak, P., Borovetz, H., Walters, F., Reeder, G., and Hattler, B.G. Acute in-vivo studies of the Pittsburgh intravenous membrane oxygenator. *ASAIO J.* 42(2): 69, 1996.

Lund, L., Federspiel, W.J., Taitel, F., and Hattler, B.G. A novel method for measuring hollow fiber membrane permeability in a gas-liquid system. *ASAIO J.* 42(2): 67, 1996.

Federspiel, W.J., Walters, F., Hewitt, T., Hout, M., Lund, L., Sawzik, P., Reeder, G., Borovetz, H., and Hattler, B.G. Recent progress in engineering the Pittsburgh intravenous membrane oxygenator. *ASAIO J.* 42(2): 71, 1996.

Federspiel, W.J. Engineering a novel intravenous oxygenator. Spring meeting of the American Association of Civil Engineers. Mechanics Division. Ft. Lauderdale, FL, May, 1996

Federspiel, W.J. Walters, F.R., Hewitt, T., Hout, M.S., Lund, L., and Hattler, B.G. Further development of an intravenous membrane oxygenator with active mixing. *Ann. Biomed. Eng.* 24: S6, 1996.

Hout, M.S., Federspiel, W.J., and Hattler, B.G. A simple model of flow dependent CO₂ exchange in artificial lungs. *Ann. Biomed. Eng.* 24: S8, 1996.

Lund, L.W., Federspiel, W.J., and Hattler, B.G. Hollow fiber membrane permeability evaluation for use in intracorporeal artificial lungs. *Ann. Biomed. Eng.* 24: S8, 1996.

Federspiel, W.J., Hout, M.S., Hewitt, T.J., Lund, L.W., Heinrich, S.A., Macha, M., Litwak, P., Walters, F.R., Borovetz, H.S., and Hattler, B.G. Development of a low flow resistance intravenous oxygenator. *ASAIO J.* 43(2): 14, 1997.

Federspiel, W.J., and Hattler, B.G. The Intravenous Membrane Oxygenator: An idea whose time has come. 10th Annual Trauma Anesthesia and Critical Care Symposium. Baltimore, MD, May 17, 1997

11. Artificial Lung Program Personnel & Titles

Brack G. Hattler, MD, PhD.	Principle Investigator
William J. Federspiel, PhD.	Project Director
Shelly Heinrich, BS.	Research Specialist
Mark Wallace, BS.	Research Specialist
Jason White, BS.	Research Specialist
Todd Hewitt, MS.	Research Assistant
Mariah Hout, MS.	Research Assistant
Laura Lund, MS.	Research Assistant
Tamara Tulou, BS.	Research Assistant
Jeff Williams, MS.	Research Assistant
Brian Frankowski	Fabricator
Philip Litwak, DVM, PhD.	Veterinarian
Mary Watach, BS.	Animal Technician
Lisa Gordon, BS.	Animal Technician
Marina Kameneva, PhD.	Scientist
Patricia Sawzik, PhD.	Scientist
Frank Walters	Consultant